THE ATMOSPHERIC INFORMATION CONTENT OF EARTH'S FAR INFRARED SPECTRUM

by

Aronne Merrelli

A dissertation submitted in partial fulfillment of
the requirements for the degree of

Doctor of Philosophy
(Atmospheric and Oceanic Sciences)

at the
UNIVERSITY OF WISCONSIN–MADISON
2012

Date of final oral examination: November 26, 2012

The dissertation is approved by the following members of the Final Oral Committee:

David D. Turner, Assistant Professor, Atmospheric and Oceanic Sciences
Steven A. Ackerman, Professor, Atmospheric and Oceanic Sciences
Ralf Bennartz, Professor, Atmospheric and Oceanic Sciences
Andrew K. Heidinger, Physical Scientist, Cooperative Inst. for Meteorological Satellite Studies
Grant W. Petty, Professor, Atmospheric and Oceanic Sciences

ABSTRACT

A key component of the modern Earth observation system is the Mid-Infrared (MIR) hyperspectral sounder. Operational instruments on polar orbiting satellites are collecting a continuous record of highly accurate infrared spectra with a wide variety of applications in geoscience. Although some research instrumentation early in the development of the meteorological satellite used Far-Infrared (FIR) sensitive detectors, the primary focus of infrared instrumentation has been the MIR region. Recent developments in FIR instrumentation and a renewed interest in the FIR for climate applications has brought attention to this underexplored part of Earth's Infrared spectrum.

The information content of Earth's FIR spectrum is investigated within a modeling framework that simulates satellite observations of FIR and MIR spectra at hyperspectral resolution. The framework allows for direct comparison of the two spectral ranges, which can quantify the potential benefits of combining FIR spectral observations with the state of the art MIR observations. The framework is first applied to investigate the information content for retrieving the vertical temperature and water vapor profile in clear sky conditions. The FIR shows additional sensitivity to upper tropospheric and lower stratospheric water vapor, and a slight but consistent vertical resolution advantage relative to the MIR. By extending the simulation framework to include layer clouds composed of ice particles, the information content in cloudy sky profiles and cloud properties is investigated. In certain conditions, the FIR shows additional profiling information transmitted through the cloud layer and additional information above the cloud through the interaction between water vapor absorption and ice particle scattering and absorption. Finally, the including FIR spectra increases information content for cloud properties in cases where the MIR has poor sensitivity. These cases include high optical depth clouds and clouds with particle effective radius. Error propagation calculations are used to estimate the improvement on the resulting cloud Ice Water Path

(IWP). These results suggest extending the spectral coverage of the hyperspectral sounder into the FIR would improve the retrieval of several important geophysical quantities.

ACKNOWLEDGMENTS

Reflecting on my non-traditional path back to grad school, I realize there are quite a few people who have helped me along the way, and many places where things just had to "line-up" to bring me to this point in my career. Before applying to grad school in atmospheric science, I was lucky to work for a great team at Ball Aerospace that gave me my first exposure to research in remote sensing. Working with Chris Borel and Mark Manzardo helped to show me that remote sensing would be a rewarding career path. I learned a lot from them about the process of applying theory to practical problems. The support of my supervisors, Bryan Everding and Lynne Vettel, was extremely helpful as I was able to pursue engineering graduate studies in the Electro Optics department at the University of Dayton. The support and teaching at UD was excellent in all regards and I learned a great deal. In particular, Brad Duncan, Russ Hardie, and Andrew Sarangan were excellent teachers mentors during my time at UD. I would later discover that solving Maxwell's equations in a cylindrical waveguide is excellent practice for tackling GFD problems!

After finishing a master's degree at UD, I was making yet another turn in my career path when I decided to return to grad school full time. Atmospheric science was a change to a new field, and I had a very incomplete picture of its research community. In hindsight, I was very lucky to have chosen to apply to the University of Wisconsin, since at the time I did not fully appreciate this institution's role as a world leader in satellite meteorology. I would like to thank Steve Ackerman for taking the time to contact me during the application process and showcasing CIMSS and AOS as an excellent environment for graduate research.

At UW, I have had the pleasure to work with many excellent professors and research scientists. Each member of my committee has provided valuable support and advice at various stages of my research, and I thank them for their willingness to support my dissertation. Dan Vimont contributed

a great deal to my research using the NCAR CESM. Discussions with Dan helped me work through the practical issues that arise while running a GCM as well as the statistical issues involved with interpreting GCM data.

Within SSEC and CIMSS, I have benefited from the advice and expertise of many, in particular Bryan Baum, Paolo Antonelli, Eva Borbas, Bob Knuteson, Dave Tobin, Hank Revercomb, and Bob Holz. Whether it was sharing a dataset, a useful MATLAB function, or explaining the inner workings of an FTS, I greatly appreciate all the assistance. I would also like to thank the SSEC Technical Computing group, especially for support with the computing cluster which I have used extensively in this research.

Finally, I would like to thank my research adviser, Dave Turner, for all of his time and energy invested in this dissertation. Since Dave had to relocate to NSSL partway through my time at UW, we have had to deal with the "long distance" advising problem. Many times people would ask me how this was working out. In many cases I am sure that a student's research has suffered due to the difficulties of a remote adviser. Fortunately, this never became a problem. Dave has always been extremely reliable with our "semi-weekly" teleconferences while balancing his time between a number of other projects and meetings at NSSL.

This work was partially supported by the NASA grant NNX08AP44G as part of the CLARREO program, and DOE grant DE-FG02-06ER64167 as part of the ARM program.

TABLE OF CONTENTS

Page

Appendix

Page

LIST OF FIGURES

LIST OF TABLES

Chapter 1

Introduction

Understanding Earth's weather and climate requires detailed knowledge of the energy flows in and out of the system, at a wide variety of spatial and temporal scales, across a wide swath of the electromagnetic spectrum. From this planetary perspective, it is most convenient to split the spectrum according to the energy flow into the Earth system from the Sun, called the "shortwave" radiation, and the energy flow out from the Earth in the form of "longwave" radiation. This split is also useful to classify passive remote sensing techniques. In large part, when studying radiative processes in the shortwave region, the problem can be considered one of scattering, reflection, and absorption of the incident irradiance from the Sun, with no emission at all from any terrestrial sources. In the longwave region, the problem is now typically dominated by emission from terrestrial sources, with some scattering and reflection depending on specific wavelength in consideration. The solar term in the longwave can be taken as zero, since it is orders of magnitude smaller than the terrestrial terms (Figure 1.1). The separation between these two regimes is not a sharp boundary, but typically a wavelength of roughly 4 μm (wavenumber 2500 cm^{-1}) is a reasonable choice. Wavelengths near this value are neither purely "shortwave" nor "longwave" in their characteristics, and exhibit radiative influence from all of the above processes.

The longwave spectrum can be further divided into several primary spectral bands. The lowest frequency region, microwave, can be taken as < 300 GHz (or equivalently a wavelength of > 1 mm). This of course includes radio waves, but for purposes of meteorology, radio waves are not typically relevant so can be ignored in this discussion. The highest frequency region is the infrared,

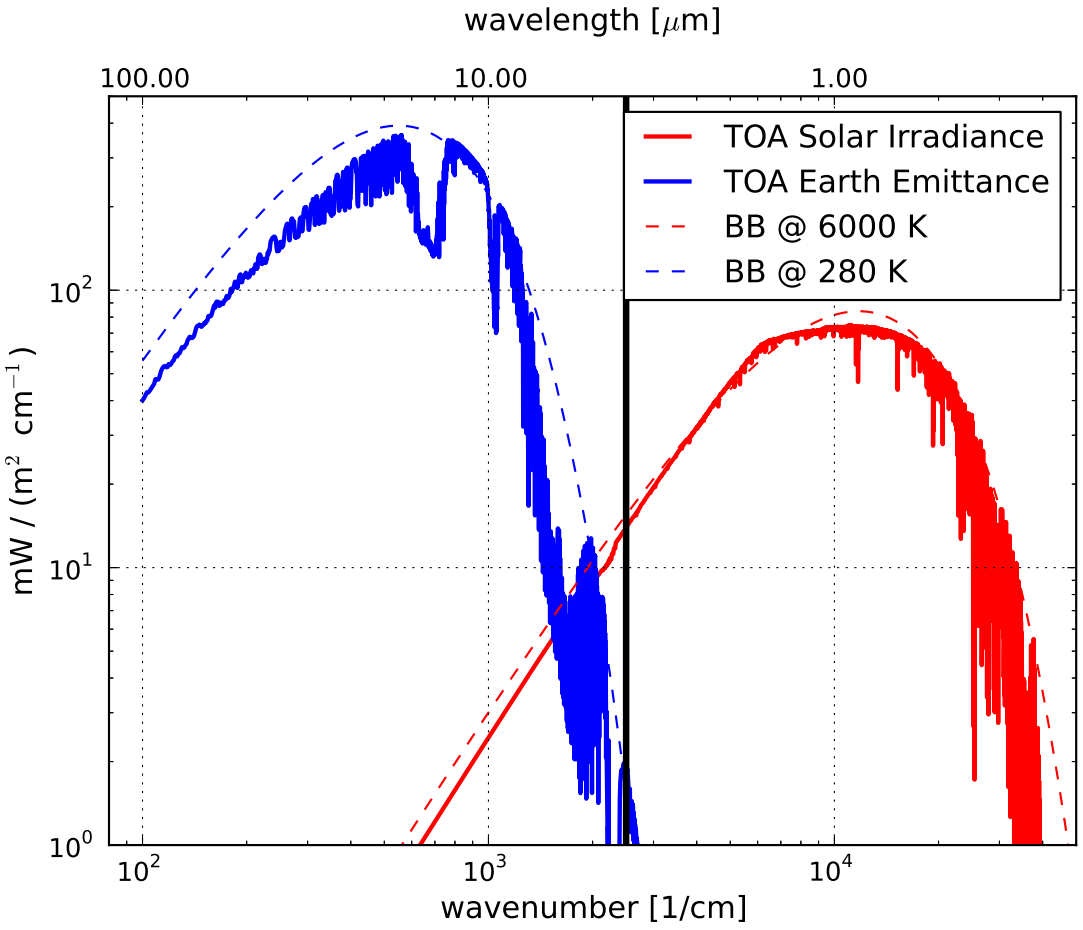

Figure 1.1 The solar spectral irradiance, for zero degree zenith angle, and the earth spectral emittance (for a clear sky standard atmosphere) at the top of the atmosphere. The solid vertical line marks the longwave-shortwave division at wavenumber of 2500 cm^{-1} (4 μm wavelength). Earth spectrum computed from LBLRTM, Solar spectrum from (Kurucz, 1992).

which is defined here as frequencies of > 3 THz (100 cm^{-1}) or equivalently wavelengths < 100 μm. Between these two regimes is the submillimeter band, covering wavelengths between 1 and 0.1 mm (0.3–3 THz). The infrared can be further split into two regions, the far and mid infrared, at a wavenumber of 667 cm^{-1} (15 μm wavelength). Typically another division at perhaps 1500 cm^{-1} (6.7 μm wavelength) would be made to separate mid infrared from "shortwave" infrared (not to be confused with the definition "shortwave" radiation above), but that distinction is not relevant to the discussion at hand, so the entire band 667–2500 cm^{-1} (15–4 μm) will be considered as the MIR band. These spectral range definitions are summarized in Table 1.1. Figure 1.2 shows these definitions as annotations on over a simulated brightness temperature spectrum.

Although these different regimes throughout the longwave have significantly different scattering characteristics for atmospheric particles because of the wide range in scattering size parameter, the radiative transfer problem is actually quite similar across the entire range, especially in cloud-free atmospheres. Thus, to some extent the divisions between these regimes are made to reflect the specific technology used to make instrumentation for the given frequency range. For example, microwave instruments often use coherent detection with heterodyne receivers, while infrared detectors are typically photoelectric. In fact, one of the reasons for the lack of observations in the FIR region is the lack of mature instrumentation choices. MIR photodetectors can be created with sensitivity to longer wavelengths, and thus lower energy photons, by engineering materials with smaller band gap energies. At such small band gaps, the thermal electron energy must be greatly reduced to prevent an overwhelming background signal; this implies much lower temperature cooling systems which add significant cost and complexity. From the other direction, microwave systems can be designed for higher frequencies. Some recent limb sounding missions have had used channels at 500 GHz and 600 GHz (Odin, Nordh et al. (2003), SMILES, Takahashi et al. (2010)), and the highest frequency reached was the 2.25 THz channel on the Aura MLS (Schoeberl et al., 2006). Higher frequencies are not easily measured with coherent techniques, as it becomes difficult to construct reliable local oscillators at these high frequencies (Evans et al., 2002). Direct detection at these frequencies can be done with bolometers, but achieving low noise requires advanced detector technologies such as high temperature superconducting films. This in

an area of ongoing research (Kreisler and Gaugue, 2000), but no recent missions in atmospheric science have used this technology.

Both the microwave and the mid-infrared are very well studied, with a long heritage back to the some of the original scientific missions flown on the first space launch missions. Many of the modern techniques were first tested on a series of pathfinding instruments in the 1960's and 1970's as part of the Nimbus program. Two experiments in the Nimbus series did examine parts of the FIR spectrum. The IRIS spectrometer had a low frequency cutoff at 400 cm^{-1}; the ITPR instrument used a 460–540 cm^{-1} channel (Atlas, 1969). The focus on meteorological missions since that time however has focused on MIR spectral regions. The reasons for this shift are not well documented, but are likely related to the relative advantage of using MIR photodetectors, as described above. The initial FIR-sensitive instruments used pyroelectric and bolometric devices as detectors; it is likely these were outperformed by MIR photodetectors. Since the primary focus of meteorological missions since that time (e.g., TIROS and NOAA-POES) has been temperature and water vapor sounding, the FIR spectral features can be viewed as redundant with the MIR spectral features. Specifically, the sounding can be performed by measuring the long wavelength side of the 15 μm CO_2 band, and the water vapor rotational band (e.g., using the FIR), or using the short wavelength side of the 15 μm CO_2 band and the first vibrational-rotational band of water vapor (e.g., using the MIR). With higher information content measurements, there are important differences in the different spectral regimes, but for low spectral resolution measurements they are roughly equivalent. Since a low-noise MIR detector is easier to construct, the MIR became the primary spectral region for high spatial resolution sounding.

Thus, the FIR and submillimeter spectral regions represent a frontier in atmospheric remote sensing. The submillimeter region has been the focus of recent research, as a new remote sensing tool for characterizing ice clouds. Recently developed pathfinding instruments have been deployed on aircraft in targeted field campaigns (Evans et al., 2005). Other research groups have proposed new satellite missions based on this concept, in order to improve our global knowledge of ice cloud properties, primarily focusing on the critical ice water path variable. (Buehler et al., 2007, 2012).

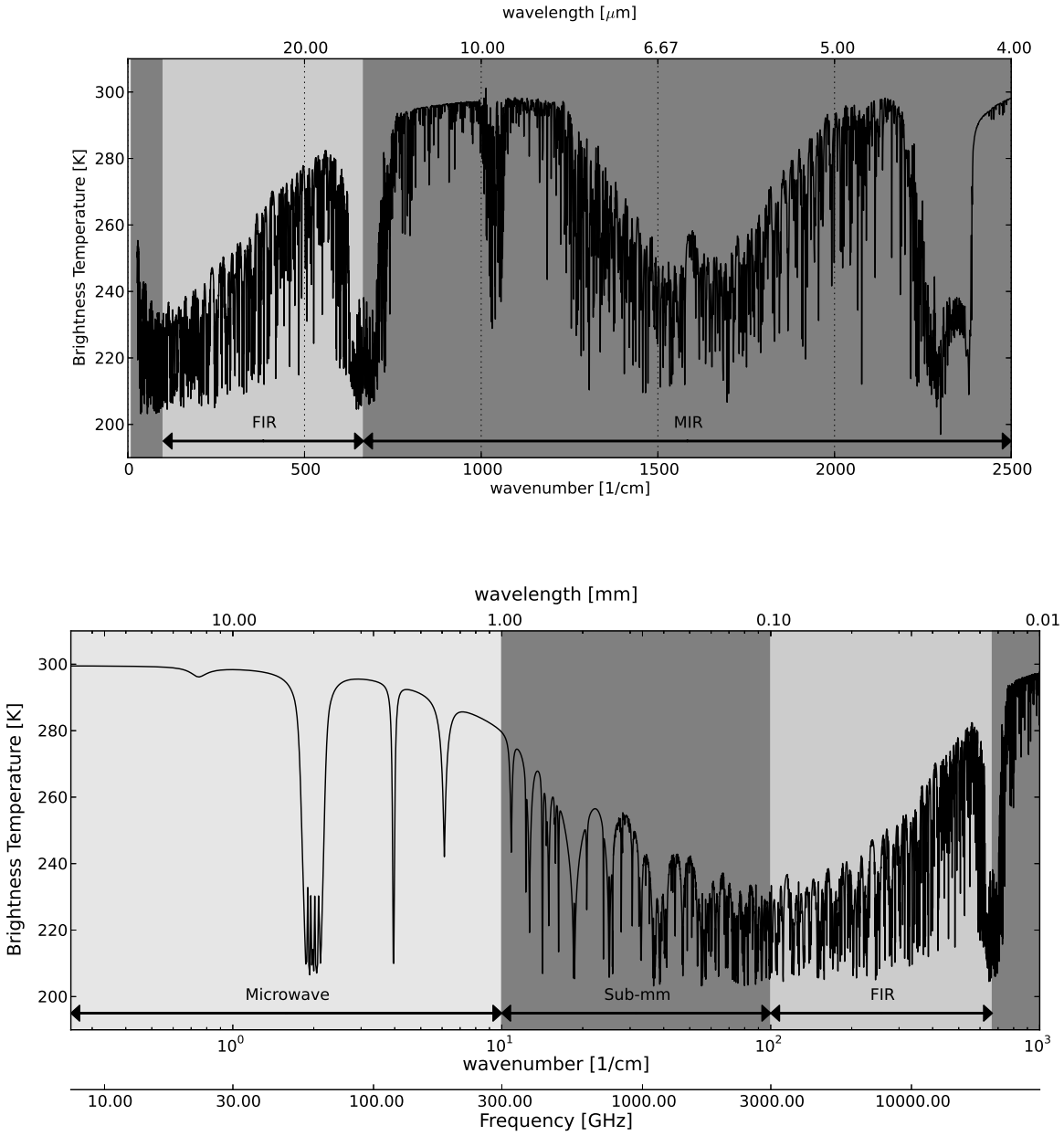

Figure 1.2 A division of the longwave spectrum into microwave, submillimeter, FIR, and MIR spectral ranges, with a linear frequency scale (top) and logarithmic frequency scale (bottom)

Table 1.1 Spectral Region Definitions

Spectral region	Frequency Range	wavenumber range	wavelength range
Microwave	3–300 GHz	0.1–10 cm^{-1}	1 mm–10 cm
Submillimeter	0.3–3 THz	10–100 cm^{-1}	0.1–1 mm
FIR		100–667 cm^{-1}	15–50 μm
MIR		667–2500 cm^{-1}	4–15 μm

In this work, the remote sensing potential of the FIR spectrum is studied. The FIR has unique aspects that are of interest to atmospheric science, particularly how FIR radiation interacts with water in all three thermodynamic phases. In particular, this dissertation focuses on the use of FIR measurements for temperature and water vapor sounding, and ice cloud characterization. Using various radiative transfer models, high spectral resolution measurements of the MIR and FIR upwelling radiance are simulated and analyzed. The modeling framework allows the FIR information content to be compared and contrasted with the MIR.

Chapter 2

Background

2.1 A Brief Review of Infrared Satellite Sensors [1]

Very early in the development of satellite technology, the possibility of using space based platforms for remote sounding was an active subject of research. The first thorough documented research in this area was from the Environmental Science Services Administration (ESSA) in the United States during the 1960's (Wark and Fleming, 1966; Hilleary et al., 1966; Wark et al., 1967). The techniques used in these studies were similar to the original proposal by Kaplan (1959), where the remote sounding would be done with several moderate spectral resolution (approximately 5 cm^{-1}) measurements in the 667 cm^{-1} CO_2 absorption band. The technique was demonstrated with a balloon-borne instrument flight to simulate the satellite view.

These first demonstration studies led to further experiments on a series of research satellites in the Nimbus program in the late 1960's and early 1970's. The Nimbus program served as a testbed for many technologies that would form the core of the polar orbiting meteorological satellite sensing program. Many different instrumentation techniques were attempted, the primary infrared experiments being the Satellite InfraRed Spectrometer (SIRS), the Infrared Temperature Profiling Radiometer (ITPR), and the InfraRed Interferometer Spectrometer (IRIS). SIRS and IRIS, both flying on Nimbus-3, demonstrated the utility of IR radiances for characterizing the atmosphere. SIRS was similar to the earlier demonstration instruments built by ESSA. This instrument had a relatively coarse spatial resolution (100 km FOV) with a fixed nadir view, and 7 channels of 5 cm^{-1} resolution on the high frequency side of the CO_2 band at 667 cm^{-1}, and one window channel

[1] See Appendix A for a summary of all instruments mentioned in this section. Most references are omitted here for brevity, and can be found in the Appendix.

at 900 cm^{-1}. IRIS was a Fourier transform spectrometer, covering 400–2000 cm^{-1} at a spectral resolution of 5 cm^{-1}. ITPR flew on Nimbus-5, and used a filter radiometer similar to SIRS with 7 spectral channels. Two of the CO_2 sounding channels from SIRS were dropped and replaced with a water vapor FIR channel at 500 cm^{-1}, and a single channel at the higher frequency CO_2 absorption band at 2679 cm^{-1}. The ITPR was also the first such instrument to implement crosstrack scanning to gain better spatial coverage.

These early experimental instruments demonstrated the utility of spectral radiance measurements for temperature and water vapor sounding, and cross track scanning to improve spatial coverage. These experiments led directly into the development of operational instruments. The primary operational instruments included the Vertical Temperature Profile Radiometer (VTPR), the first operational sounding system on the Improved TIROS satellites, and the High resolution InfraRed Sounder (HIRS) instrument, first flown on Nimbus-6 and then continued as part of the operational TIROS Operational Vertical Sounding (TOVS) system on TIROS-N and later. The HIRS has been a key instrument for infrared sounding, from 1978 until the present day.

The design decisions made for these instruments show several general principles related to remote sensing of the atmosphere. The construction of a practical instrument must make certain tradeoffs, and the result will be a balance between five competing design characteristics: spatial coverage (i.e., crosstrack scanning versus nadir-only view), spatial resolution, spectral resolution, spectral coverage, and noise performance. The design goals must be balanced within cost and weight limitations for the satellite platform. Clearly if a certain noise performance is needed for a particular measurement, this may limit the spatial or spectral resolution, since these both can be tradeoffs with measurement noise (e.g., dividing the spectrum into finer spectral elements implies a lower signal to noise ratio for each sample). As technology advances, improvements can be made to any one of these aspects. Since the development of HIRS, there have been key improvements to spatial and spectral resolution. With spatial resolution, the previous generation imaging systems (e.g., the Very High Resolution Radiometer (VHRR) and Advanced VHRR (AVHRR)), always had superior spatial resolution relative to sounding instruments (1 or 4 km, compared to 17

km for HIRS). More recent technology applied in the MODerate resolution Imaging Spectrometer (MODIS) has increased the spatial resolution (from 4 to 1 km), and drastically improved the spectral coverage. Although MODIS is technically an imager, the spectral coverage is complete enough to do limited temperature and water vapor sounding.

For instruments dedicated to sounding, the spatial resolution has not increased, but the spectral resolution and coverage has increased dramatically with the deployment of high spectral resolution cross track scanning spectrometers. These instruments include the Atmospheric InfraRed Sounder (AIRS), a grating spectrometer with 0.4–2.0 cm^{-1} resolution; the Infrared Atmospheric Sounding Interferometer (IASI), a Fourier transform spectrometer with 0.5 cm^{-1} resolution, and the Cross-track scanning Infrared Sounder (CrIS), a Fourier transform spectrometer with 0.625 cm^{-1} resolution. All three instruments have similar overall spectral coverage (600–2500 cm^{-1}), with AIRS and CrIS having a few large gaps, and IASI covering the entire range. Broadly, these instruments can be called "hyperspectral" infrared sounders, due to the high spectral resolution ($\approx$ 1 cm^{-1} or better), and high number of spectral samples ($O(10^3)$ or more). The spatial resolution is similar to HIRS (approximately 15 km), but represents a large improvement over the original IRIS instruments (150 and 100 km), in addition to being cross track scanning. For the sounding mission, the spectral coverage has also increased by the fact that the spectrometers cover wide continuous swaths of the earth spectrum, rather than small targeted slices, as with HIRS. This increase in spectral coverage brings in a wealth of additional information for very low marginal cost, since by measuring the wide spectral swath, information about trace gas concentration, spectral cloud properties, and spectral surface emissivity will be present in the spectrum at the same time as the temperature and water vapor profile information. These different geophysical signals will be discussed in more detail in the next sections.

2.2 Applications of IR Sounder Data

The state of the art hyperspectral infrared sounders have shown to have a wealth of information about many geophysical properties. This section briefly reviews some of the literature documenting retrievals in the hyperspectral era, with emphasis on areas where the FIR will be relevant.

2.2.1 Sounding: measuring the vertical thermodynamic profile of the atmosphere

The original purpose for these instruments was to produce soundings of the temperature and water vapor profile. The satellite platform gives coverage in poorly instrumented areas, such as ocean basins or remote land areas. Soundings in these areas have a substantial impact on numerical weather prediction (NWP) models. The additional information in hyperspectral measurements has greatly increased the vertical resolution of the retrieved profiles, as well as reduced the retrieval error. At hyperspectral resolution, individual strong absorption lines can be resolved. This improves vertical resolution by introducing a wider range in weighting function altitudes, as well as sharpening individual weighting functions. One of the first studies comparing a low spectral resolution sounding measurement to a hyperspectral measurement compared HIRS to simulated Fourier transform spectrometer measurements (Purser and Huang, 1993), and showed an effective increase in data density of a factor of 2–3 along the full vertical profile. Similarly, retrieved profiles from HIRS data showed errors of approximately 2–2.5 K for clear sky soundings, (Susskind et al., 1984) and the hyperspectral measurements from AIRS show a reduction to 0.75–1.25 K, when comparing to independent "truth" measurements such as radiosondes (Susskind et al., 2006). The increased information also shows a positive impact on Numerical Weather Prediction (NWP) models (Hilton et al., 2009). The design goal of AIRS and other hyperspectral sounders is typically on the order of 1 K error, with a vertical resolution of 1 km; this is achievable in good conditions, but errors tend to increase over land where surface emissivity varies (Divakarla et al., 2006).

The total information content for water vapor tends to be somewhat lower. Humidity profiling from TOVS has enough information to profile on five broad layers, with pressure levels at 100, 300, 500, 700, and 850 hPa, with the last level at the surface (Chaboureau et al., 1998). For the AIRS retrievals, the number of layers in the standard retrieval is increased to 9, and shows an accuracy of up to 15% for clear conditions (Susskind et al., 2003, 2006), and 20%–40% when compared globally over all conditions where retrievals can be made (Divakarla et al., 2006).

2.2.2 Cloud Property Retrieval

Macrophysical cloud properties, such as cloud altitude (directly related to temperature), cloud fraction, and optical thickness, were not typically viewed as primary retrieved parameters from IR sounders, but it was known that some method to constrain these values would be required for successful thermodynamic profile retrievals. The temperature retrieval algorithms applied to the first experimental sounders (Smith et al., 1970; Chahine et al., 1977) had corrections for cloud effects, but typically the "retrieved" cloud properties were not utilized. Since these instruments typically had large footprints ($\sim 10^2$ km), the estimated cloud property represented some effective averaged quantity over the large area. Later instrumentation with much better spatial resolution, such as HIRS ($\sim$ 10 km), led to useful retrievals of these global cloud properties (Wylie et al., 1994).

Thermodynamic phase is also retrievable in the MIR due to the different shape of the spectral index of refraction for liquid water and ice. The primary feature is the increase in the imaginary part as the wavenumber decreases from 1000 cm^{-1}, which implies a drop in the in single scatter albedo of cloud particles. The slope is very different in liquid water versus ice. The spectral change in refractive index also implies a spectral change in the extinction efficiency. The bulk optical properties of a cloud layer will then have spectral features, dependent on the thermodynamic phase, that can be exploited by remote sensing techniques. The cloud could exhibit relatively more scattering, or relatively higher optical depth, across a pair of selected wavenumbers, which in turn may show a measurable brightness temperature difference. "Split window" approaches based on these principles can be used to determine phase in low spectral resolution measurements, since the variation of the index of refraction is slow (Figure 2.1), with features spread over $\sim 10^2$ cm^{-1} (Strabala et al., 1994; Baum et al., 2000).

More recent research has involved retrieval of the basic microphysical quantity, particle effective size, both from TOVS and hyperspectral IR measurements (Stubenrauch et al., 1999; Zhou et al., 2007). Because the spectral variation of cloud properties is much smoother than gas absorption lines, the high spectral resolution does not improve the retrieval nearly as much as for temperature and gas profile retrieval. At the same time, cloud spatial variation can be much more

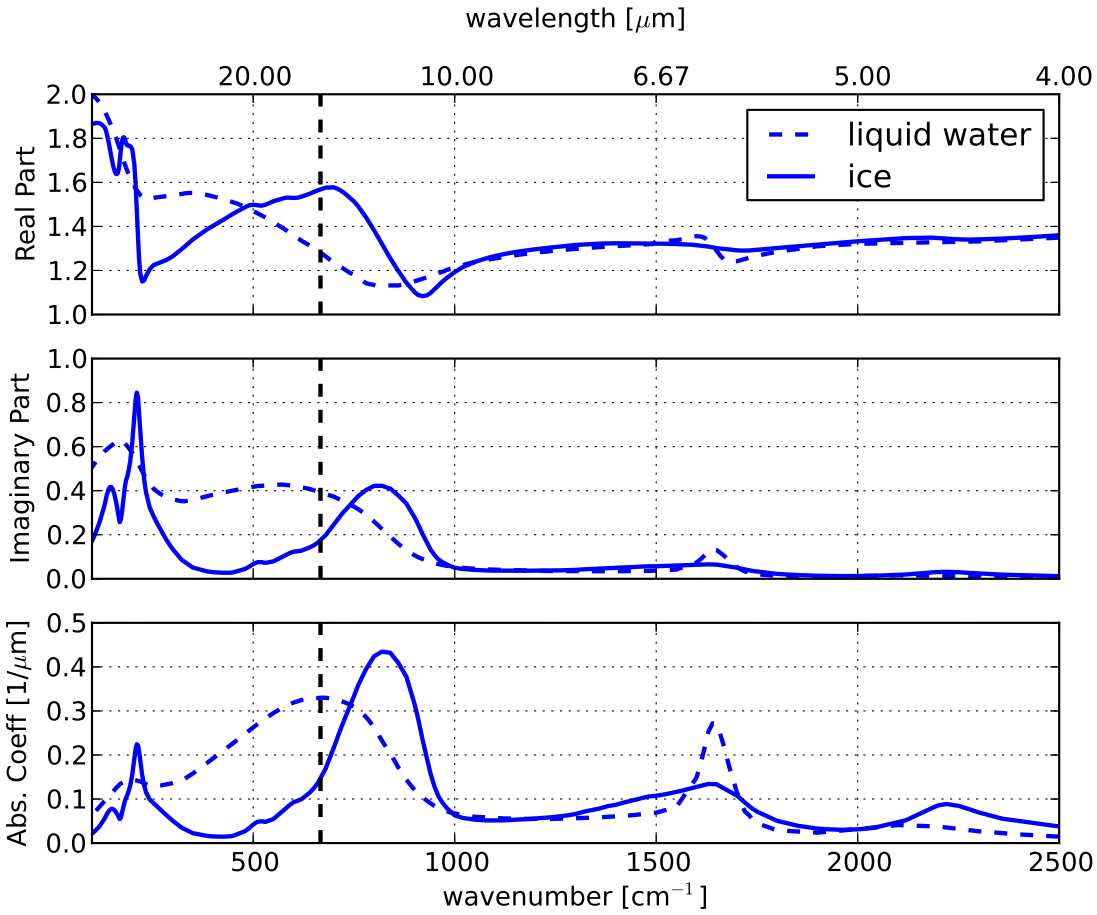

Figure 2.1 The complex index of refraction (real part, top; imaginary part, bottom) for bulk water and ice, in the FIR and MIR. The dashed vertical line shows the FIR-MIR division (667 cm^{-1}). Ice refractive index data from Warren and Brandt (2008), water refractive index data taken from Downing and Williams (1975).

dramatic than the spatial variation of absorbing gas species. Thus, retrievals from multiband imagers that leverage high spatial resolution (Inoue, 1985; Parol et al., 1991; Heidinger and Pavolonis, 2009), may outperform methods based on hyperspectral measurements due to the relatively poor spatial resolution of the hyperspectral sounder. Knowing the cases where each sensing method is more optimal is an active area of research, and retrievals that utilize both measurements should yield a superior result (Li et al., 2005; Nasiri et al., 2011).

2.2.3 Trace Gas Retrieval

Another significant impact of hyperspectral measurements is the ability to retrieve numerous gas species other than water vapor. These trace gas retrievals are impossible from the lower spectral resolution measurements, since the detection may rely on only a small number of individual absorption lines that are lost within the wider spectral band pass. For many trace gases, the information content in a cross track scanner may be fairly low, only allowing an estimate of total column amounts, because the total optical depth in the full atmosphere column may be too small. Profiling a particular gas requires a wide range of total optical depths, in order to produce weighting functions at different altitudes, which may not be physically possible for lower concentration species. Missions with the primary purpose of measuring trace gases are often limb sounders for this reason (for example, the Michelson Interferometer for Passive Atmospheric Sounding (MIPAS) on EnviSat). AIRS has shown useful information for O_3, CH_4, CO, and SO_2 (Chahine et al., 2006). IASI has continuous spectral coverage (650–2700 cm^{-1}) over wavenumbers where the AIRS has gaps, and superior spectral resolution in some bands (0.625 cm^{-1} over the whole spectrum, in contrast to AIRS which has a resolution of ~ 2 cm^{-1} in the highest wavenumber bands). With these new capabilities, IASI can detect all trace gases that are detected by AIRS as well as a number of additional gases. The list of documented detections of trace gases in IASI includes N_2O, NO_2, HNO_3, HCOOH, CH_3OH, and NH_3, as well as the water isotope HDO (Hilton et al., 2011).

2.2.4 Surface Emissivity

In low spectral resolution measurements, the surface emissivity can not be decoupled from the surface temperature. Hyperspectral measurements offer a key advantage by adding enough spectral information to enable retrieval of the surface spectral emissivity. (Knuteson et al., 2004a; Li and Li, 2008; Capelle et al., 2012). Many of the same considerations for clouds apply, namely that surface emissivity over land can have a large spatial variation that is not well sampled by the typical resolution of an infrared sounder. On the other hand, spectral variation of emissivity can be more complex than cloud properties, so the higher spectral resolution can be more useful for surface emissivity. Accounting for the surface emissivity spectral variation is also an important consideration for cloud property retrieval in window regions of the infrared spectrum, since errors in each can introduce bias errors in the other if not properly handled.

2.3 Key material properties in the FIR and relationships to remote sensing

2.3.1 Water Vapor absorption

The FIR water vapor absorption consists of the rotational mode absorption lines and continuum absorption. The rotational absorption band has the lowest energy, since no vibrational mode is excited. Thus the transition energies are small, and this band continues well into the microwave region. The peak line intensities are highest in this band, relative to any other vibrational-rotational absorption band (e.g., the first such band centered at 6.3 μm wavelength, or higher order transitions at shorter wavelengths) (Harries et al., 2008). The highest altitude weighting functions for upwelling radiance should appear in the FIR due to the increased line strengths.

The water vapor continuum absorption is still not fully explained in a firm theoretical framework, and has been described as caused by dimer interactions between two water vapor molecules, or due to subtle shape distortions to the Lorentz profile wings of the numerous absorption lines. Regardless of the physical basis, the semi-empirical method in the CKD and MT_CKD continuum models has been able to model the continuum shape quite well, by decomposing the total absorption into line contributions, and a smoothly "self" and "foreign" continuum (Clough et al.,

1989; Mlawer et al., 2012). The line contributions are defined to be Voigt functions within 25 cm^{-1} of either side of the line center, where the absorption coefficient is forced to zero at the $\pm$ 25 cm^{-1} points. Any residual absorption in the far wings of the line, or within the "basement" term in the center $\pm$ 25 cm^{-1} is then added into the continuum (Turner and Mlawer, 2010). The two continuum absorption components respond differently to pressure and water vapor density, so by modeling the components separately, they can have independent coefficients and scaling exponents. The so-called "self" continuum is proportional to the square of the water vapor density, while the "foreign" component scales linearly with water vapor density. The strength of the continuum absorption is highest in the FIR. All other factors being equal, the higher continuum absorption will tend to increase the weighting function altitude for the upwelling radiance weighting functions.

Earlier work involving sensitivity analysis of the IR spectra to perturbations in the water vapor concentration show the impact of the increased absorption. The magnitude of the water vapor Jacobian is stronger in the FIR water vapor rotational band by as much as a factor of 6 (Rizzi et al., 2002). However, this previous analysis does not consider any realistic impacts of sensor noise, spectral sampling, or correlation in spectral signatures, so the results are difficult to interpret in terms of actual retrievable water vapor profile information in a realistic measurement.

Validation of water vapor spectroscopy is an ongoing research effort. Both the line and continuum properties must be known as accurately as possible, since any errors can introduce bias into the retrieved profiles. Radiance closure studies have led to significant improvement in the water vapor absorption line properties as well as the continuum absorption using MIR measurements (Revercomb et al., 2003; Turner et al., 2004). More recent field campaigns have extended the applicability of these closure experiments, by collecting data in extremely dry conditions in order to measure farther into the FIR region where the line and continuum absorption strengths are higher (Turner and Mlawer, 2010). These new FIR measurements will lead to further refinement of water vapor spectroscopy.

2.3.2 Blackbody Peak Radiance and Spectral Cooling

An important aspect of FIR emission is the fact that the relative intensity of the blackbody curve is more strongly peaked in the FIR for cold atmospheric temperatures. Coupled with the fact that the water vapor absorption is stronger in the FIR relative to the MIR leading to higher altitude weighting functions, the majority of the upper atmosphere cooling to space occurs in the FIR region. From a remote sensing perspective, this implies a higher effective Signal to Noise Ratio (SNR) for retrieving geophysical information from the upper atmosphere water vapor emission, assuming constant measurement noise across the spectrum. Figure 2.2 shows the ratio between spectral radiance from a blackbody for various temperatures spanning the approximate range observed in the troposphere. Each curve is divided by the radiance from a T = 300 K blackbody. The significant radiance reduction in MIR wavenumbers is readily apparent, especially in the important wavenumber range for water vapor sounding in the upper troposphere (approximately 100–500 cm^{-1} for the FIR and 1250–1750 cm^{-1} for the MIR). For those ranges, the radiance at T = 200 K drops to approximately 40% (FIR) and 4% (MIR) of the the radiance at T = 300 K.

More detailed calculations were documented in Kratz (2002) using high spectral resolution radiative transfer codes. In clear sky conditions, the fraction of total outgoing longwave flux below 650 cm^{-1} ranges from 42.1% for the standard tropical atmosphere, to 53.7% in the standard subarctic winter atmosphere[2]. Limiting the calculation to consider only the flux from the atmosphere, these fractions increase to 51.1% and 75.5% for the two atmospheres, as a consequence of the emission peak favoring FIR wavenumbers for the colder troposphere temperatures where most of the atmospheric emission to space occurs. Finally, the spectral cooling rate calculations of Clough and Iacono (1995) show a strong maximum in spectral cooling in the FIR wavelengths through the mid and upper troposphere from water vapor emission lines. The cooling rate profile couples the radiative emission processes to dynamical processes, adding to the importance of accurate water vapor spectroscopy. General circulation models (GCMs) must include accurate parameterizations of these longwave radiation processes in order to produce useful simulations of climate. In the

[2]Note that this is slightly below the FIR boundary convention in this research (667 cm^{-1}) but the affect on these calculations should be small.

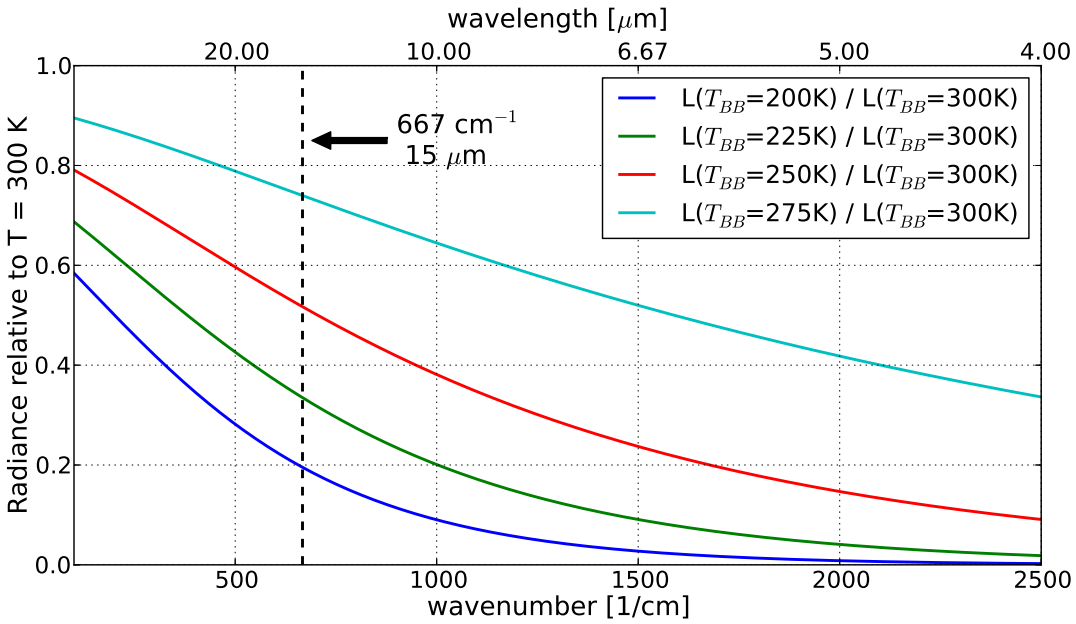

Figure 2.2 Ratio of black body radiance, relative to T = 300 K, for a set of temperatures to roughly span the typical range in the troposphere.

subtropics, for example, the clear sky radiative cooling is largely balanced by subsidence, so in this regime the cooling rate is directly tied to the large scale vertical motions in the atmosphere.

2.3.3 Ice and Water Index of Refraction

The spectral index of refraction for ice changes substantially in the FIR relative to the MIR (Figure 2.1). The imaginary part drops to a minimum around 400 cm^{-1}, while the water imaginary part stays elevated. Ice particles will then have much higher single scatter albedo, and cloud layers with ice will show much more scattering than water clouds. This spectral feature allows for sensitive phase detection beyond the MIR split window approaches (Rathke et al., 2002; Turner, 2005).

Phase determination is beyond the scope of this work, but the properties of ice clouds will be studied in detail in Chapter 5. The scattering maximum at 400 cm^{-1} is a key feature for remote sensing of cloud microphysics, since it introduces measurable changes in the bulk optical properties of ice clouds. Several papers have investigated this feature for ice cloud properties, using simplistic brightness temperature difference (BTD) measurements. BTD measurements are the typical starting points for split-window cloud property retrievals using bi- or tri-spectral measurements from moderate resolution infrared images (Strabala et al., 1994; Baum et al., 2000; Heidinger and Pavolonis, 2009), so these studies could be viewed as a motivation for adding an FIR channel to these types of instruments. In Yang et al. (2003), BTDs are simulated for a variety of cloud thicknesses in several standard atmosphere profiles. Large sensitivities are shown for a variety of cloud parameters, including very high optical depth clouds.

Another sensitivity study, based on spectral radiance differences rather than BTD (Baran, 2007), shows that FIR spectra can be sensitive to a number of important microphysical properties, such as particle effective diameter, Particle Size Distribution (PSD) shape, crystal habit, and vertical inhomogeneity within the cloud layer. The study is focused on sensitivity only, not retrievable information, so no consideration is made for sensor characteristics (other than a wavenumber

coverage to match a particular FIR research instrument, the Tropospheric Airborne Fourier Transform Spectrometer (TAFTS)), or correlation between spectral signatures. The analysis is also done only for a single macrophysical layout, namely a cloud with unit optical depth at z = 9.8 km.

2.3.4 Trace Gases

The information content for trace gas retrieval in the FIR is not well known. The FIR will probably not be as important for trace gas retrieval, as many species do not have a strong rotational band in the FIR (water vapor being the exception), and their strong rotational lines typically occur at lower frequencies (e.g. submillimeter or microwave). The lowest energy vibrational band typically occurs in the MIR. A simple visualization of the HITRAN database is shown in Figure 2.3, where the line intensities are multiplied by the column density in the US Standard Atmosphere to give the total line optical depth. In order to thin the data, the HITRAN data is grouped into 5 cm^{-1} spectral intervals, and only the strongest line for each species is displayed in the plot. The primary infrared absorbers water vapor, CO_2 and O_3 are ignored, and only species with at least one retained line with an optical depth greater than 10^{-3} are plotted. The most important trace gas in the FIR is N_2O, with a fairly strong absorption band (peak $\tau \approx 0.1$) at 550 cm^{-1}. The only other species with lines over 10^{-3} in optical depth in the FIR are HF, HCl and NH_3 with a few weak ($\tau \approx 3 \times 10^{-3}$) lines below 300 cm^{-1}. In fact, the lack of trace gas absorption can be a benefit to water vapor profile retrieval, since the water vapor signature is cleaner due to lack of interfering absorption lines. A detailed analysis of trace gas retrieval is beyond the scope of this work, so trace gases will not be discussed further, other than in reference to interference with water vapor absorption features in Chapter 4.

2.3.5 Surface Emissivity

Because of the high opacity of the water vapor rotational absorption band, the surface is not usually detectable within the FIR, except in cases of low water vapor column amounts. The state of knowledge for FIR spectral emissivities for natural surfaces is basically non-existent, except for measurements of mineral properties used in planetary geology. To support remote sensing of

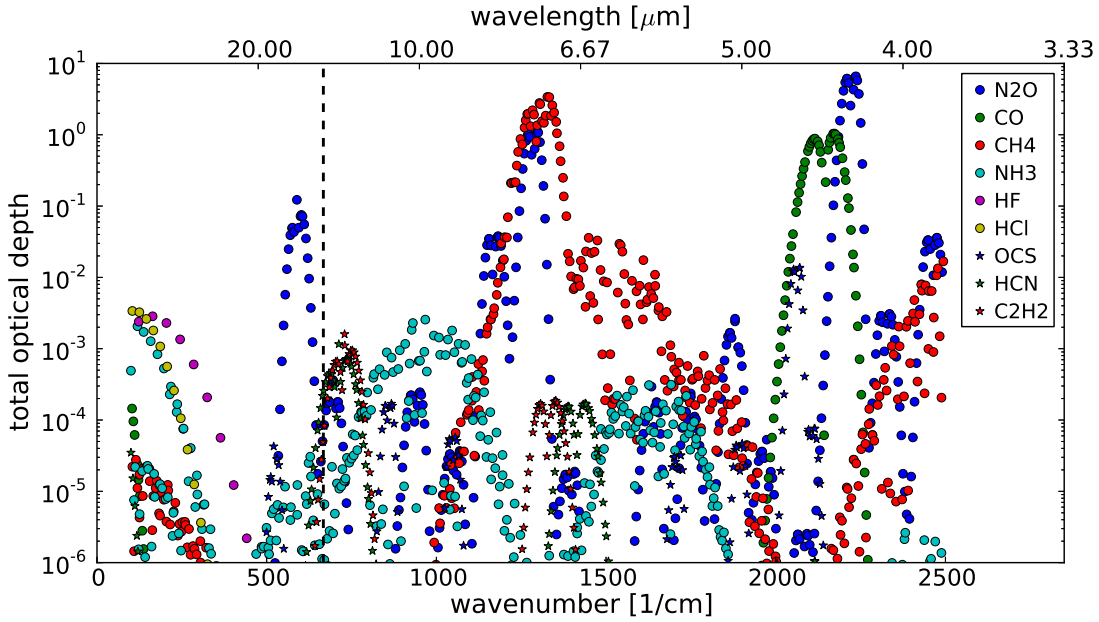

Figure 2.3 Integrated absorption line optical depth for a number of molecular species. The line intensities are taken from the HITRAN 2008 database (Rothman et al., 2009), and scaled by the molecular column density in the US Standard Atmosphere.

mineral distributions on the surface of Mars, laboratory measurements were made of many mineral and rock surfaces (Christensen et al., 2000). These reference spectra were used in the exploitation of THEMIS data (Christensen et al., 1992), a moderate resolution (5 cm^{-1}) interferometer covering the spectral range 200–1600 cm^{-1}. The laboratory data show that there is likely as much variation in the surface spectral emissivity in the MIR window due to land surface changes (e.g., rock or soil types), since there are strong features in the FIR correlated to features that are prevalent in global surface emissivity databases for MIR spectra (Seemann et al., 2008). Figure 2.4 shows the leading principal components of the global emissivity database, with two emissivity spectra from laboratory measurements of quartz and serpentine, two common minerals. The features at 1000–1200 cm^{-1} in the mineral spectra are seen in the Principal Components (PC) from the global database, which suggests that these features in the PC spectra are likely due to the same minerals. This would suggest the strong emissivity features in the FIR seen in the mineral spectra may be important for any FIR remote sensing in dry atmospheres where the surface is detected.

2.4 Future Directions

The infrared sounder has been a critical part of the overall earth observing system for many decades, and over time the number of applications for the data continues to grow. Sounders will continue to be a key component for the foreseeable future, and they will likely be enhanced in capability in a number of ways. For the operational sounder, where the instrument design can have a lifetime measured in decades (over multiple constructed examples), the current EUMETSAT and NOAA designs for polar orbiters (IASI and CrIS) are in the middle and beginning of their lifetimes, respectively, so there is no concrete design for the next generation sounder. The follow-on EUMETSAT system, IASI-NG (Next Generation), is in design phase. The current instrument plan includes higher spectral resolution and lower sensor noise, but uses the same spectral coverage (Crevoisier, 2012).

There are several promising directions for hyperspectral instrumentation development on geosynchronous satellites, such as the infrared sounder on the third generation MeteoSat (Stuhlmann et al.,

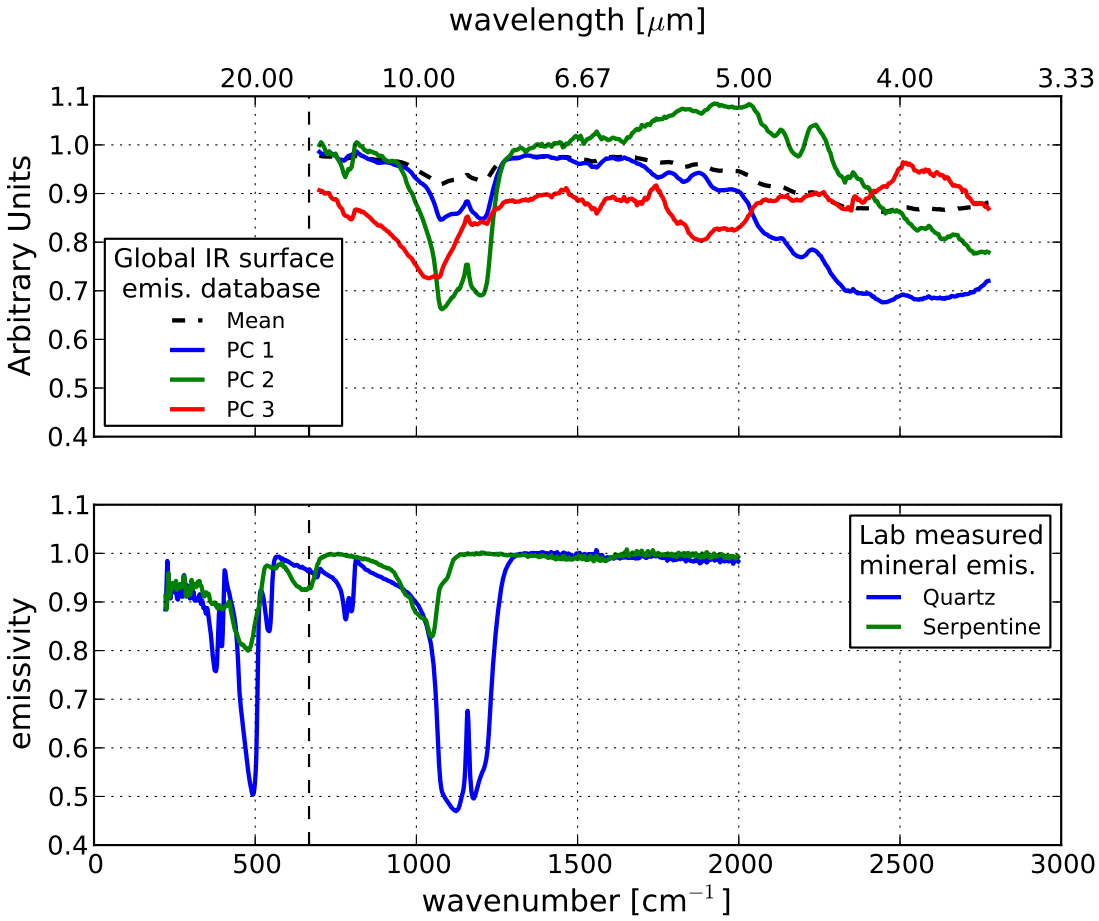

Figure 2.4 Top figure: The mean spectral emissivity, along with the first 3 Principal Components, from the emissivity library in Seemann et al. (2008) that describes a global emissivity distribution for remote sensing applications in the MIR. Bottom figure: laboratory emissivity spectra of quartz and serpentine from Christensen et al. (2000), showing strong features in the MIR and FIR.

2005), or potential missions based on the Geosynchronous Imaging Fourier Transform Spectrometer (GIFTS) instrument (Elwell et al., 2006). This would follow the pattern of the sounding technology in operational use on polar platforms for some length of time before transitioning to a geosynchronous platform.

Another possible route would be to expand spectral coverage again, by pushing the spectrometers to measure lower frequencies, and cross into the FIR region. The original IRIS instrument did observe frequencies as low as 400 cm^{-1}, but the current hyperspectral instruments all have a cutoff at about 650 cm^{-1}. The focus of this dissertation is to explore what advantage could be realized by extending the IR sounding measurement into the FIR, to a low cutoff wavenumber of 100 cm^{-1}. The information content for cloud microphysical property and sounding – both temperature and water vapor – is studied, using high accuracy forward models and physical retrieval frameworks.

2.5 Summary

This chapter gave a brief history of passive IR sounding systems from satellites, showing the push toward higher spatial resolution and spectral coverage among imaging systems, and the dramatic increase in spectral resolution among sounding instruments. The key applications of hyperspectral IR sounders were reviewed. Unique material properties in the FIR were discussed, focusing on water vapor absorption characteristics, and ice spectral index of refraction. These unique FIR properties affect thermodynamic profile and ice cloud property retrievals. The following chapters form the core of this thesis. First, in Chapter 3, the retrieval algorithms, radiative transfer models, and other modeling framework details are described. In Chapter 4, the thermodynamic profile retrieval problem is investigated, by computing the information content using hyperspectral measurements of the upwelling MIR and FIR spectra. In Chapter 5, the work is extended to include layer ice clouds, to investigate the impact of the FIR ice scattering properties. Finally, in Chapter 6, some applications of FIR radiative transfer and remote sensing are described, along with a brief summary of prospects for future research in this area.

Chapter 3

Methods[1]

This work uses the well known Optimal Estimation (OE) (Rodgers, 2000) algorithm to solve the inverse problem of retrieving geophysical data from infrared radiance spectra. In this chapter, the OE mathematical framework is first reviewed. Once the mathematical quantities are defined, the specific implementation details are described. First, the forward models are discussed, followed by specific details of various components such as assumed priors and sensor characteristics. When possible, framework is applied in an identical manner to both the clear sky and cloudy conditions. Differences between the clear sky and cloudy calculations are noted.

3.1 Algorithms

3.1.1 Optimal Estimation (OE)

Optimal Estimation is a Bayesian solution to the inverse problem. OE produces the maximum likelihood solution under the assumptions that the forward model is linear and the error covariances have Gaussian probability distribution functions. The method has many useful properties for the inverse problem at hand, such as the ability to quantify the prior knowledge used in the retrieval; calculation of error estimates on the final solution; and robustness to measurement errors. The disadvantage is mainly the computational expense. In some cases the requirement of prior information can be a disadvantage if such information is difficult to obtain. Highly nonlinear models or

[1] Portions of this chapter were published in Merrelli and Turner (2011) and are copyright of the American Meteorological Society.

non-Gaussian error covariances may be unsuitable for OE as these can introduce large bias errors in the solution.

The OE method can be defined with the following terms, which follow the notation used in Rodgers (2000). Given a m-dimensional measurement vector $\mathbf{y}$ and a n-dimensional state vector $\mathbf{x}$, the two spaces can be related via a function F, the "forward model", with error ϵ from measurement uncertainty and forward model errors. Typically this is expressed relative to a specific state vector value, $\mathbf{x}_0$, and the forward model evaluated at that state vector value, $F(\mathbf{x}_0)$:

$$\mathbf{y} - \mathbf{y}_0 = F(\mathbf{x}) - F(\mathbf{x}_0) + \epsilon \tag{3.1}$$

The expression can be linearized by replacing the function with its Taylor expansion and retaining only the linear term. The linear term contains the first derivative of the forward model, the Jacobian matrix ($K_{i,k} = \partial F_i / \partial x_k$). The linearized forward model equation using the Jacobian matrix can be written as

$$\mathbf{y} - \mathbf{y}_0 = \mathbf{K}(\mathbf{x} - \mathbf{x}_0) + \epsilon \ + \ (\text{higher order terms}) \tag{3.2}$$

If the prior covariance for the state vector ($\mathbf{S}_\text{a}$) and the error covariance ($\mathbf{S}_\text{e}$) are both known, then the OE solution for the linear case can be expressed as

$$\hat{\mathbf{x}} \ = \mathbf{x}_0 + \left(\mathbf{K}^T \mathbf{S}_\text{e}^{-1} \mathbf{K} + \mathbf{S}_\text{a}^{-1}\right)^{-1} \mathbf{K}^T \mathbf{S}_\text{e}^{-1} \left[\mathbf{y} - F(\mathbf{x}_0)\right] \tag{3.3}$$

where the solution $\hat{\mathbf{x}}$ is called the "state estimate" for the observation $\mathbf{y}$. In this equation, the error covariance $\mathbf{S}_\text{e}$ includes the measurement noise for the instrument measuring $\mathbf{y}$ and some estimate of the error in the forward model. Since these two covariances would be added together to form $\mathbf{S}_\text{e}$ in the cases where model error is included, the error covariance could be split into two terms:

$$\mathbf{S}_\text{e} = \mathbf{S}_y + \mathbf{S}_F \tag{3.4}$$

where $\mathbf{S}_y$ represents the covariance of the measurement noise, and $\mathbf{S}_F$ represents the covariance of the model error.

The measurement noise is usually obtained by an independent method, for example calibration data collected by the instrument independently from the observation $\mathbf{y}$. The model error is

typically much more difficult to characterize, since it includes errors due to missing or unknown physics relevant to the prediction of the measurement from the given state vector. Some model errors may have quantified uncertainties. For example, absorption line widths or center frequencies may have measured or estimated uncertainties. In most cases with real data these model errors will be unquantified, since the errors will be due to unaccounted physical properties. Examples include three dimensional scattering effects in cloud fields represented by a one dimensional forward model, or unaccounted aerosol layers in a clear sky radiance simulation. In many cases the model error is assumed to be a constant additive variance (uncorrelated noise) (Zhou et al., 2007).

Since this research uses the independent pixel assumption, and a forward model that describes clouds as homogeneous layers, the important model errors will likely be three dimension cloud scattering effects as well as multiple layer and subpixel cloud fraction effects. These effects are beyond the scope of this research, but it should be noted that this is an active area of research within the larger community (Kahn et al., 2011). However, within the framework used in this research, since the same forward model used in the OE algorithm is the same forward model used to simulate measurements, the model error component $\mathbf{S}_F$ is zero. This is sometimes called the "perfect model" condition. In some specific test cases in Chapter 4 a model error will be simulated by including a difference between the model that simulates the measurement and the model that is used inside the OE retrieval to compute $F(\mathbf{x})$ and $\mathbf{K}$. In those specific cases, the perfect model condition will not be applicable.

To extend the linear solution to nonlinear problems, the linear equation can be applied in an iterative algorithm. The state estimate and Jacobian are recomputed at each iteration:

$$\hat{\mathbf{x}}_{i+1} = \mathbf{x}_0 + \left(\mathbf{K}_i^T \mathbf{S}_\mathrm{e}^{-1} \mathbf{K}_i + \mathbf{S}_\mathrm{a}^{-1}\right)^{-1} \mathbf{K}_i^T \mathbf{S}_\mathrm{e}^{-1} \left[\mathbf{y} - F(\hat{\mathbf{x}}_i) + \mathbf{K}_i(\hat{\mathbf{x}}_i - \mathbf{x}_0)\right] \tag{3.5}$$

In this equation $\mathbf{K}_i$ represents the Jacobian computed at the state estimate $\hat{\mathbf{x}}_i$. The iteration continues until some exit criterion is reached. In this work, the exit criterion is based on the change in the state estimate compared to the size of the posterior error. Using the definition of the posterior error, $\hat{\mathbf{S}}$, the change in state estimate is scaled and compared to $0.1\ N$. This threshold is similar to

a 0.1 σ threshold for a scalar random variable, but generalized to N-dimensional state space:

$$\begin{aligned} \hat{\mathbf{S}}^{-1} &= \mathbf{K}_i^T \mathbf{S}_{\mathrm{e}}^{-1} \mathbf{K}_i + \mathbf{S}_{\mathrm{a}}^{-1} \\ 0.1 &> \frac{1}{N} (\hat{\mathbf{x}}_{i+1} - \hat{\mathbf{x}}_i)^T \hat{\mathbf{S}}^{-1} (\hat{\mathbf{x}}_{i+1} - \hat{\mathbf{x}}_i) \end{aligned} \tag{3.6}$$

This nonlinear form of OE, Newton's method, is used for all retrievals. An implicit assumption must be made that the prior and measurement covariances are Gaussian, and that the forward model is "mildly nonlinear" (Rodgers, 2000). These assumptions are difficult to verify in practice, and are beyond the scope of this research. Instead, it will be noted that the method has been successfully applied to numerous data sources in atmospheric science, including infrared sounding instruments (for example, TOVS (Eyre, 1989), IASI (Carissimo et al., 2005), and AERI (Turner, 2005)).

3.1.2 OE Based Metrics

There are three important intermediate matrices computed in the Bayesian solution which are used throughout this research to quantify various aspects of the retrieved state estimate. These matrices are $\hat{\mathbf{S}}$, the posterior state covariance; $\mathbf{G}$, the gain matrix, or the generalized inverse of $\mathbf{K}$; and $\mathbf{A}$, the averaging kernel matrix.

$$\hat{\mathbf{S}} = \left(\mathbf{K}_i^T \mathbf{S}_{\mathrm{e}}^{-1} \mathbf{K}_i + \mathbf{S}_{\mathrm{a}}^{-1} \right)^{-1} \tag{3.7}$$

$$\mathbf{G} = \left[\left(\mathbf{K}_i^T \mathbf{S}_{\mathrm{e}}^{-1} \mathbf{K}_i + \mathbf{S}_{\mathrm{a}}^{-1} \right)^{-1} \mathbf{K}_i^T \mathbf{S}_{\mathrm{e}}^{-1} \right] = \hat{\mathbf{S}} \mathbf{K}_i^T \mathbf{S}_{\mathrm{e}}^{-1} \tag{3.8}$$

$$\mathbf{A} = \left[\left(\mathbf{K}_i^T \mathbf{S}_{\mathrm{e}}^{-1} \mathbf{K}_i + \mathbf{S}_{\mathrm{a}}^{-1} \right)^{-1} \mathbf{K}_i^T \mathbf{S}_{\mathrm{e}}^{-1} \right] \mathbf{K}_i = \mathbf{G} \mathbf{K}_i \tag{3.9}$$

The posterior state covariance represents the uncertainty of the state estimate after exploiting the information contained within the measurement. Measurements with low uncertainty should shrink the volume of the prior state covariance substantially, so that the posterior state covariance will cover a much smaller volume in state space. The amount of reduction can be examined by simply looking at the square root of the diagonal, to get effectively a 1-σ uncertainty level on the state estimate, and comparing this to the 1-σ uncertainty in the prior covariance. Correlated error in the state estimate would be ignored by this simple method, but it has the advantage of describing the error in a simple way in terms of physical units.

The Shannon information content, H, is related to the posterior and prior state covariances through the relation

$$H = -\frac{1}{2} \ln \left| \hat{\mathbf{S}} \mathbf{S}_{\mathrm{a}}^{-1} \right| \tag{3.10}$$

Because the posterior covariance always describes a smaller volume of state space, the sign convention implies H is a positive quantity. In an approximate sense, H represents the reduction in state space in the posterior relative to the prior. The determinant of a covariance matrix is sometimes called the "generalized variance" since it represents the volume of the associated error distribution. If the covariance matrices are of full rank, H can be rewritten in a form that suggests an analogy to the scalar signal to noise ratio:

$$H = -\frac{1}{2} \ln \left(\left| \hat{\mathbf{S}} \right| \left| \mathbf{S}_{\mathrm{a}}^{-1} \right| \right) = -\frac{1}{2} \ln \left(\frac{\left| \hat{\mathbf{S}} \right|}{|\mathbf{S}_{\mathrm{a}}|} \right) \tag{3.11}$$

The averaging kernel describes the amount of correlation between state vector components. By approximating $\mathbf{y}$ with the linearization of F, $\mathbf{y} = \mathbf{K}(\mathbf{x} - \mathbf{x}_0) + F(\mathbf{x}_0)$, replacing this term in equation 3.3 and rearranging, the following expression relating the true state $\mathbf{x}$ and the state estimate $\hat{\mathbf{x}}$ is obtained:

$$\hat{\mathbf{x}} - \mathbf{x}_0 = \mathbf{A}(\mathbf{x} - \mathbf{x}_0) + \mathbf{G}\epsilon \tag{3.12}$$

This equation gives several perspectives on the action of $\mathbf{A}$ on the true state $\mathbf{x}$. Considering a δ-function like true state (meaning, the true state differs from $\mathbf{x}_0$ at only one state variable x_k), then column of $\mathbf{A}$ at this index k represents the response in the state estimate. The response will be smeared out according to the correlation to other state variables, which arises from correlation inherent in the assumed prior covariance and in the character of the measurement as described by $\mathbf{K}$. For a general true state, the response in the state estimate for state variable k will be the scalar product between the corresponding row of $\mathbf{A}$ and the true state $\mathbf{x} - \mathbf{x}_0$. The rows can be thought of as "averaging kernels", since the k^{th} element in the state estimate represents an average over multiple elements in the true state, according to the k^{th} row in $\mathbf{A}$. The summed elements across the k^{th} row also gives an indication of the relative weight of the prior state and measurement in the calculation of the state estimate. A row sum near zero indicates that the corresponding

state variable estimate $\hat{x}_k$ will tend to be equal to the prior mean value $x_{0,k}$, regardless of the measurement. This indicates that the measurement is not sensitive to that state variable either directly or through any correlation implied by the prior covariance.

Examining the rows of $\mathbf{A}$ in cases where the state vector represents a vertical thermodynamic profile shows important information about the effective vertical resolution of the state estimate. One easy way to represent this resolution is to calculate the Full Width, Half Maximum (FWHM) of the averaging kernel. Simple linear extrapolation between points in the averaging kernel produces an estimate of FWHM that is not quantized by the level grid in the state vector. Figure 3.1 shows such a calculation for an averaging kernel for water vapor and temperature profiles. For cases where the state vector is not a vertical profile, the averaging kernel will represent the amount of correlation between different variables in the state estimate.

The other key metric related to the $\mathbf{A}$ matrix is the Degrees of Freedom for Signal (DFS). The DFS is equal to the trace of $\mathbf{A}$. It represents the amount of independent information in the state estimate that comes from the measurement vector. For profile retrieval, this quantity can be considered as an estimate of the number of retrievable vertical levels in the measurement. In this research, the DFS will be the preferred metric, rather than the Shannon information content H.

The aim of OE is to obtain an averaging kernel that is as close to the identity matrix as possible, while reducing the effect of measurement error through the term $\mathbf{G}\epsilon$. A tradeoff is made between reducing the amplitude of the error in the state estimate, and improving the resolution or reducing correlation in the state estimate. The OE framework as described here allows this tradeoff to be made by selection of different prior covariances. High amplitude, uncorrelated prior covariances tend to reduce correlation and increase resolution in the state estimate, at the cost of increased error and potential instability in algorithm convergence. Lower variance, higher correlation priors will reduce noise but produce higher correlation and lower vertical resolution in the state estimate.

3.1.3 OE Channel Selection

The same OE mathematical framework can also be used to optimally select a subset of the full hyperspectral channel list. Two approaches based on Rodgers et al. (1996) can be used. For

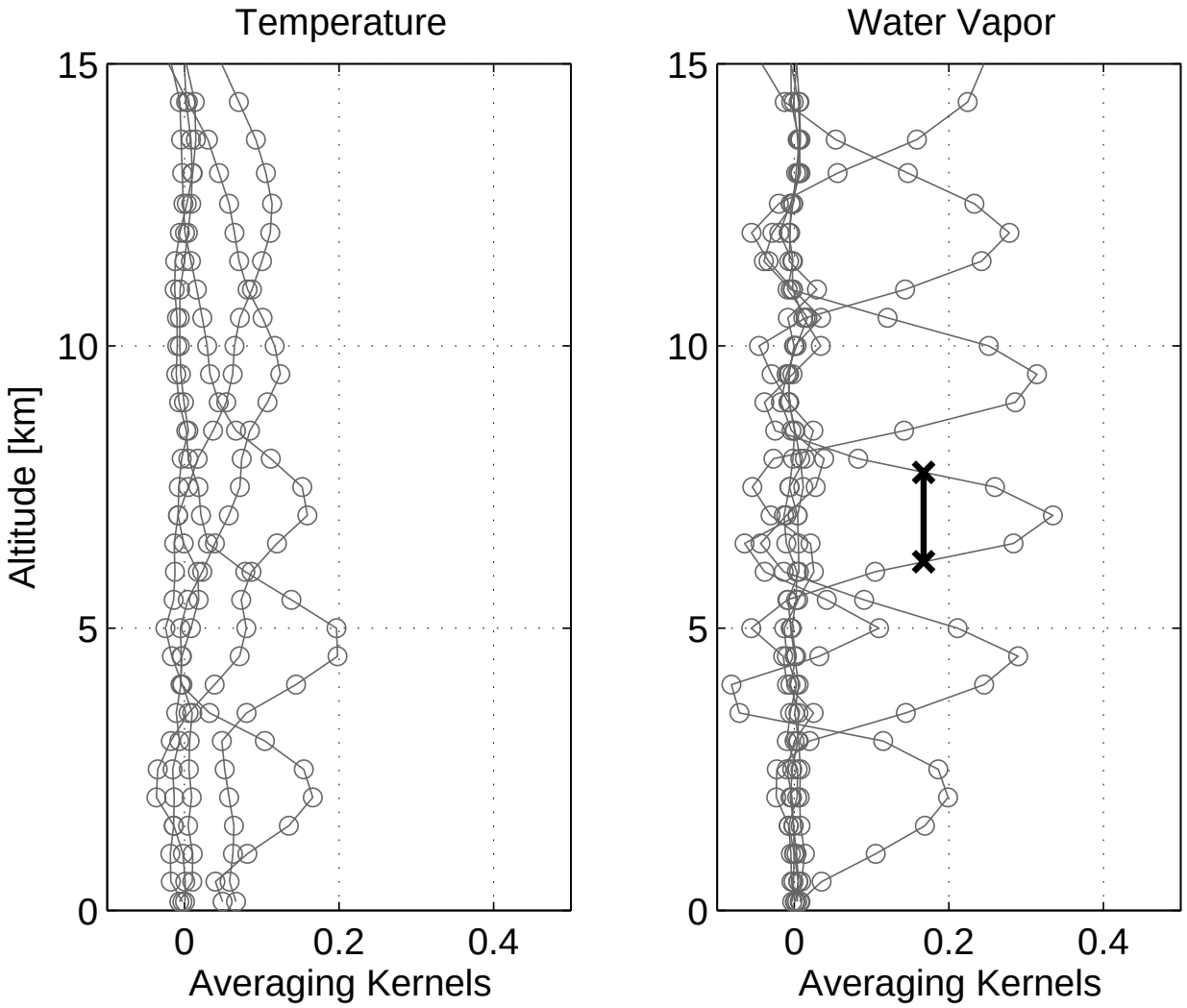

Figure 3.1 Example Averaging Kernels for temperature and water vapor retrievals. Only every fifth kernel is plotted for brevity. The solid vertical black line segment illustrates the calculation of the FWHM for that kernel. Figure from Merrelli and Turner (2011).

the first method, the DFS of each channel is computed directly. The first channel is selected by looping over all m channels, computing the DFS for each individual channel, and selecting the maximum. The posterior covariance is computed with an alternate form that is computationally simpler for this algorithm. It involves inverting a square matrix of size equal to the number of selected channels (s), and requires one less matrix inversion than the form in equation 3.5. For the c^{th} channel,

$$\hat{\mathbf{S}}_c = \mathbf{S}_\text{a} - \mathbf{S}_\text{a}\mathbf{K}_c^T \left(S_{\text{e},c} + \mathbf{K}_c\mathbf{S}_\text{a}\mathbf{K}_c^T\right)^{-1} \mathbf{K}_c\mathbf{S}_\text{a} \tag{3.13}$$

$$\mathbf{A}_c = \hat{\mathbf{S}}_c\mathbf{K}_c^T S_{\text{e},c}^{-1}\mathbf{K}_c \tag{3.14}$$

where the term $\mathbf{K}_c$ refers to the single row vector from $\mathbf{K}$ for channel c, and $S_{\text{e},c}$ refers to the variance of channel c (a scalar). The subscript c on the posterior covariance signifies that this is the posterior related to that specific channel. The DFS is computed normally ($\text{trace}(\mathbf{A}_c)$), and the channel with the maximum DFS is selected. Later channels are selected in the same manner. First the matrix $\mathbf{K}_s$, is created, containing the rows of $\mathbf{K}$ for the s already selected channels. This matrix is augmented by adding one additional row corresponding to one channel from the remaining $m-s$ unselected channels. A similar operation constructs the covariance $\mathbf{S}_{\text{e},s}$, which is then augmented by one of the remaining $m-s$ unselected channels. This produces an array of $m-s$ DFS values, as the calculation is repeated for each of the $m-s$ channels. Subtracting the DFS value from the s already selected channels yields the increase in DFS by adding any one of the unselected channels, though this is not needed for the channel selection step as the maximum DFS or maximum DFS increment would produce the same selection.

This approach works for any form of $\mathbf{S}_\text{a}$ or $\mathbf{S}_\text{e}$, but is quite time consuming due to the nested loops (looping over $m-s$ channels for each selection of the s desired channels) and the matrix inversion at each iteration. The second approach is more computationally simple but requires that the error covariance $\mathbf{S}_\text{e}$ is diagonal. By first pre-scaling $\mathbf{K}$ by $\mathbf{S}_\text{e}$ and $\mathbf{S}_\text{a}$, yielding $\mathbf{K}'$,

$$\mathbf{K}' = \mathbf{S}_\text{e}^{-1/2}\mathbf{K}{\mathbf{S}_\text{a}}^{1/2} \tag{3.15}$$

then the DFS added by channel c, $\delta\mathrm{DFS}_c$, after a selection of s channels becomes a simple scalar vector product (Rodgers et al., 1996):

$$\delta\mathrm{DFS}_c = \frac{(\hat{\mathbf{S}}_s\mathbf{k}_c^T)^T(\hat{\mathbf{S}}_s\mathbf{k}_c^T)}{1+\mathbf{k}_c\hat{\mathbf{S}}_s\mathbf{k}_c^T} \tag{3.16}$$

where $\hat{\mathbf{S}}_s$ is the posterior state covariance including the already selected s channels, and $\mathbf{k}_c$ is the row from $\mathbf{K}'$ for channel c, which is under consideration for selection as channel $s+1$. After this product is computed for all possible $m-s$ channels, the channel with the maximum $\delta\mathrm{DFS}$ is selected, and the posterior state covariance is updated to include the newly selected channel:

$$\hat{\mathbf{S}}_{s+1} = \hat{\mathbf{S}}_s\frac{\mathbf{I}-\mathbf{k}_c(\hat{\mathbf{S}}_s\mathbf{k}_c)^T}{1+\mathbf{k}_c^T\hat{\mathbf{S}}_s\mathbf{k}_c} \tag{3.17}$$

The optimized second approach is used where possible, which depends on whether a diagonal matrix is assumed for $\mathbf{S}_\mathrm{e}$.

Regardless of which calculation is used, the iterative selection algorithm is typically run until some desired fraction of the total DFS is reached. A single DFS calculation over the entire channel set is performed first, so then the running total DFS over the s selected channels can be converted to a DFS fraction. Because of the optimal selection, the majority of the total DFS ($> 90\%$) can typically be reached after selecting approximately 20% of the channels.

3.2 Forward Models

3.2.1 LBLRTM

The Line-By-Line Radiative Transfer Model (LBLRTM, Clough et al. (2005)) is a well validated model developed at Atmospheric and Environmental Research (AER). This work uses version 11.6 and 11.7 of the model; the differences between the models do not significantly impact this study. Most changes occurred in the high wavenumber end of the spectrum (above 2000 cm^{-1}). Some water vapor absorption lines in the wavenumber range 400–2000 cm^{-1} were modified, but these changes were minor and result in maximum changes of 0.05 K brightness temperature for a standard tropical atmosphere. The LBLRTM is used to compute the radiance for all clear sky

cases. It has the added capability to compute analytic Jacobians for surface temperature, emissivity, profile temperature, and concentrations profiles of any of the absorbing gas species used in the calculation. The line absorption data is derived primarily from HITRAN2004 (Rothman et al., 2005), with various updates to certain line data as determined by AER. In addition, LBLRTM allows for a Instrumental Line Shape (ILS) to be applied to the monochromatic simulated radiance, to produce a simulated observation from a specified Fourier transform spectrometer with one of a number of possible ILS functions. In all simulations, the top 7 HITRAN molecules are used. In order, these are: H_2O, CO_2, O_3, N_2O, CO, CH_4, and O_2.

3.2.2 LBLDIS

The LBLDIS (LBLrtm DISort) model (Turner, 2005) is used to compute all radiances and Jacobians for cloudy sky profiles. LBLDIS uses gaseous optical depth data computed from LBLRTM to describe the spectral absorption due to gas absorption lines. This optical depth data is computed at monochromatic resolution by LBLRTM, and averaged within spectral increments by LBLDIS. The layer-to-instrument transmittance is computed at the monochromatic resolution, and then averaged within the defined spectral increments. The averaged transmittance is then converted back to an effective layer optical depth within the coarse spectral grid. LBLDIS uses DIScrete Ordinate Radiative Transfer (DISORT, Stamnes et al. (1988)) to compute the scattering and absorption through a cloud layer embedded within the atmosphere profile. The LBLDIS expects an input scattering property database which describes the bulk scattering of the cloud particles, meaning the various scattering parameters (single scatter albedo, phase function, extinction efficiency) should represent the size distribution weighted quantities.

Each layer cloud is defined at one vertical level. The cloud particles are assumed to be vertically homogeneous within the layer that contains the input cloud level, where the layering is defined by the pre-computed LBLRTM gaseous optical depth. For example, if the LBLRTM optical depth is computed on a layer grid defined by levels every 1 km from the ground level, placing a cloud at z = 4.5 km above ground in LBLDIS implies a 1 km thick, homogeneous cloud layer defined by the levels at z = 4 km and z = 5 km.

A spectral grid consisting of a constant spectral increment between start and stop wavenumber is used for all LBLDIS calculations. As long as the spectral grid is not too coarse, the resulting spectrum should approximately represent an interferometer with a rectangular ILS function.

3.3 Framework Details

In Section 3.1.1, the key input terms in the OE mathematical framework are defined: the state vector $\mathbf{x}$, the prior state $\mathbf{x}_a$ and its covariance $\mathbf{S}_\mathrm{a}$, the forward model $F(\mathbf{x})$ and its Jacobian $\mathbf{K}(\mathbf{x})$, the measurement covariance $\mathbf{S}_y$, and the model error $\mathbf{S}_F$. In this section, each of these terms is described in detail in their usage and application in the present study.

3.3.1 State Vector

The state vector contains all geophysical parameters that will be retrieved in the OE algorithm. For the clear sky problem, this vector contains the surface temperature, profile temperature, and the logarithm of the concentration of any gas absorbers that are included in the retrieval. The logarithm of the concentration is used because the effect of gas absorption on simulated radiance is closer to a logarithmic rather than linear variation. In addition, the profile variation of some species (water vapor in particular) covers many orders of magnitude, so for numerical issues it is preferable to reduce the range in values covered by the state vector by using the logarithm.

Since the thermodynamic and gas concentration profiles are physically continuous variables, there is freedom to select the level grid for the state space vector (the "design points"). The primary a priori data sources for the prior profiles are the radiosonde climatologies described in the next section and the standard atmosphere profiles (Anderson et al., 1986). The vertical sampling grid in radiosonde profiles is irregular due to the random nature of the balloon ascent. The vertical resolution is also very high, with spacing between samples of order 10–100 m. Each profile is initially interpolated onto a common grid with 20 m vertical spacing to facilitate processing. This is far too high a vertical resolution for the design point selection, partly because of computational limitations within the forward model (LBLRTM is limited to < 200 layers), and partly because the

vertical resolution of the retrieval itself is poor relative to the radiosonde data. Applying the information density analysis of Purser and Huang (1993) to these data shows a maximum of roughly 0.5 km^{-1} in the middle troposphere with a rapid decrease above 12 km in altitude. Using this metric as a guideline, the design points for the vertical profile are selected with the level spacing in the troposphere at 0.5 km (implying a resolution of 2.0 km^{-1}). Above 11 km, the spacing increases smoothly, up to a maximum of 2.6 km at the last level, at an altitude of 31.9 km. In total, there are 40 levels from 0–31.9 km.

For cloudy profiles, additional parameters describing the layer cloud are added. The macrophysical properties cloud height and visible optical depth are included in all cases. The microphysical properties include parameters describing the particle size distribution. These will be covered in more detail in Chapter 5.

3.3.2 Prior State and Covariance

For the atmospheric profiles, the prior states are defined in two ways: selecting a profile with a synthetic covariance matrix, or selecting a profile with a covariance matrix derived from a radiosonde climatology.

In the first method, the prior mean state is selected, typically from one of the standard atmosphere profiles (Anderson et al., 1986). The inter-level correlation is then assumed to follow a simple exponential decay as a function of level separation. In the most general sense, the a priori covariance as a continuous function of z would be expressed as:

$$S_{\mathrm{a}}(z_i, z_j) = \sigma(z_i)\sigma(z_j)e^{-\left|\frac{z_i - z_j}{L(i,j)}\right|} \tag{3.18}$$

By discretizing the z coordinate, and assuming a fixed scale length L, the discrete covariance matrix $S_{a;i,j}$ is:

$$S_{\mathrm{a};i,j} = \sigma_i\sigma_j e^{-\left|\frac{z_i - z_j}{L}\right|} \tag{3.19}$$

For this simplified covariance matrix, no correlation is assumed between the different profile variables, meaning no correlation between temperature and water vapor (or any other constituent). An

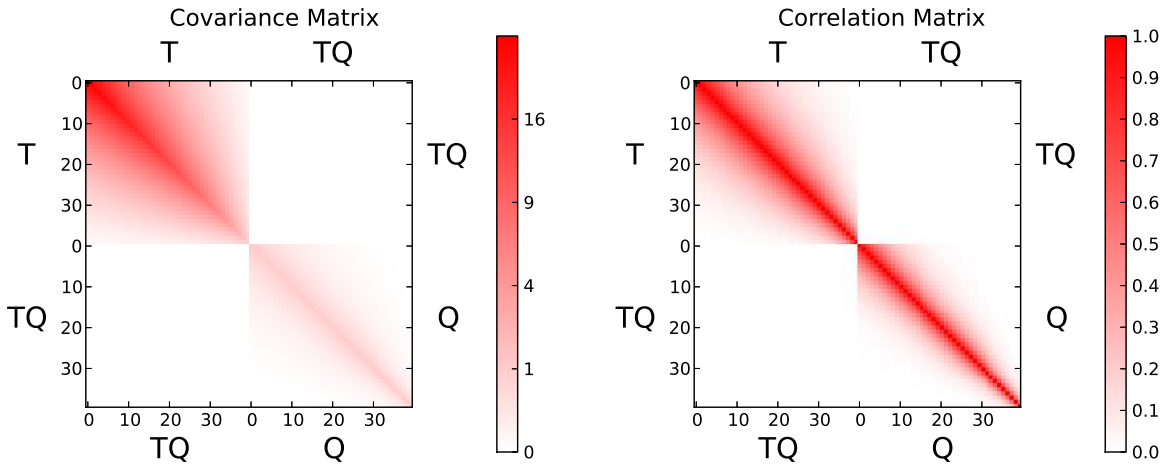

Figure 3.2 Synthetic prior covariance matrix (left) and correlation matrix (right) for temperature (T) and water vapor (Q) using equation 3.19. Level numbering starts from the surface at level 0, to the TOA at level 39.

example 40 level covariance matrix is shown in Figure 3.2. In this case, the temperature variance is a linear ramp from 25 to 1 K^2, and the water vapor variance is constant, equal to 1, for the logarithm of the water vapor mass mixing ratio. The vertical scale length L is 6 km for temperature and 3 km for water vapor. The leveling starts at 0 at the surface, so the apparent sharpening at higher level numbers is due to the more widely spaced levels at high altitudes.

In the second method, a radiosonde climatology is used to directly compute the covariance from an ensemble of measurements. Data from the ARM Climate Research Facilities (ACRF) is used for this purpose (Ackerman and Stokes, 2003). The ARCF sites feature twice daily radiosonde launches. Three sites are selected to span a wide range in atmosphere conditions: North Slope Alaska (NSA) at Barrow, Alaska; the Southern Great Plains (SGP) site at Lamont, Oklahoma; and the Tropical West Pacific (TWP-C3) site at Darwin, Northern Territory, Australia. Yearly and seasonal climatologies are constructed for each site; the seasonal climatologies include all profiles within the typical 3 month seasons [December–February (DJF), March–May (MAM), June–August (JJA), and September–November (SON)] plus 15 additional days before and after the 3 month window. Initially, bad radiosonde profiles are removed from the dataset by various

automatic checks: extremely high or low temperatures, large data gaps, or profile truncation below the tropopause. In addition, some manual outlier removal was performed to remove bad humidity profiles that showed unphysical variations. These data quality filters removed at most a few percent of the radiosonde profiles. A humidity correction (Cady-Pereira et al., 2008) is then applied to the each quality checked profile.

Standard atmosphere data is used for all other inputs required by the forward model that are not measured by the radiosondes. These additional data are primarily concentrations of infrared active trace gases (CH_4, O_3, N_2O, CO). In addition, the stratospheric data from the radiosonde is discarded. Altitudes above the tropopause are not consistently sampled since the maximum altitude reached by the radiosonde balloon is often in the lower stratosphere. The humidity measurements are not reliable in the very cold and dry stratosphere conditions. The stratosphere profile in the prior is taken from the corresponding standard atmosphere profile. Each profile within a particular composite uses the closest matching standard atmosphere. For example, all seasonal Darwin composite profiles are combined with the standard tropical profile. The SGP winter (summer) profile is combined with the standard midlatitude winter (summer) profile, and the spring and autumn SGP profiles are combined with an average of the two standard midlatitude profiles. The NSA seasonal profiles are combined with the standard subarctic profiles in an analogous manner. The transition between troposphere radiosonde data and stratosphere standard atmosphere data occurs at the tropopause, which occurs at level 19 in the subarctic winter profile (9 km altitude) and level 32 in the tropical profile (17 km altitude). The data on either side of the transition level is smoothed to prevent sharp discontinuities in the profiles. A small amplitude random fluctuation (1 K RMS for temperature, 30% RMS for log water vapor mixing ratio) is added to each stratospheric level, before computing the covariance. The covariance within the stratosphere is therefore diagonal with added sampling noise.

For clear sky priors, the profiles are also filtered to remove cloudy profiles. Cloudy profiles are indicated by layers with saturated relative humidity levels in the high resolution (20 m) gridded data before interpolation to the coarse level grid. Profiles with relative humidity over water or ice (for T $< -10^{\circ}$ C) greater than 100% for two samples were classified as cloudy. Two samples

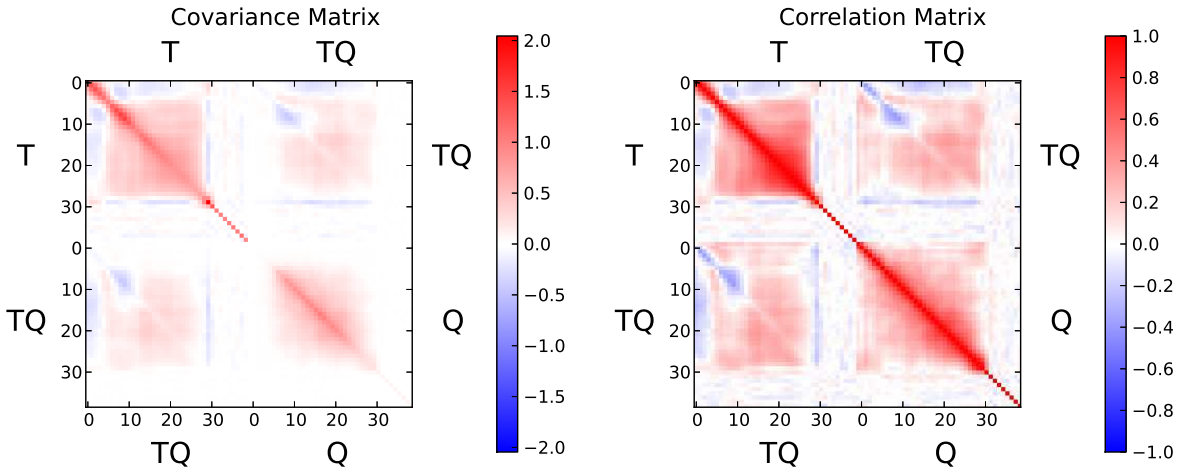

Figure 3.3 Computed covariance (left) and correlation (right) matrices, for the prior covariance computed at Darwin for DJF. Level numbering follows the convention in 3.2, so the upper left is the surface temperature point, and the lower right is the TOA water vapor profile point. Figure from Merrelli and Turner (2011).

implies a roughly 40 m layer for the high vertical resolution gridded data. For the Arctic data, these thresholds caused a large number of profiles to be classified as cloudy. To get a statistically significant sample for the seasonal composites, the count threshold was increased to five (from two), and points in the lowest 200 m altitude were ignored. The physical justification for these ad hoc threshold changes is that a relatively thicker saturated layer is needed to constitute a cloud layer with enough optical thickness to affect the infrared emission in arctic conditions where the water vapor content is much lower. The low altitude saturated points are likely occurring in blowing snow or diamond dust conditions which would not be detected as a cloud layer.

Figure 3.3 shows the computed covariance and correlation matrices for the clear sky Darwin DJF prior. The stratospheric levels stand out because the high altitude portion of the covariance matrix becomes approximately diagonal.

3.3.3 Forward Model and Jacobian

For Jacobian calculations, the LBLRTM computes analytic derivatives for surface temperature, surface emissivity, temperature and molecular concentration profiles. Any clear sky calculation in this work uses the LBLRTM analytic calculation. For LBLDIS, a simple first order finite difference is used to compute the Jacobian. Specifically, for the i^{th} state variable, the corresponding column of $\mathbf{K}$ is computed as:

$$\mathbf{K}_i(\mathbf{x}) = \frac{F(\mathbf{x} + \delta x_i \mathbf{e}_i) - F(\mathbf{x})}{\delta x_i} \tag{3.20}$$

where $\mathbf{e}_i$ is the unit vector for state variable i, meaning a value of 1 in the i^{th} element and 0 otherwise. The size of the increment δx_i is made as small as possible while still producing a large enough change in the simulated radiance so that the difference is larger than any numerical error in the calculation (e.g., floating point roundoff). For temperatures and cloud heights, the increment is an additive 0.1 K and 20 m, respectively. For other variables, including water vapor, cloud parameters (particle effective radius, optical depth, or particle PSD parameters), these are multiplicative increments in the range of 1%–5%.

3.3.4 Sensor Description, Including Measurement Covariance

The simulated sensors in this study resemble the planned infrared component of the CLimate Absolute Radiance and Refractivity Observatory (CLARREO). One of the primary objectives of CLARREO is to measure the spectral radiance of Earth's outgoing infrared emission with high absolute measurement accuracy. The planned infrared instrument is a Fourier Transform Spectrometer (FTS) with 0.5 cm^{-1} spectral resolution. The spectral coverage from 200–2000 cm^{-1} would be covered by one FIR-optimized and one MIR-optimized detector. The essential specifications of the simulated sensors roughly match this design. The spectral Noise Equivalent Delta Radiance (NEDR) follows from specifications of the potential pyroelectric FIR detector and photoelectric MIR detector that would be used in the CLARREO instrument. (Mlynczak, 2010; Merrelli and Turner, 2011). The two detector FTS design is also similar to the Atmospheric Emitted Radiance Interferometer (AERI, Knuteson et al. (2004b)) with the shortwave detector in the AERI

Table 3.1 Key characteristics of the simulated instrument.

Sensor band	Number of channels	wavenumber range [cm^{-1}]	wavelength range [μm]	minimum NEDT at 250 K
FIR	1006	200–685	50.0–14.6	0.18 K (at 600 cm^{-1})
MIR	2904	650–2050	15.4–4.88	0.17 K (at 760 cm^{-1})

replaced with an FIR detector. The MIR noise assumed in this study is similar to the longwave AERI detector noise. The FIR noise level may be significantly larger than the MIR noise. In order to compare the impact, a second noise curve will also be used in some calculations to see the impact of noise on the information content metrics. The low and high noise levels are different by a multiplicative factor of 3 in standard deviation (9 in variance). Figure 3.4 shows the assumed sensor noise as NEDR curves. The curves marked as dashed lines are the "high noise" curves. For the CLARREO instrument, the total NEDR curve will likely be the high noise curve for the FIR and the low noise curve for the MIR. Later comparisons will be mainly be in this configuration, but additional comparisons will be made between sensors at identical noise levels.

The wavenumber sampling and optical path difference is identical to the AERI (0.482 cm^{-1} and OPD = 1.037 cm), although there are some additional complications to consider when comparing the spectral radiance computed by the different forward models (see Sections 3.3.4.1 and 3.3.4.2). These spectral characteristics are summarized in Table 3.1. Since no apodization is used, the measurement noise covariance is assumed to be diagonal. This assumption is generally quite reasonable for spectral measurements from an FTS (Antonelli et al., 2004; Turner and Löhnert, 2012).

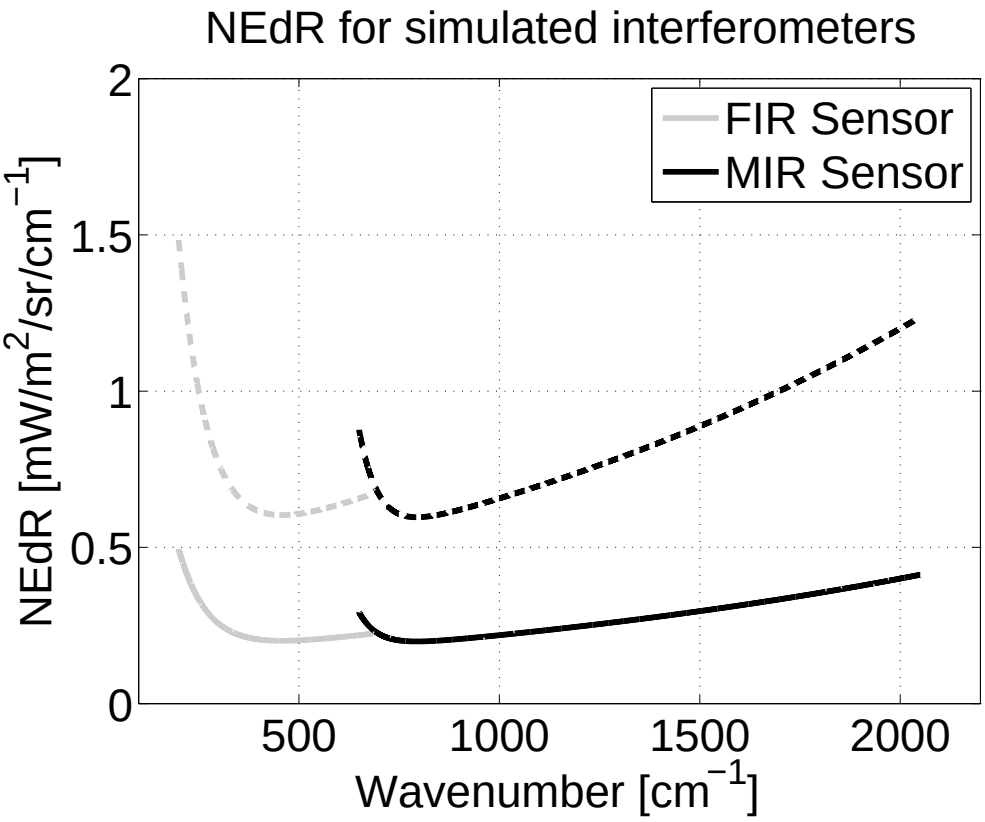

Figure 3.4 NEDR curves for the simulated spectrometer. The dashed lines denote the "high noise" simulated detectors, and the solid curves denote the "low noise" simulated detectors. Figure from Merrelli and Turner (2011).

3.3.4.1 Spectral Sampling in LBLRTM

For all LBLRTM radiance simulations, the ILS shape is assumed to be the unapodized sinc function for the idealized interferometer. The optical path and sampling is taken from the AERI, specifically OPD = 1.037 cm, and sampling $\Delta\nu$ = 0.48215 cm^{-1} (Knuteson et al., 2004b).

3.3.4.2 Spectral Sampling in LBLDIS

As described in 3.2.2, the LBLDIS averages quantities within the defined spectral increment width, which results in a rectangular function ILS. For simplicity, the spectral grid is set to 0.5 cm^{-1}, which is slightly coarser than the LBLRTM grid (0.48215 cm^{-1}). Although changing the spectral sampling in an interferometer should change the noise level, this is a very small discrepancy (3%), so the same NEDR curve is applied for simulated measurements from either model.

In the overall framework, since the same forward model is generating synthetic measurements as is used in the retrieval (a "perfect model" assumption), and the spectrometers are modeled as idealized interferometers, the difference between the LBLDIS spectrum and the LBLRTM spectrum should only be a difference in convolution kernel: rectangle function for LBLDIS, sinc function for LBLRTM. Convolution is a linear operation, so it should not affect the information content calculations within this framework. To verify this assumption, two extra calculations were run with LBLDIS at a much higher spectral resolution (0.05 cm^{-1}, a factor of 10 higher in resolution), with a thin (τ = 0.2) and thick (τ = 10.0) cloud at z = 14 km in a standard tropical atmosphere profile. The resulting radiances and radiance Jacobians are convolved with the same sinc function ILS as LBLRTM, and these calculations are compared to the default LBLDIS configuration with 0.5 cm^{-1} rectangular function ILS. Each set of Jacobians is used to compute DFS, following the calculations in equation 3.7. The final computed DFS for both simulated sensors (FIR-only, MIR-only, FIR + MIR combined) are very close, with a maximum discrepancy between the different DFS metrics of 1%.

Chapter 4

Information Content in Clear Sky Profiles[1]

The clear sky vertical profile of temperature and water vapor is the primary retrieved geophysical data from the hyperspectral infrared sounder. In this chapter, the information content, vertical resolution, and robustness to simulated model error are studied for both FIR and MIR hyperspectral observations. Since both spectra are simulated within the same framework, quantitative comparisons can be made between the various metrics. The results show where retrievals from FIR spectra can complement or improve upon the same retrieval from MIR spectra.

4.1 Methods

4.1.1 Modeled Sensors

The FIR and MIR spectrometers are described in Chapter 3, and the key specifications are listed in Table 3.1. The "base" instruments use the low noise (solid curve) NEDR curves shown in Figure 3.4. In addition to the base instruments, two additional instrument pairs are considered: high noise and high spectral resolution. The high noise pair have the same characteristics except have NEDR curves that are a factor of 3 higher (the dashed curves in Figure 3.4). The high spectral resolution pair has the same characteristics but uses a factor of 4 higher OPD (4.148 cm) and a factor of 4 reduction in the spectral sample increment (0.12 cm^{-1}). The same NEDR curve is used at this higher spectral resolution. This does imply an observation requiring a factor of 4 longer in dwell time, since the interferogram would need to be measured by the FTS detector over the longer OPD

[1]Portions of this chapter were published in Merrelli and Turner (2011) and are copyright of the American Meteorological Society.

with the same scan rate. These three sets of instruments will be labeled “base”, “NEDR $\times 3$”, and “$\Delta\nu/4$” in later figures.

4.1.2 State Vector

Since the focus of this analysis is the thermodynamic profile, the assumed surface properties are quite simple. The surface is assumed to be a greybody with constant spectral emissivity of ϵ = 0.95. The surface temperature is assumed to be equal to the temperature of the level at z = 0. The final state vector for the clear sky analysis consists of per-level profiles of temperature and the logarithm of water vapor mass mixing ratio with the level grid as described in Section 3.3.1.

4.1.3 Clear Sky Priors

After constructing all the composite radiosonde prior covariances (section 3.3.2), a subset of four was selected in order to simplify the analysis. The four composites, ordered by total water vapor amount, are NSA DJF, SGP DJF, SGP JJA, and Darwin DJF. These priors roughly span the same climatological range as the standard atmosphere profiles (subarctic, midlatitude, tropical), but have the additional information about covariance among levels in the temperature and water vapor profiles. Figure 4.1 shows the prior mean temperature and water vapor mass mixing ratio profiles.

4.1.4 Ad Hoc Channel Selections

Due to the simplistic surface assumption (constant emissivity), the spectral information from the surface is entirely redundant over all surface sensitive channels. In order to reduce the computational complexity of the retrievals, most of the window region (770–1228 cm^{-1}) is removed from the MIR spectrum. The removal of the window region also removes the primary O_3 absorption feature at 1040 cm^{-1}. Since no detailed a priori data for O_3 is used in this study, there is no need to consider these channels.

One important consideration for thermodynamic profile retrieval is characterization of other radiometric signatures in the radiance spectrum that can interfere with the signatures needed for

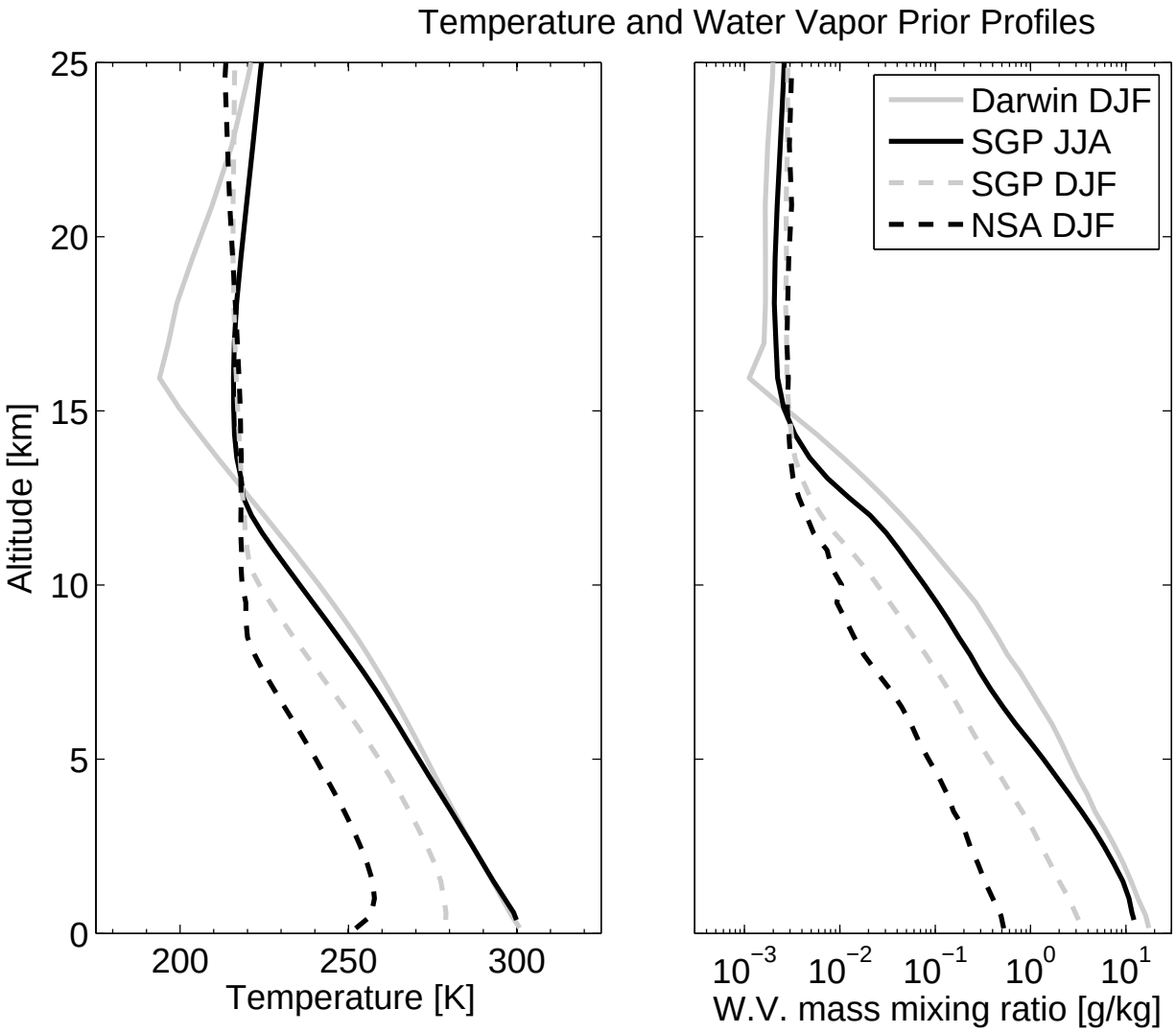

Figure 4.1 Mean temperature and water vapor mass mixing ratio profiles for the four selected clear sky composite priors. Figure from Merrelli and Turner (2011).

profile retrieval. For the clear sky problem, the important signatures are trace gases, surface temperature and surface emissivity. These signatures can easily introduce bias error in the thermodynamic profile if not handled appropriately. One way to limit their impact is to simply censor them from the spectrum used in the retrieval. For thermodynamic profiling, the temperature and water vapor is spread over a large fraction of the IR spectrum and covers a large number of the available channels. There is a large degree of redundant information in these channels, so discarding a small fraction of the available channels should cause minimal degradation in the information content.

In order to remove the effect of trace gas interference, a simple ad hoc channel selection is used. The three primary infrared active molecules after water vapor and CO_2 are O_3, CH_4 and N_2O. For each of these molecules, the profile is scaled by 5% relative to the standard atmosphere concentration, and the radiance is computed using LBLRTM in the standard configuration. Each difference spectrum (5% perturbation versus unperturbed profile) is compared to the NEDR curve, and any channel that shows a change that is larger than 0.5 times the NEDR at that channel is added to the "ignore list". This calculation is repeated for each ACRF climatology, and the total ignore list consists of the union of all lists. The primary trace gas absorption features identified with these calculations are N_2O at 590 cm^{-1}, O_3 at 700 cm^{-1}, and CH_4 and N_2O at 1300 cm^{-1}. Figure 4.2 shows the identified channels overplotted on a brightness temperature spectrum computed from the Darwin DJF mean profile. Note the large gap from 770–1228 cm^{-1} where the window and O_3 sensitive channels are ignored.

4.2 Results

4.2.1 Simulated Forward Model Errors

Since the state vector only includes the temperature and water vapor profiles, the surface temperature, surface emissivity and trace gas profiles are not retrieved. These variables are set to the a priori values (bottom level temperature, $\epsilon = 0.95$, and the standard atmosphere trace gas profiles). If the upwelling radiance measurement is simulated with a different surface property or trace gas profile, while the forward model continues to use the a priori value, the difference essentially creates a forward model error. Random differences were applied to several variables to

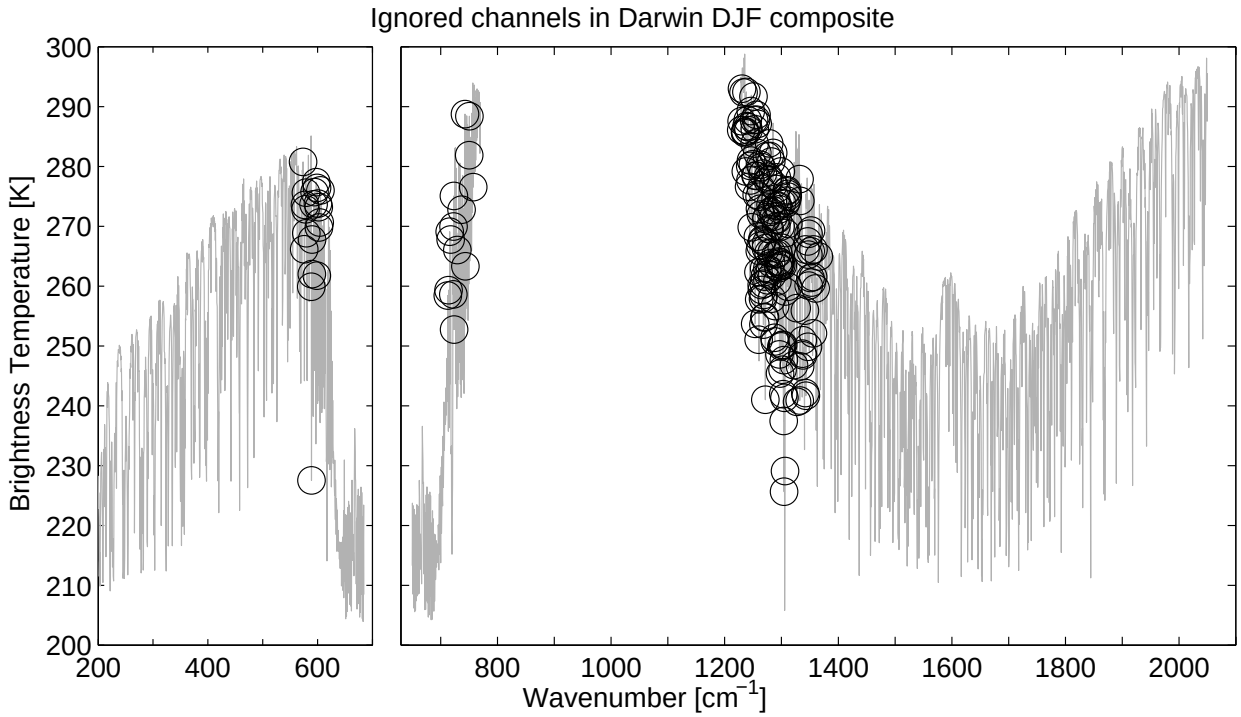

Figure 4.2 Simulated brightness temperature spectrum with ignored channels marked with circles. See text for description. Figure from Merrelli and Turner (2011).

create such forward model errors. For the surface property, a perturbation to the temperature or gray body emissivity would produce nearly the same effect on the simulated radiance, so only a surface temperature perturbation is used. The temperature perturbation is an additive error drawn from a Gaussian probability distribution with a standard deviation of 0.25 K. For trace gas profiles, the total column is perturbed by a multiplicative factor, which is a drawn from a Gaussian with a standard deviation of 2.5%. These perturbations are applied to the $\mathrm{CH_4}$ and $\mathrm{N_2O}$ profiles, as these showed the most impact on the final retrieval error. The 2.5% variations are roughly consistent with observed seasonal variations in total column amounts observed with remote sensing techniques based on differential solar absorption (Dils et al., 2006).

A number of retrieval experiments are run to compute sample estimates of the retrieval error. Each experiment involves 30 retrievals over an ensemble of independent sensor noise realizations, using the prior mean state and the measurement vector corresponding to the prior mean state. The baseline experiment has no forward model perturbation, so the resulting retrieval error is only caused by the random sensor noise. This represents an error "floor" for the retrieved state. Three additional experiments are run, for each of three simulated forward model errors: surface temperature, CH_4 profile, and N_2O profile perturbations. The retrieval error for each of these cases will be increased by some amount dependent on the sensitivity of the retrieval to that forward model error. The basic error statistic is the Root Mean Square (RMS) of the difference between the mean retrieved profile and the truth (prior mean) profile. The mean retrieved profile is the average over the 30 profiles with independent sensor noise realizations. Since the RMS is computed for the mean retrieved profile, the uncorrelated random error due to sensor noise is reduced through averaging by a factor of approximately $\sqrt{30}$. The error in the retrieved profile due to the forward model error may be correlated, which would imply less reduction in the RMS through averaging. Any retrieval that did not converge was discarded. This only occurred for surface temperature perturbations to profiles with low water vapor amounts. Finally, each set of experiments was run with the full channel set (all FIR channels, and MIR with the window channels removed, 770–1228 cm^{-1}), and again with the ad hoc ignore list of channels sensitive to trace gas perturbations (section 4.1.4).

The RMS error results are shown for all experiments in Figure 4.3. The baseline temperature error is in the range 0.05–0.12 K for all cases, while the baseline water vapor error is in the range 0.05 g kg^{-1} for the tropical profile and 0.003 g kg^{-1} for the arctic profile. The baseline errors are approximately equal when comparing the MIR and FIR retrievals.

The different sensitivities to the forward model errors qualitatively follow expectations, given the location of the trace gas absorption bands and the highly variable total column water vapor in the different mean profiles. First, focusing on the retrievals with full channels (the solid lines), the surface temperature error is shown to increase sharply as the water vapor amount decreases. For the FIR measurement in the tropical atmosphere, the transmission to the surface is zero everywhere, so the retrieval is unaffected by the temperature error. A similar but not as direct pattern is seen in the MIR results, since there is relatively more transmission to the surface in all climatologies. The MIR results do show a drop in temperature error from the SGP JJA profile to SGP DJF, which acts opposite to the change in water vapor amount between the two profiles. The reason for this discrepancy is not clear, though it is likely related to the different covariance structures in the two priors. The perturbation to the CH_4 profile only affects the MIR, since the associated absorption band is centered in the MIR at 1300 cm^{-1}. The effect is weakest in the arctic mean profile, since there is relatively less interference due to the low water vapor amounts and thus the overlapping water vapor absorption lines are much weaker. The effect is strongest in the SGP DJF profile, which may indicate that retrieval sensitivity to CH_4 perturbations is maximum for particular water vapor column amounts. Similar to the CH_4 perturbation, the N_2O perturbation shows the least impact in the low water vapor arctic profile, and the maximum for the SGP DJF profile. It shows essentially no impact on the water vapor error for the arctic profile. N_2O has strong absorption features in both the MIR and FIR, so the perturbation does cause errors in both bands, but the error increase is much smaller in the FIR.

Applying the ad hoc channel selection to remove interfering trace gases shows significant improvement for the CH_4 and N_2O results, but no impact on the surface temperature, as expected. For CH_4, there is still residual temperature error in the SGP DJF profile, and residual water vapor error in all but the arctic profile (which was not effected by CH_4 at all). Even though CH_4 absorption

lines only exist in the water vapor absorption bands, they can introduce temperature error due to the fact that the water vapor and temperature Jacobians tend to correlate these state variables. For example, consider a real atmosphere profile that contains excess optical depth at wavenumbers in the 1300–1400 cm^{-1} range due to increased CH_4 concentration above the assumed prior value. If the temperature decreases with height through the altitude spanned by the relevant weighting functions, then at these wavenumbers the simulated spectrum would show a higher radiance than the observed spectrum. The residual between the simulated and the measured radiance spectrum could be compensated in the state estimate update by either an increase in water vapor concentration or a decrease in temperature. The actual state estimate will quite likely contain a combination of both compensating adjustments. It is very unlikely that the adjustment would only be made in the water vapor profile, so the result is an incorrect adjustment to the temperature profile, and an increased temperature error. The error that remains while using the ad hoc channel selection is likely caused by residual weak CH_4 lines that were not included in selection because the radiance change did not pass the NEDR-based threshold. Similarly to CH_4, applying the ad hoc selection improved the error for the N_2O as well, with some residual error left over in the MIR water vapor retrieval.

4.2.2 Applied OE Channel Selection

By using the ordered channel selection list from the OE selection algorithm, the DFS can be plotted as a function of the number of selected channels. Dividing by the total DFS contained within the entire channel set shows the fractional DFS and allows for easier comparison between calculations that have different total DFS. Figure 4.4 shows this result for one composite prior and all modeled sensors. Only one composite is plotted for clarity. Other composite priors produce very similar curves. These fractional DFS curves have many common features. For the first s channel selections, the channels are largely independent, so each new channel nearly 1 additional DFS. This only continues for a few channels, roughly $s < 8$. As the number of channels increases, the fractional DFS grows much slower as additional channels are correlated to channels that have already been selected. The OE selection does concentrate information within these s channels, but there is always some fraction in the remaining $m - s$ channels. For example in Figure 4.4 the

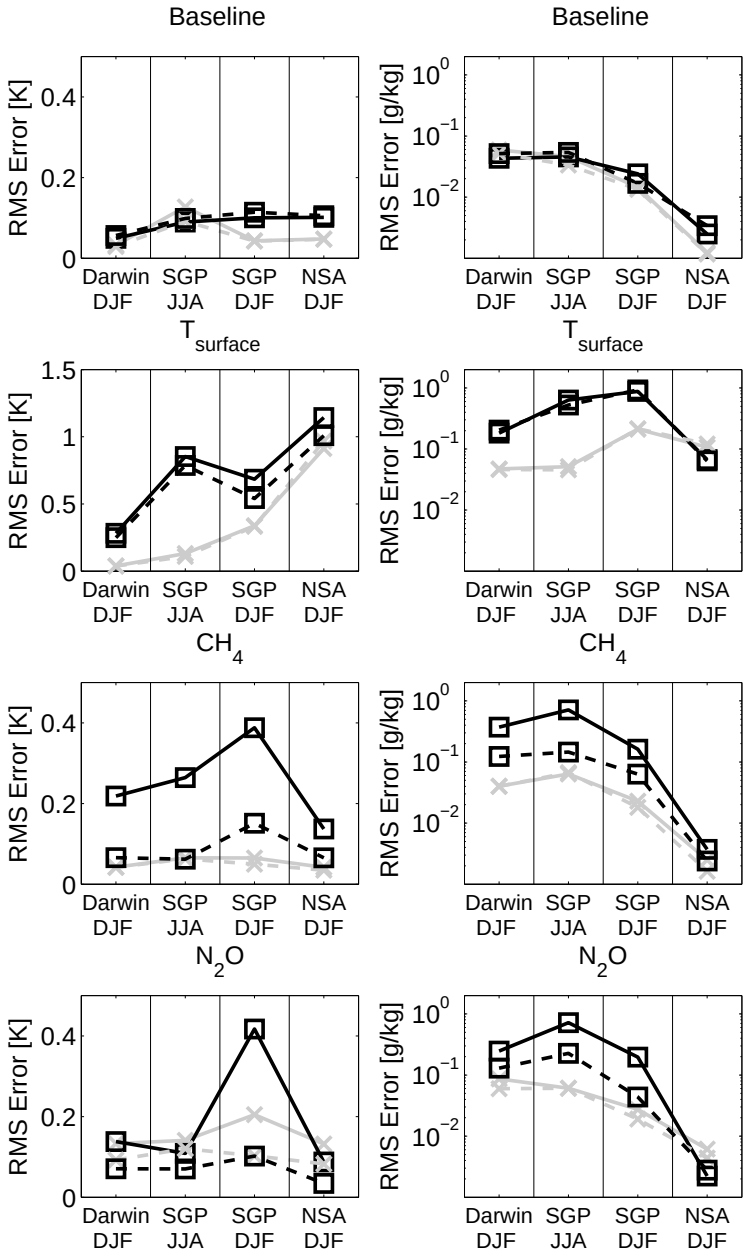

Figure 4.3 (left) RMS Error for temperature (right) and water vapor mass mixing ratio for various simulated forward model errors. The results are shown for MIR (square markers, dark gray lines) and FIR (X markers, light gray lines). Solid lines use maximum channels, and dashed lines ignore channels with significant interference from trace gases (see text for description), Note the y-axis is identical for all temperature plots except for the larger range for the surface temperature perturbation. The y-axis display range for all water vapor errors is identical and logarithmic. Figure from Merrelli and Turner (2011).

selections are stopped at 250 channels for the base and NEDR $\times 3$ spectrometers and 500 channels for the $\Delta\nu/4$ spectrometers. These cutoffs were chosen so that $> 80\%$ of the total DFS are retained in all selected subsets. From the logarithmic scaling in the plot, it is clear that reducing the DFS loss from 20% to 10% would require a much larger number of retained channels (over 1000 for the MIR $\Delta\nu/4$ spectrometer). The subset of OE selected channels is overplotted on a simulated radiance spectra in Figure 4.5. Note that the ad hoc channel selection described in Section 4.1.4 was applied before the OE channel selection, which results in no selections of the weak water vapor lines in the range 800–1200 cm^{-1}. It is also important to note that the ad hoc selection did not remove channels with wavenumbers higher than 1650 cm^{-1}; channels at these higher wavenumbers are ignored by the OE selection because of higher sensor noise for these channels.

4.2.3 Constrained OE Channel Selections

An additional variation of OE channel selection is used to investigate and visualize relative information content of each spectral region. The channel selection is first run on one spectral region using the standard approach described in Section 3.1.3 to select a subset of 250 channels. The total set of channels is then merged into one combined set, and the selection continues, with the constraint that the initial 250 are already allocated from the initial selection run with only those channels from one spectral band. This process is similar to the sequential selection in Rabier et al. (2002).

For example, consider an initial selection with 250 channels from the FIR spectrometer. The channel list is now expanded to include the 2904 MIR channels as well as the (1006–250) unselected FIR channels. The channel selection loop is now restarted using this merged set of unselected channels, with the posterior covariance including the initial selection of 250 FIR-only channels. Channel selections 251 and beyond could be drawn from FIR or MIR channels, depending on their information content as computed by the OE algorithm.

The constrained selection is applied in two ways. First, 250 channels are selected from the FIR-only channel list, followed by 250 channels from the merged (unselected FIR and MIR) channel list. This yields a total of 500 selected channels. The second way applies the constraint in the

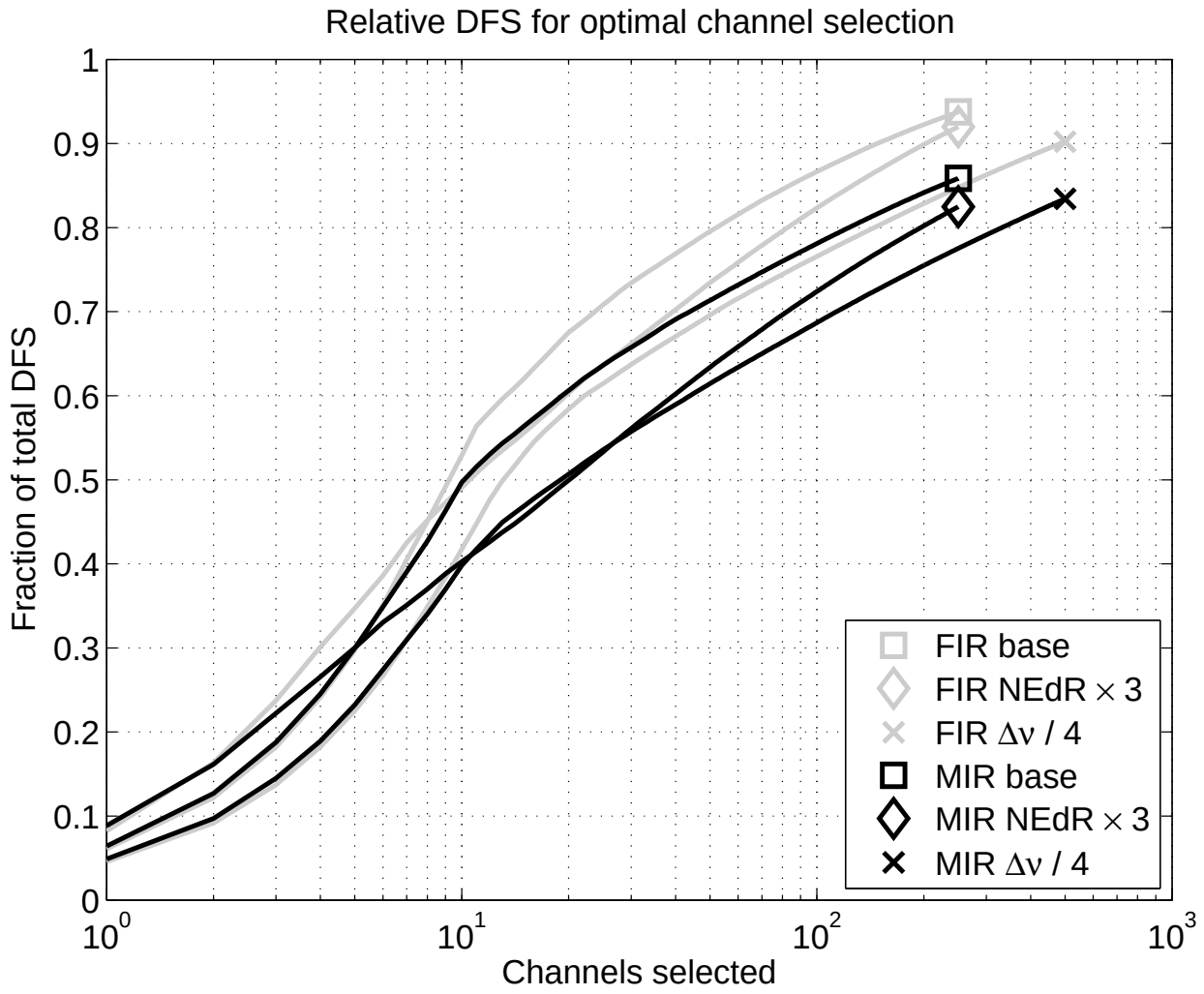

Figure 4.4 Cumulative DFS fraction as a function of number of channels selected by the OE algorithm. The selections were stopped at a total of 250 channels for the baseline and high noise sensor specifications, and 500 channels for the high spectral resolution specification. Figure from Merrelli and Turner (2011).

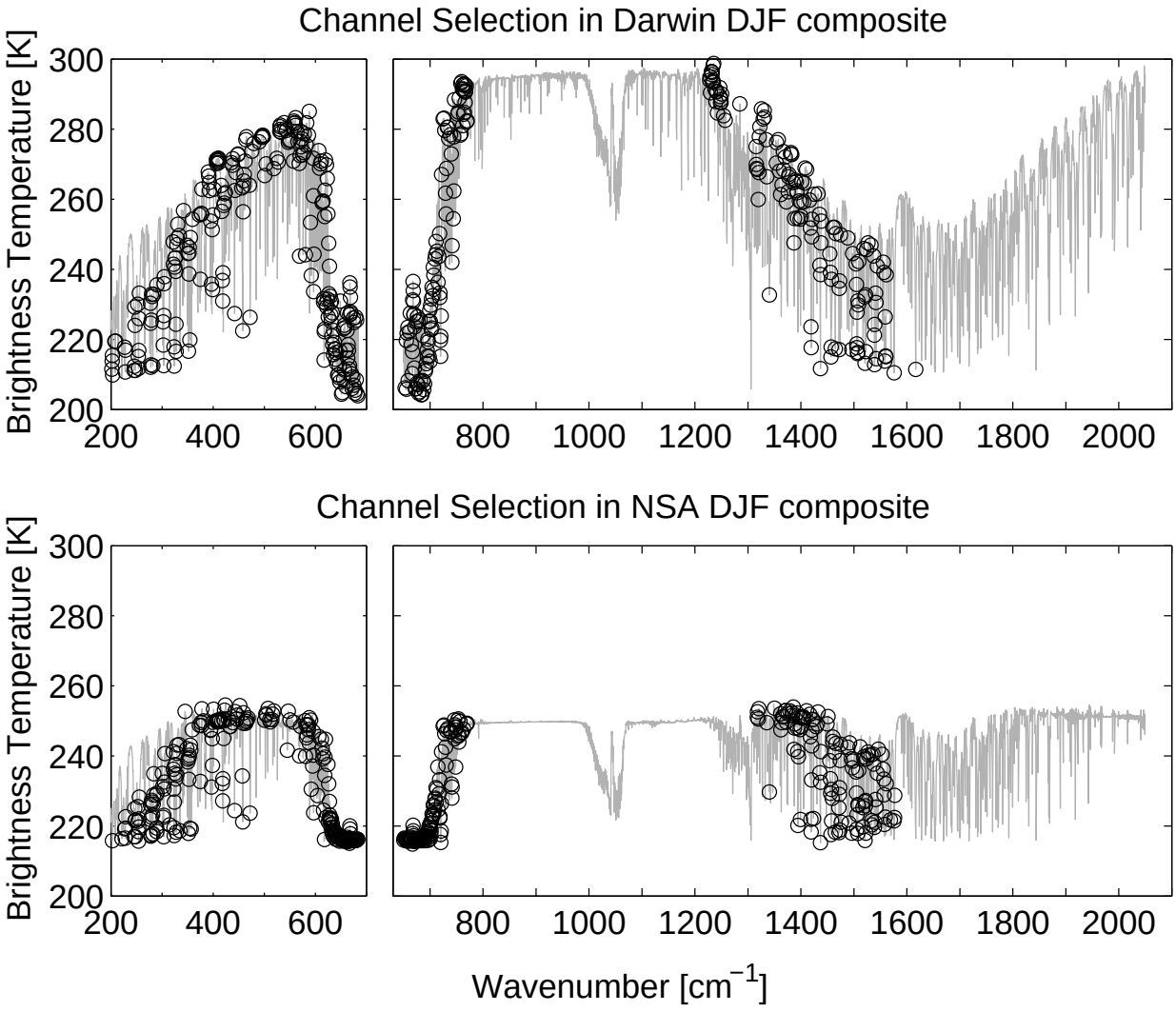

Figure 4.5 Simulated radiance spectra for the Darwin DJF and NSA DJF prior profiles, with the 250 selected channels marked with circles. Figure from Merrelli and Turner (2011).

reverse order. Specifically, the first 250 channels are selected from the MIR-only channel list, and the next 250 are selected from the merged (unselected MIR and FIR) channel list. These two constrained selections are both applied to two sensor configurations. The first uses the base FIR and MIR sensors (both using the low noise NEDR curves), and the second uses the $\times 3$ NEDR (high noise) FIR combined with the base (low noise) MIR. Figures 4.6 and 4.7 show the results of these constrained selections, presented as a scatter plot of selection rank versus wavenumber. The selection rank as the y axis shows the order of channel selection. In each figure, the top plot represents the first constrained selection (FIR-only for the first 250 channel selections), so all points for ranks < 250 on the y-axis are drawn from the FIR wavenumbers. The reverse is seen in the bottom plot, where all selections in the first 250 selections are drawn from the MIR wavenumbers. Noting the wavenumbers of the selections for channels 251–500 reveals where the OE algorithm finds independent information in the spectrum.

First, consider the constrained selection using the base MIR and FIR sensors (Figure 4.6). In the top plot, where the FIR channels are selected first, all of the next 100 channels are selected from the MIR. However, the MIR channels sensitive to water vapor (> 1200 cm^{-1}) are almost entire ignored in the final $\sim$100 selections, making up only 5 channel selections. The FIR water vapor absorption band is well sampled in the last 100 selections. The MIR does show a large amount of added information in temperature, from the high wavenumber side of the CO_2 absorption band. The FIR half of the CO_2 band has interference from the water vapor absorption band, so it is likely that adding MIR channels in this region improves the ability of the OE algorithm to separate water vapor and temperature changes in the lower troposphere levels. The constrained selection in the reverse order (MIR-only for the first 250 selections) is shown in the bottom plot, and reveals the same principles. After the MIR-only selection, almost all the channel selections are drawn from the FIR.

Repeating the experiment with the high noise FIR and low noise MIR sensors shows a similar pattern, but with less emphasis on the FIR channels due to the higher noise (Figure 4.7). After the MIR-only selection, the majority of selections in the merged channel list are taken from the FIR water vapor absorption lines. Compared to the previous results with both low noise sensors,

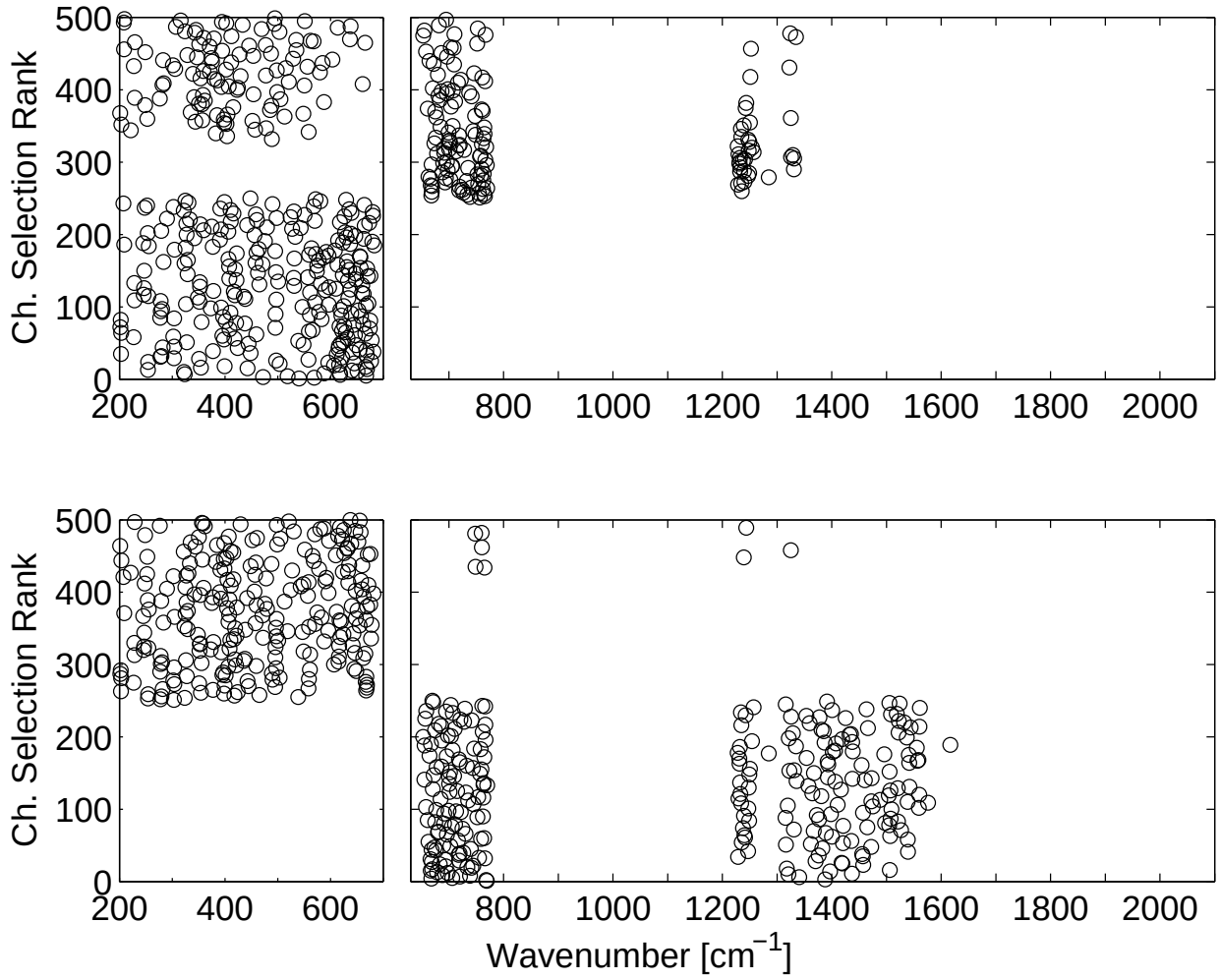

Figure 4.6 Constrained selection using the base (low noise) FIR and MIR sensors. 250 channels selected from FIR only, followed by 250 channels selected from merged FIR and MIR channel list (top); 250 channels from MIR only, followed by 250 channels selected from merged FIR and MIR channel list (bottom). Figure from Merrelli and Turner (2011).

relatively more MIR channels are selected. For example, 12 channels are selected from the MIR water vapor absorption, up from 3 selected when both low noise sensors are used. Preferentially less channels on the FIR side of the CO_2 absorption band are selected, as the noise level is now much higher for these channels compared to the MIR CO_2 channels.

4.2.4 Information Content

Continuing with the same climatological priors, the DFS statistic is calculated at the prior mean profile for all three sensor variants: baseline, high spectral resolution ($\Delta\nu$ / 4), and high noise ($\times 3$ NEDR). The DFS is split into information in the temperature profile and information in the water vapor profile by computing the trace along only the section of the $\mathbf{A}$ matrix that contains the corresponding profile. Recalling from section 4.1.3 that the stratospheric levels in the prior are synthetic, the DFS are computed only from the tropospheric levels. Figure 4.8 shows the results for all conditions.

Comparing FIR and MIR temperature DFS results, the FIR shows a small information content advantage (0.2–1 DFS increase) in nearly all situations. For the Darwin DJF prior, there is a slight (0.2 DFS) advantage for the MIR. In this case the high water vapor column amount causes the atmosphere to become fully opaque at the lowest levels in the FIR, which cases this slight drop relative to the MIR DFS. The water vapor DFS is sharply higher in the FIR in the Darwin DJF prior, in contrast to the temperature DFS.

Comparing the FIR and MIR for the water vapor DFS results, the FIR shows a slightly larger advantage (0.5–2.0 DFS) in all situations. Interestingly, the DFS advantage for the FIR is highest in the high water vapor profile, Darwin DJF. Although the high water vapor amount means the FIR loses all sensitivity to the lowest levels which should cause a DFS drop, within the tropical prior the lower troposphere levels are fairly constrained by the prior. Tropical atmospheres tend to be nearly saturated at the lowest levels. Saturation implies a narrower range of water vapor mixing ratio, and less potential for the measurement to help constrain the state estimate. Therefore, even though the lowest level water vapor cannot be constrained by the FIR measurement, it is already constrained by the prior so there is no significant DFS drop in this situation. In contrast, the upper

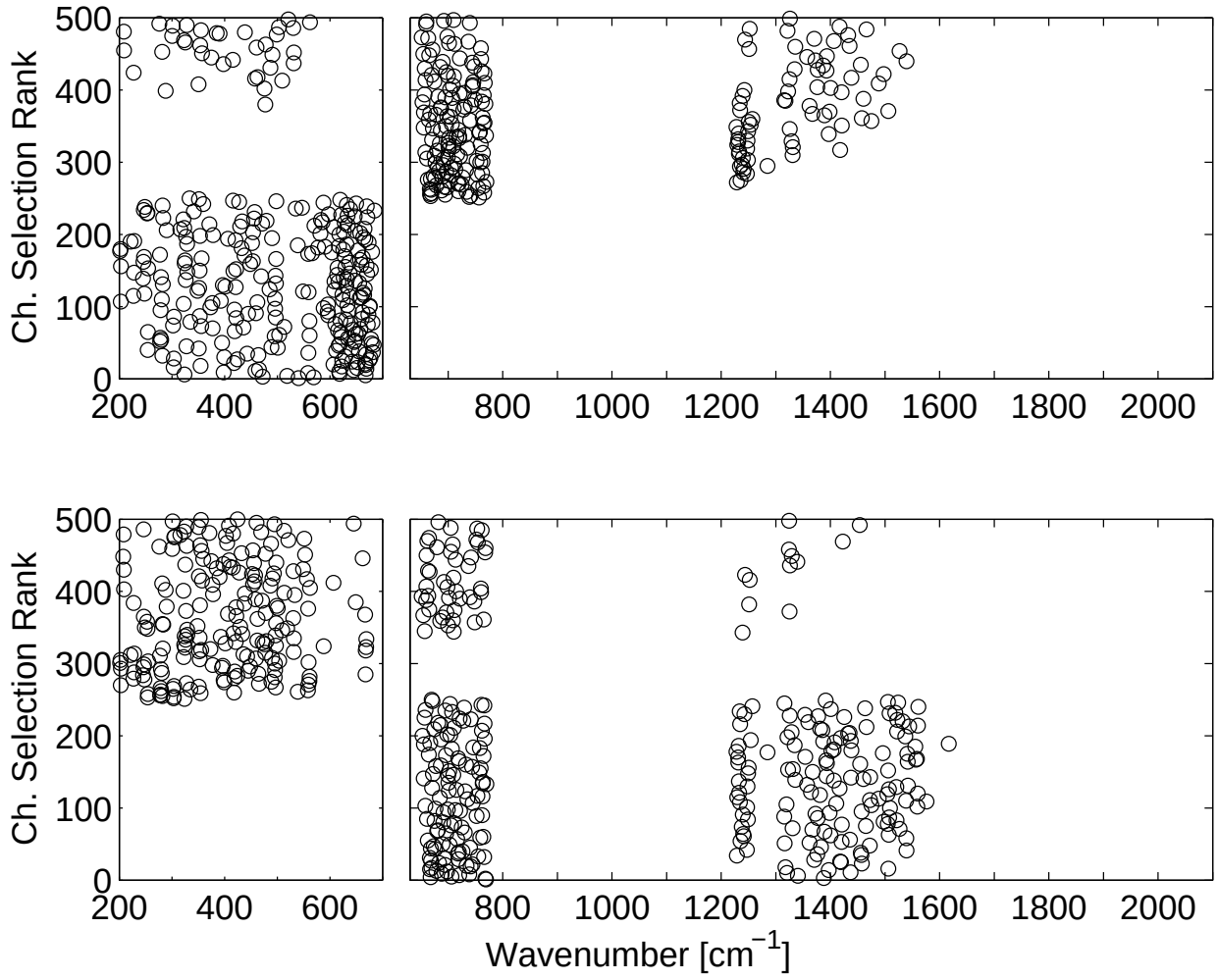

Figure 4.7 Same as Figure 4.6, but using high noise FIR and low noise MIR spectrometers. Figure from Merrelli and Turner (2011).

troposphere levels in the tropical profile have the largest information content advantage for the FIR due to the cold emission temperatures (section 2.3.2).

Profiles of the DFS per level are shown in Figure 4.9. These profiles display the DFS per km, which is simply the DFS profile (the diagonal of the $\mathbf{A}$ matrix) divided by the layer thickness at that altitude. The profiles at all four climatologies are shown, computed for the FIR-only, MIR-only, and combined (FIR + MIR) spectral measurements. In the three cases shown in Figure 4.9 the DFS profiles are computed with different a priori state covariance matrices to emphasize the affect of the prior on the resulting DFS. The top image shows the results using the prior covariance computed from the radiosonde climatology. The tropopause is easily visible as the altitude where the water vapor DFS sharply drops, since there is little information where the water vapor concentration is extremely small (roughly 16, 13, 11, 9 km, from left to right). There is a similar feature at these altitudes in the temperature DFS, but this is related to a reduction in the prior variance above the tropopause. The stratospheric data was simulated using 1 K RMS variation, which is significantly smaller than the RMS temperature variation for all radiosonde climatologies except for the tropical (Darwin) case. The tropical temperature RMS is very low (1–2 K at all levels). The DFS profiles also show some small spatial scale fluctuation due to the propagation of sampling noise from the covariance calculation. This prior includes any temperature–water vapor correlation found in the radiosonde data as well. By computing a synthetic covariance using the exponentially decaying correlation (equation 3.19), much of the sampling noise can be removed. This tuned synthetic a priori covariance has the same variance (diagonal) as the computed covariance with the off diagonal elements recomputed from the exponential equation. All cross-correlations between temperature and water vapor are set to zero. The resulting DFS profiles are shown in the middle plot in Figure 4.9. The tropical temperature DFS stands out as being much lower than the other profiles. This is due to the small RMS (1–2 K) mentioned earlier. Since the prior has such a small volume in state space, there is not much added information for temperature. The water vapor profile, however, has a high amount of information since there is a large amount of variance in the prior above the boundary layer. Finally, to focus on the difference between the prior mean profiles, a single synthetic covariance was applied to all profiles. The synthetic covariance matches Figure 3.2.

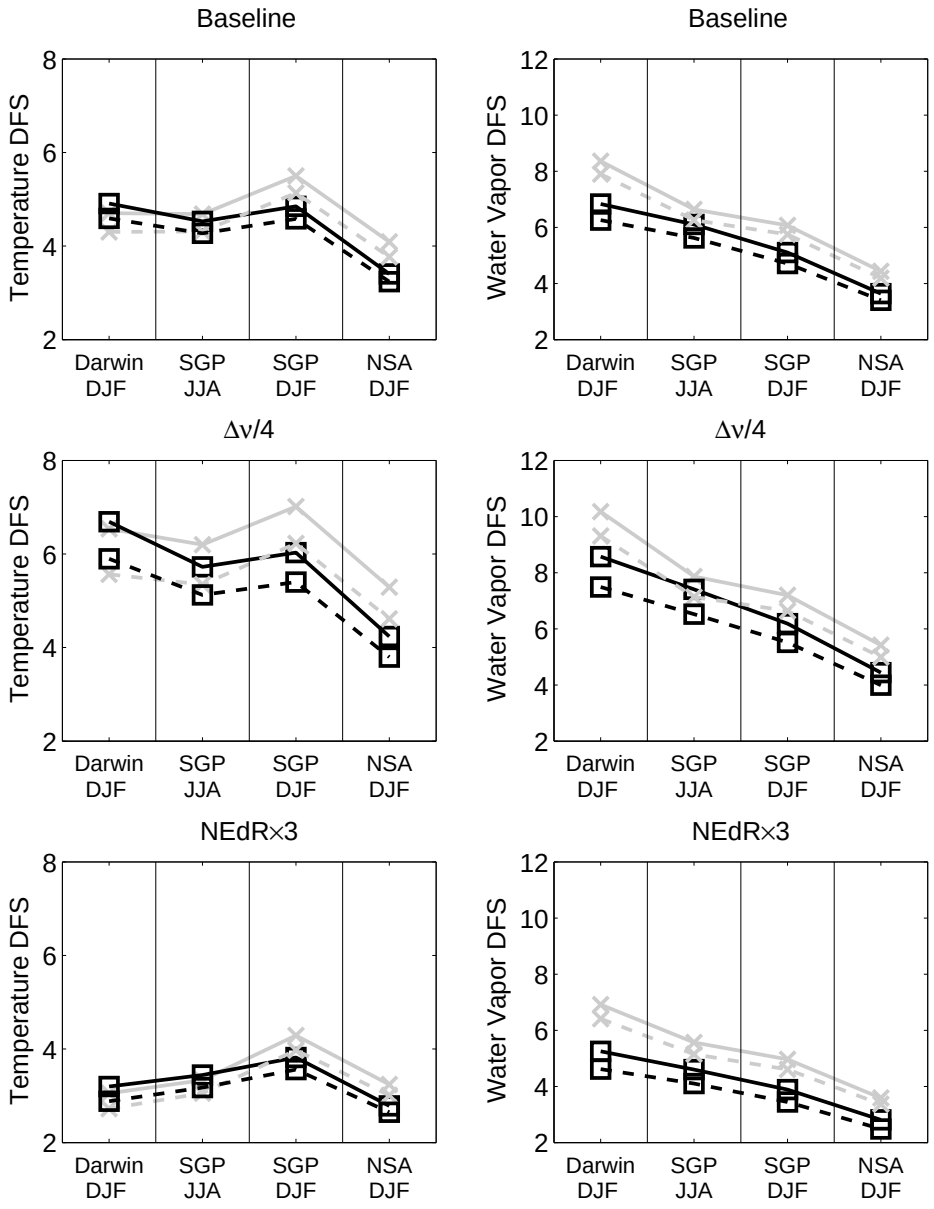

Figure 4.8 DFS results for the temperature profile (left column) and water vapor profile (right column). All three simulated spectrometer types are represented: baseline (top row), high spectral resolution $\Delta\nu/4$ (middle row), and high noise (NEDR $\times 3$) (bottom row). The plot markers match those used earlier in Figure 4.3, namely: light gray and X for FIR results; dark gray and square for MIR results. The solid line and dashed lines now represent different aspects. The solid line represents results using the ad hoc channel selection (MIR window, and trace gas sensitive channels are removed), and the dashed line represents the OE channel selection using 250 channels (500 channels for high spectral resolution). Figure from Merrelli and Turner (2011).

The differences are now dependent only on the atmosphere profile, which affects the calculation through the $\mathbf{K}$ matrix computed at the prior mean profile. The DFS profiles are shown in the bottom part of Figure 4.9. Since there is no sampling noise, the profiles are much smoother. The tropical temperature DFS profile no longer stands out since all profiles have the same total variance in the prior.

A number of important qualitative features can be seen by comparing the results using different spectra. The lack of sensitivity at the lowest levels in the FIR can be seen in the high water vapor profiles (Darwin DJF and SGP JJA). However, there are enough microwindows between water vapor absorption lines that even in the tropical profile there is information down to ≈ 2 km. The FIR generally shows increased water vapor DFS at all altitudes. The temperature DFS is generally equivalent between the FIR and MIR. The combined measurement shows the strengths of both FIR and MIR spectra.

The effect of sensor noise and spectral resolution on the DFS profile can be examined by plotting the difference between profiles using different instrument specifications. For these comparisons, the single synthetic covariance is used, in order to eliminate the sampling noise and focus on the differences in the atmospheric profile rather than the shape of the prior covariance. Figures 4.10 and 4.11 show the difference between the baseline and high noise (NEDR $\times 3$) and the high spectral resolution ($\Delta\nu/4$) and the baseline. Qualitatively, each plot shows similar overall features. There is increased DFS primarily in the tropospheric levels with a small amount extending into stratospheric levels. The sensor noise reduction (from high noise to low noise) appears to have a smaller effect in the stratosphere water vapor DFS relative to the spectral resolution increase. This difference is mainly due to the fact that DFS for stratospheric water vapor is close to zero for the baseline and NEDR $\times 3$ sensor specifications. The increased DFS for stratospheric water vapor in the high spectral resolution case is an interesting result. The implication is that a stratospheric water vapor profile may be retrievable with a spectral resolution increase to 0.125 cm^{-1}.

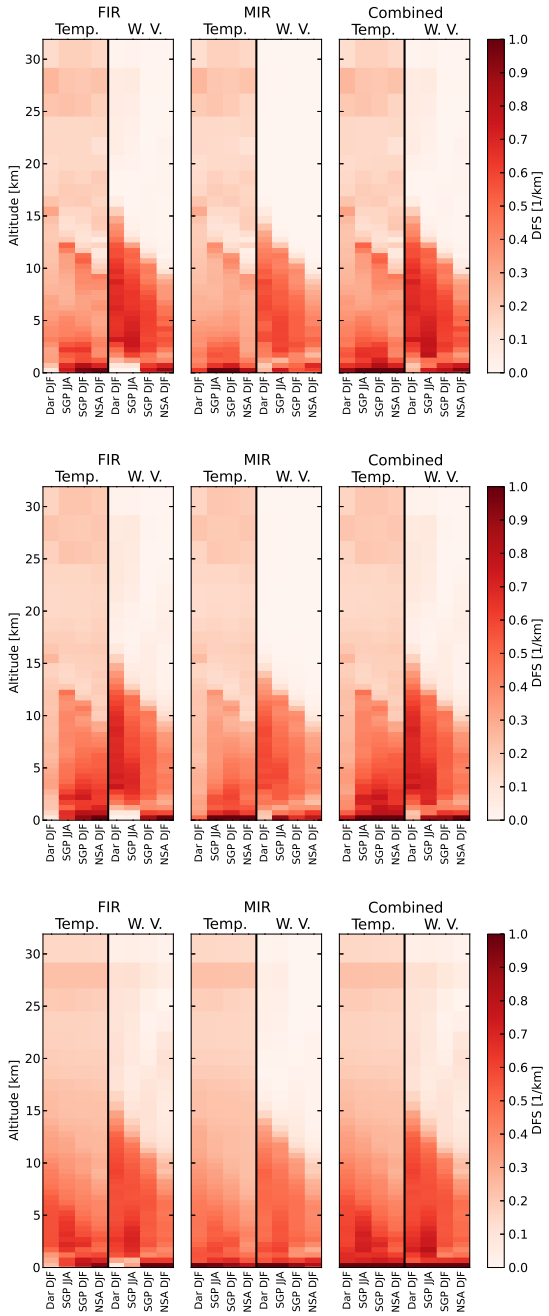

Figure 4.9 DFS profiles for temperature and water vapor, using a priori covariance computed from radiosonde climatologies (top), a priori variance computed from radiosonde climatologies, but with correlation set by equation 3.19 (middle), and a single synthetic covariance (Figure 3.2) applied to all climatologies (bottom). Each plot shows results from FIR spectra (left), MIR spectra (middle) and FIR + MIR spectra (right), with each image showing temperature DFS profiles on the left, and water vapor profiles on the right.

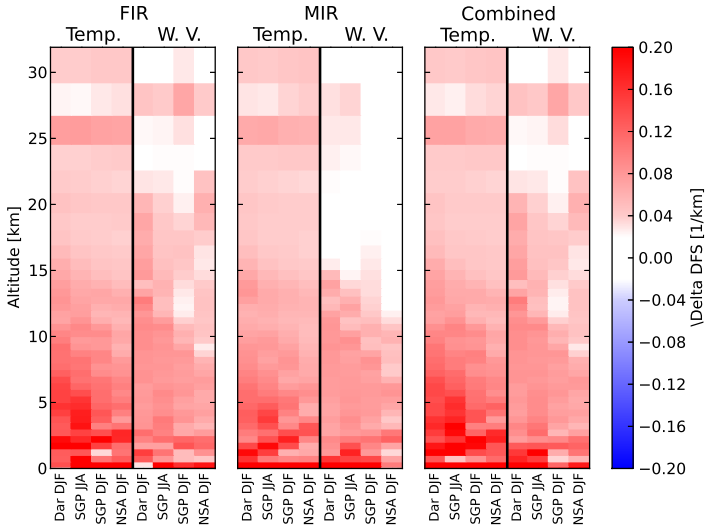

Figure 4.10 "Δ DFS" profiles: DFS profiles from the high noise (NEDR $\times 3$) instrument subtracted from the DFS profiles from the baseline instrument. Plot layout identical to Figure 4.9

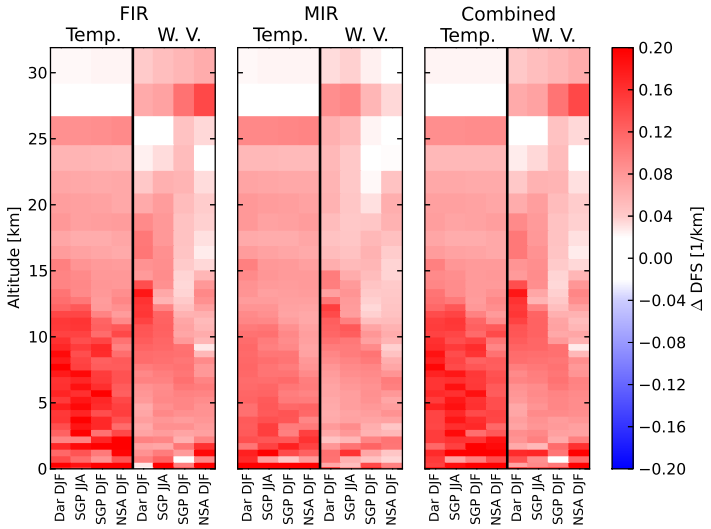

Figure 4.11 "Δ DFS" profiles from the baseline instrument subtracted from the DFS profiles from the high spectral resolution ($\Delta\nu/4$) instrument. Plot layout identical to Figure 4.9

4.2.5 Vertical Resolution

The averaging kernel FWHM calculation presented earlier (Figure 3.1) can be used to compute the vertical profile of the averaging kernel width, by computing the FWHM for each row in $\mathbf{A}$. Figure 4.12 shows these profiles for the baseline instrument, using the same set of a priori covariances as used in Figure 4.9. Several patterns emerge, that are similar to patterns seen in the DFS profiles. Regions of low DFS (stratospheric water vapor in particular) show very poor vertical resolution (off scale, meaning > 10 km), which reflects the fact that little can be added to the profile beyond the a priori in this region. Removing the measured T–Q cross correlations and replacing the T–T and Q–Q correlation with the exponential equation (middle plot) shows improved vertical resolution for all but the tropical temperature profile. In general, removing the temperature–water vapor correlations should increase resolution, since the retrieval can independently fit each profile. For the tropical profile, it appears that the correlation between temperature and water vapor was adding information and resolution to the temperature profile through the cross-correlation to water vapor. The significant impact after removing this cross-correlation is due to the fact that the tropical profile has a relatively small temperature and large water vapor variance. Applying the same covariance to all four climatologies (bottom plot) improves the resolution in the tropical profile to match the pattern suggested by the other three profiles.

In Figure 4.13, the summary resolution statistics are plotted in a layout that matches the DFS summary shown in Figure 4.8. Each single point in this case is the average of the AK resolution profile within the troposphere for that prior climatology and sensor specification. The measured a priori covariances are used in these calculations. The relatively poor resolution for the Darwin temperature is related to the previously discussed combination of low total variance and a high degree of correlation between levels in the radiosonde climatology. The FIR shows a small advantage in vertical resolution in all virtually all cases. The OE channel selection algorithm again shows good performance, with only a very small ($< 10\%$) degradation in vertical resolution in all cases.

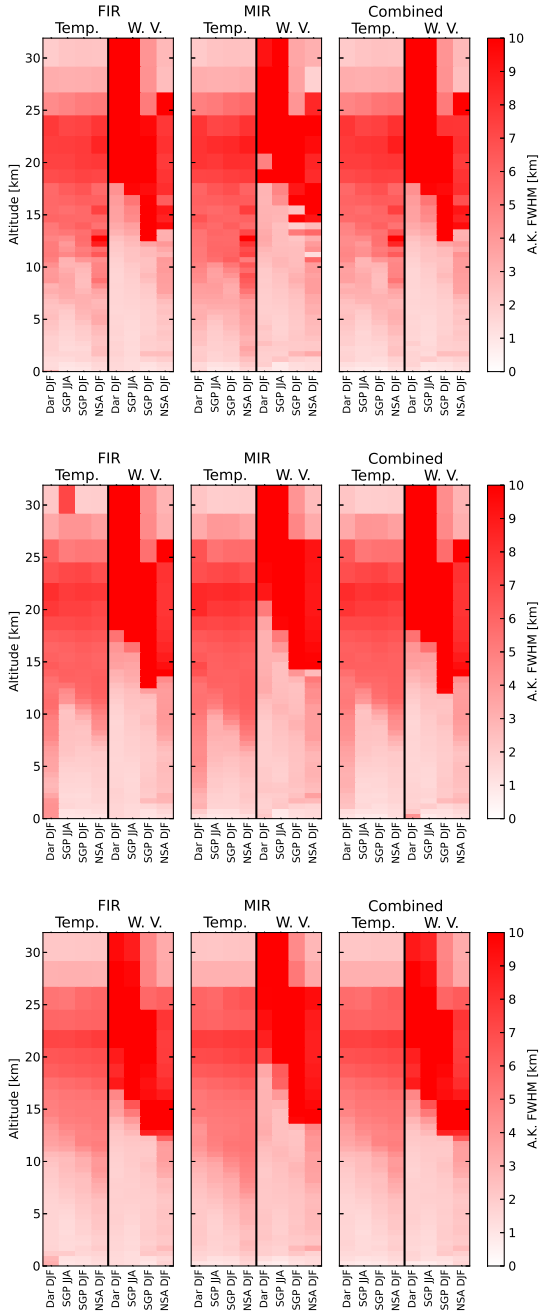

Figure 4.12 Vertical profiles of averaging kernel FWHM. Layout and annotations match Figure 4.9 except the colorbar range is now FWHM in km.

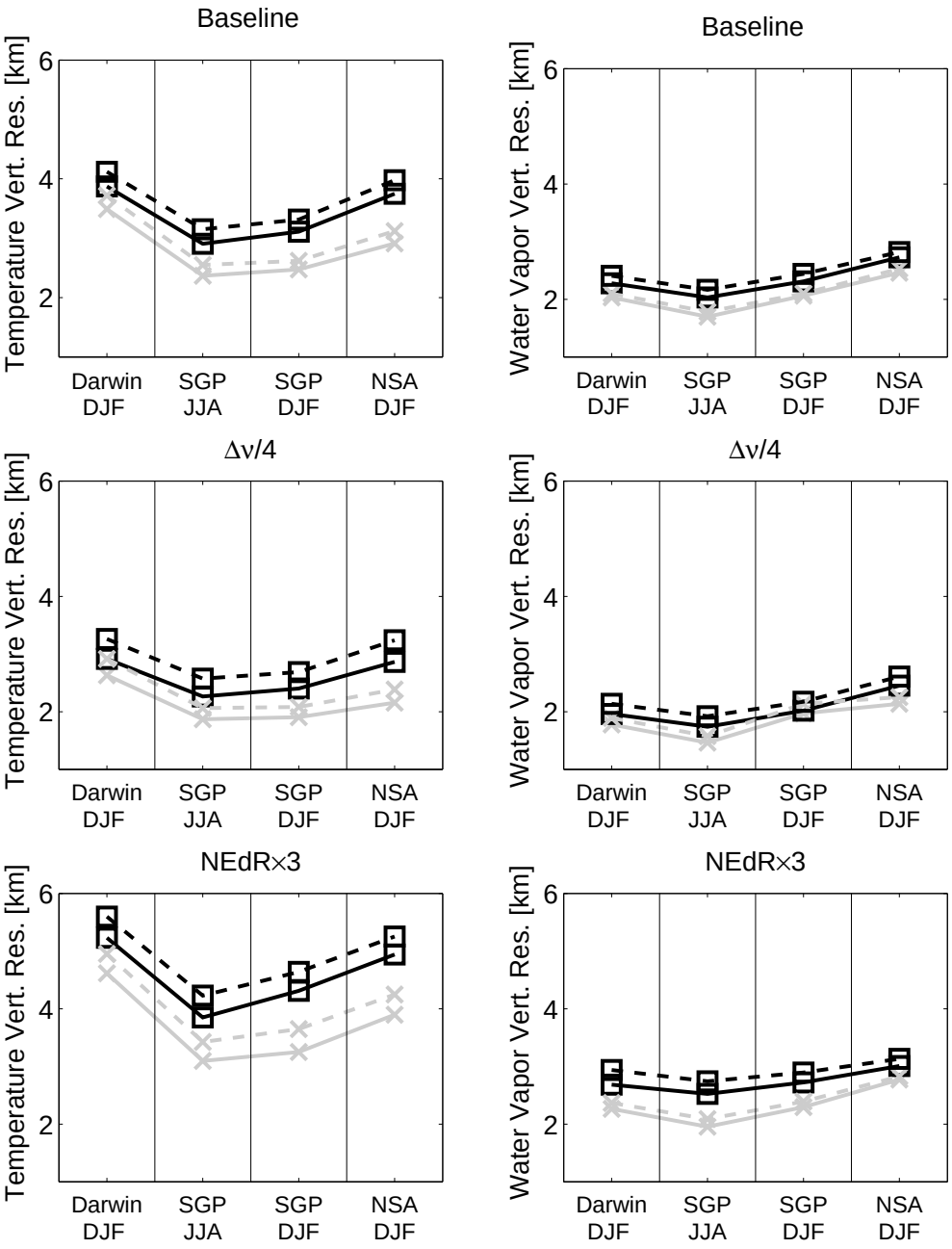

Figure 4.13 Summary of average troposphere vertical resolution. Label markers match those in Figure 4.8. Figure from Merrelli and Turner (2011).

4.3 Summary

A series of modeling and retrieval experiments enabled a detailed comparison of the information content for clear sky thermodynamic profile retrievals. The comparison reveals that the FIR offers some key advantages over the MIR for these retrievals. First, fewer trace gas absorption lines in the FIR water vapor absorption band result in a retrieval that is more robust for model errors in trace gas characteristics. For high water vapor absorption amounts, the atmosphere becomes opaque near the surface, making the FIR profile retrieval immune to any surface mischaracterization. While the opaque levels near the surface do imply a loss of information since these levels will be undetectable, there are still microwindows with partial transmission down to about 2 km in the highest water vapor atmosphere (Darwin). Even with an opaque total atmosphere column, the partial transmission allows a thermodynamic profile to be retrieved from a large fraction of the troposphere.

From an information content perspective, the FIR consistently shows an advantage in the water vapor profile and an equivalent temperature profile in clear skies when compared to the MIR. For high water vapor, the lowest levels would need to be retrieved by an MIR measurement. The increased information using the higher spectral resolution measurement also suggests a potential to retrieve water vapor in the stratosphere using the FIR, although this aspect should be further investigated using more realistic measurements of the stratospheric water vapor profile mean and variance (i.e., with more accurately defined a priori information). Using the averaging kernel FWHM to estimate vertical resolution, the FIR shows a small but consistent resolution advantage.

It is important to note that the comparisons above used particular spectral shapes for the sensor NEDR for each measurement (Figure 3.4), which have roughly equivalent minimum noise in radiance units. The more realistic combination for the CLARREO instrument is thought to be the higher noise FIR with the baseline (low noise) MIR (Merrelli and Turner, 2011). Repeating a similar "Δ DFS" calculation as used above in Figure 4.10 shows the impact of this different noise level. Starting on the left half of Figure 4.14, a comparison is shown between the DFS of an FIR-only and combined FIR-MIR measurement versus an MIR-only measurement. The leftmost

image, (a), shows the DFS of the FIR-only measurement minus the DFS of the MIR-only measurement, so the change in DFS can be considered the difference in information between the FIR and MIR measurements. The middle left image, (b), is now the DFS in the combined (FIR and MIR) measurement, minus the MIR only measurement. This can be viewed as the added information that would be obtained by extending an MIR spectrum into the FIR region. For these two images, the baseline specification (low noise) is used for both the FIR and MIR. The middle right and far right images, (c) and (d), show the same quantities, but now using the high noise FIR measurement. Considering images (a) and (b), there is added information in water vapor throughout the entire profile and within the troposphere for temperature. The combined measurement also shows significant additional information in the boundary layer where the FIR is blind. This increase is likely due to the improved characterization of levels just above the boundary layer, which can improve the MIR result by allowing it to rely less on correlations to estimate the boundary layer state. The result with the high noise FIR measurement shows that there is little advantage over the MIR; the FIR-only measurement is slightly worse in all cases for the temperature profile, and worse for the water vapor profile in the boundary layer. Above the boundary layer, the water vapor profile is roughly equivalent. In the combined measurement, the added information is marginal. Thus, answering the question of which spectral region produces the best sounding is difficult to answer without detailed knowledge of the actual sensor noise performance.

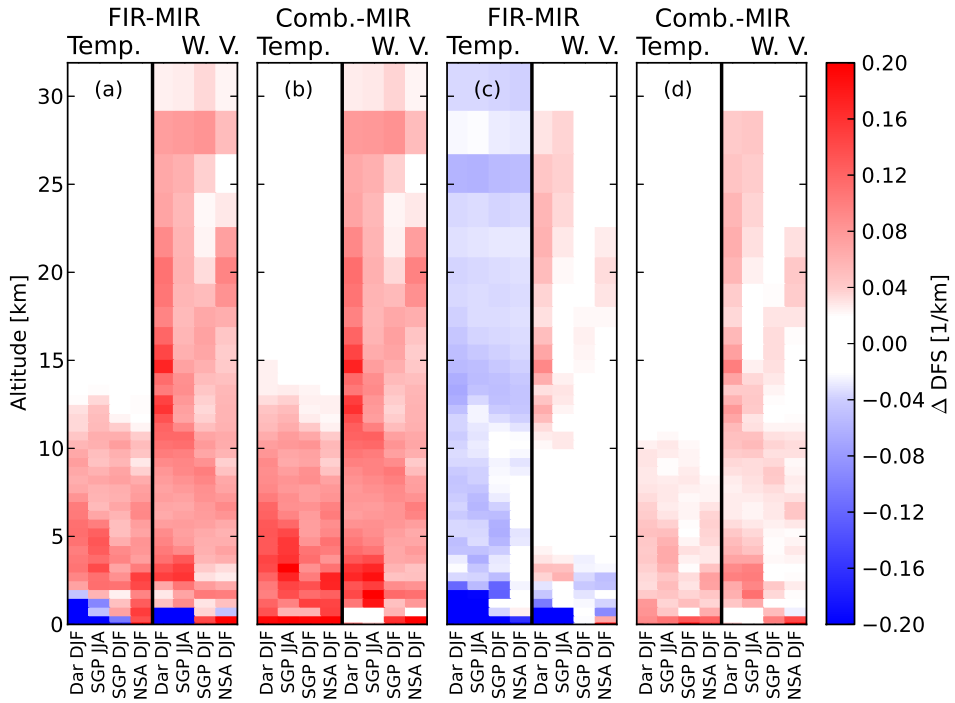

Figure 4.14 "Δ DFS" profiles, relating various DFS profiles back to the baseline MIR DFS profiles; from left to right: (a) baseline FIR DFS profiles minus baseline MIR DFS profiles; (b) baseline combined (FIR and MIR) DFS profiles minus baseline MIR DFS profiles; (c) baseline FIR DFS profiles minus baseline MIR DFS profiles; (d) baseline combined (FIR and MIR) DFS profiles minus baseline MIR DFS profiles. Plot layout for individual images matches Figure 4.9

Chapter 5

Information Content in Cloudy Sky Profiles

The framework discussed in the previous chapter is extended to include single layer ice clouds. The spectral refractive index of ice and the scattering size parameter change significantly from the MIR to FIR, resulting in key differences in the upwelling spectral radiance in cloudy atmospheres. The previously discussed Optimal Estimation (OE) metrics are used throughout as the primary method to quantify the changes in information content for thermodynamic profile and cloud property retrieval.

5.1 Methods

5.1.1 Modeling Framework

The previously defined sensor specifications are used to define the spectral range, resolution, and noise level. No comparison between the different specifications is made in this section, so only the final configuration is used for these simulations. Specifically, the FIR sensor uses the "high noise" NEDR and the MIR sensor uses the "low noise" baseline NEDR.

As discussed previously in Section 3.2.2, LBLDIS is used to simulate radiances in cloudy conditions. Although LBLDIS can be used to approximate vertically inhomogeneous clouds, by splitting a single cloud into layers with different particle distributions, this option is not used. All simulated clouds in this study will be single homogeneous layers.

The LBLDIS input parameter file allows for a cloud layer to be defined with 3 key properties: the particle effective radius, cloud optical depth, and a single altitude value to define the cloud

height. The particle effective radius is used to compute the single scattering properties for the cloud particles, by linearly interpolating between effective radius values in a pre-computed database.

The cloud particles are assumed to be evenly distributed throughout the layer containing the input altitude value. The layers used by LBLDIS are those defined in the initial LBLRTM run that computes the layer gaseous optical depths. To allow for precise control over the cloud altitude, the cloud definition is extended to include an option of defining the cloud top and bottom. The level grid is modified by inserting two levels equal to the desired cloud top and bottom, and then the single-value LBLDIS cloud altitude will be equal to the mean of the cloud boundary altitudes. If the cloud boundaries contain one or more levels in the pre-defined LBLRTM level grid, then the optical depth is divided among the two or more layers that are now contained within the cloud. The total cloud optical depth is linearly split among these layers according to the vertical altitude fraction.

5.1.2 Single Scattering Optical Properties

The ice particle scattering property database of Yang et al. (2005) is used for all simulations. This database contains the scattering phase function at 498 angles, the particle projected area, total volume, single scatter albedo, asymmetry parameter, and extinction efficiency. The asymmetry parameter is not directly used, since LBLDIS uses the computed phase function instead of a Henyey-Greenstein function approximation. These databases exist for several different ice crystal habits: solid column aggregates, bullet rosettes, hollow and solid single columns, plates, droxtals, and spheroids. Figure 5.1 shows the volume of each particle habit as a function of particle dimension scaled by the volume of a sphere with equal diameter. Note that the volume of droxtals, spheroids, and aggregates all follow a r^3 scaling, with droxtals closest to the spherical volume. The bullet rosettes and plates increase in volume slower than r^3, and the columns initially scale as r^3 but start to change in aspect ratio for $r > 100$ μm so the volume grows slower than r^3.

LBLDIS expects single scattering data for a bulk distribution of ice particles, meaning the single-size data must be integrated over an assumed Particle Size Distribution (PSD). In all cases the alternative gamma distribution form defined in Hansen and Travis (1974) is used as the particle

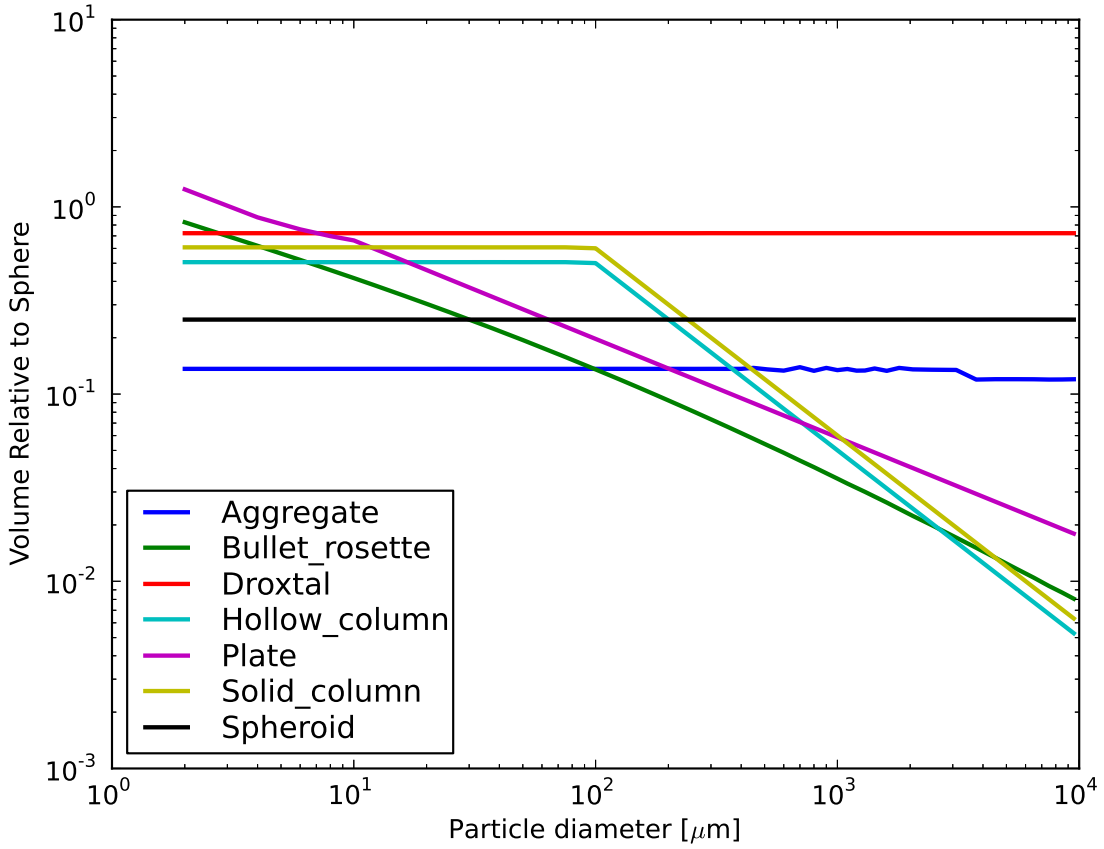

Figure 5.1 Volume as a function of particle dimension for various habits in the Yang et al. (2005) database, divided by the volume of a sphere with equal diameter.

PSD:

$$N(r) = Cr^{\frac{1-3v_{\text{eff}}}{v_{\text{eff}}}} e^{-\frac{r}{v_{\text{eff}} r_{\text{eff}}}} \tag{5.1}$$

where r_{eff} and v_{eff} are the effective radius and effective variance parameters, and C is a constant related to the total particle number density. The effective radius and variance are defined as:

$$r_{\text{eff}} = \frac{\int_{r_1}^{r_2} r\pi r^2 N(r)\, dr}{\int_{r_1}^{r_2} \pi r^2 N(r)\, dr} \tag{5.2}$$

$$v_{\text{eff}} = \frac{\int_{r_1}^{r_2} (r - r_{\text{eff}})^2 r^2 N(r)\, dr}{\int_{r_1}^{r_2} r_{\text{eff}}^2 \pi r^2 N(r)\, dr} \tag{5.3}$$

For spherical particles, the effective radius parameter r_{eff} in this equation does match the definition of effective radius commonly used for non-spherical particles (Baum et al., 2007), which is just ratio of the PSD-weighted volume integral to the PSD-weighted area integral times 3/4:

$$r_e = \frac{3}{4}\frac{\int_{r_1}^{r_2} V(r)N(r)\, dr}{\int_{r_1}^{r_2} A(r)N(r)\, dr} = \frac{3}{4}\frac{\int_{r_1}^{r_2} \frac{4}{3}\pi r^3 N(r)\, dr}{\int_{r_1}^{r_2} \pi r^2 N(r)\, dr} = \frac{\int_{r_1}^{r_2} r^3 N(r)\, dr}{\int_{r_1}^{r_2} r^2 N(r)\, dr} \tag{5.4}$$

For non-spherical particles, the r_{eff} parameter in equation 5.5 will not be equal to the effective radius r_e as defined in equation 5.4. Therefore, PSD equation will be rewritten for clarity by renaming the r_{eff} parameter as the "PSD size parameter", r_0, and the width parameter will use the symbol σ. In addition, the PSD can be expressed as a true PDF (meaning the integral over all r is equal to unity) multiplied by a constant specifying the total number density (Petty and Huang, 2011):

$$N(r) = N_0 n(r) = \frac{N_0}{(r_0\sigma)^{\frac{1-2\sigma}{\sigma}}\Gamma\left(\frac{1-2\sigma}{\sigma}\right)} r^{\frac{1-3\sigma}{\sigma}} e^{-\frac{r}{\sigma r_0}} \tag{5.5}$$

This alternate form has the advantage of decoupling the two parameters r_0 and σ such that changing r_0 "translates" the PSD and σ "stretches" the PSD. Figure 5.2 shows sample PSD curves for a variety of coefficient values, plotted in both linear and logarithmic scales.

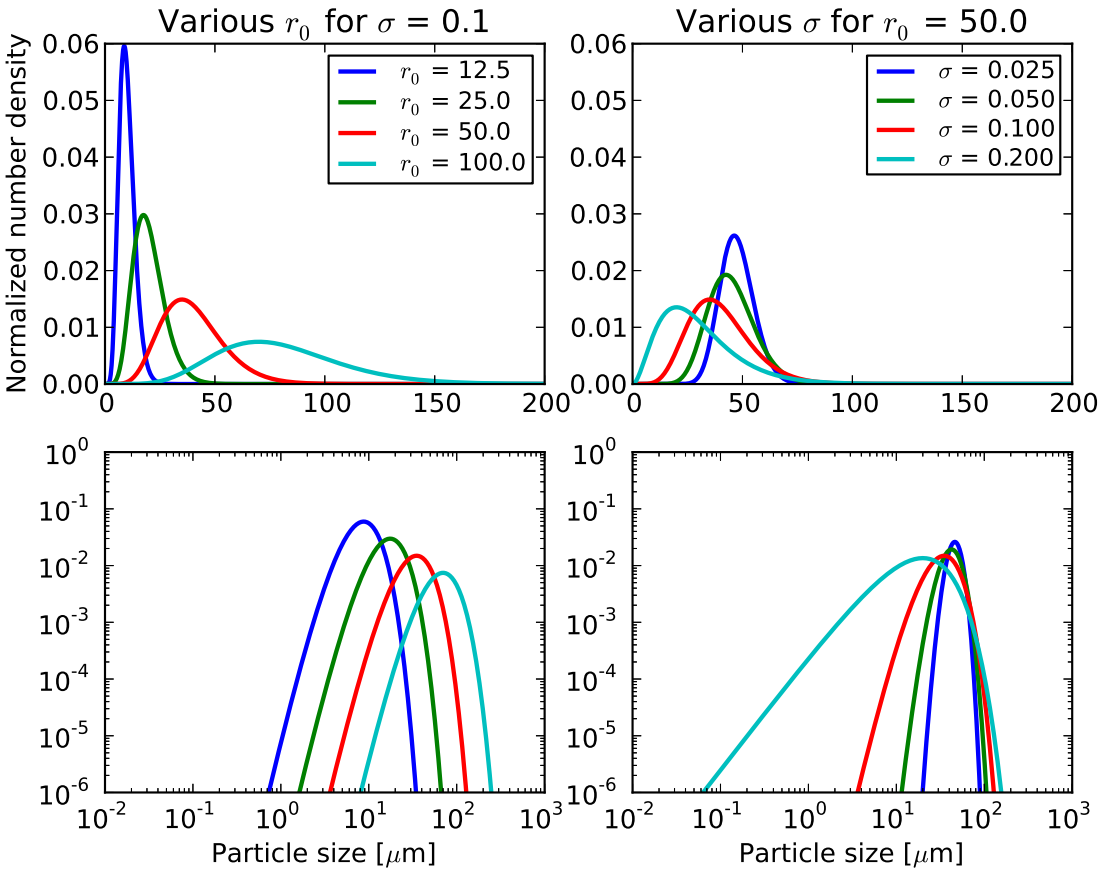

Figure 5.2 Gamma function PSDs in the alternate form defined in Hansen and Travis (1974) for various values of the PSD size parameter and PSD width parameter.

Bulk single scattering properties are computed by the appropriately weighted integrals. The key properties for LBLDIS are the extinction efficiency, single scatter albedo, and phase function. The integrals can be expressed as follows, using the single size data computed for a single habit (Baum et al., 2007):

$$\bar{Q}_{\text{ext}}(\nu; r_0, \sigma) = \frac{\int_{r_1}^{r_2} Q_{\text{ext}}(\nu, r) A(r) N(r; r_0, \sigma)\, dr}{\int_{r_1}^{r_2} A(r) N(r; r_0, \sigma)\, dr} \tag{5.6}$$

$$\bar{\omega}(\nu; r_0, \sigma) = \frac{\int_{r_1}^{r_2} \omega(\nu, r) Q_{\text{ext}}(\nu, r) A(r) N(r; r_0, \sigma)\, dr}{\int_{r_1}^{r_2} Q_{\text{ext}}(\nu, r) A(r) N(r; r_0, \sigma)\, dr} \tag{5.7}$$

$$\bar{P}(\theta, \nu; r_0, \sigma) = \frac{\int_{r_1}^{r_2} P(\theta, \nu, r) \omega(\nu, r) Q_{\text{ext}}(\nu, r) A(r) N(r; r_0, \sigma)\, dr}{\int_{r_1}^{r_2} \omega(\nu, r) Q_{\text{ext}}(\nu, r) A(r) N(r; r_0, \sigma)\, dr} \tag{5.8}$$

Each single scattering property is a function of wavenumber (ν) and PSD parameters (r_0 and σ), and the phase function is additionally a function of the scattering angle θ. These values are pre-computed and stored within databases for LBLDIS. The LBLDIS input parameter contains wavenumber and effective radius, so a simple numerical inversion routine is used to compute the required r_0 parameter values for the desired grid values in r_e. The sigma parameter is not an input parameter for LBLDIS so must be adjusted by recomputing the database at the desired σ value. Example single scattering properties computed from the column aggregate data are shown in figure 5.3.

5.1.3 Surface Emissivity

The spectral variation of surface emissivity can interfere with cloud property retrievals. The MIR window (roughly 750–1250 cm^{-1}) contains the important spectral features related to the refractive index of ice that allow cloud property retrieval. Particle effective radius can be estimated from the slope of the spectrum through the IR window (Huang et al., 2004). Any slope due to spectral changes in the surface emissivity can introduce bias errors in cloud property retrievals by altering the spectral slope. For the clear sky simulations, this was not a serious concern, since the impact on thermodynamic profile retrieval is not as important. In those simulations a constant surface (graybody) emissivity is assumed. For these cloudy simulations, an approximate surface

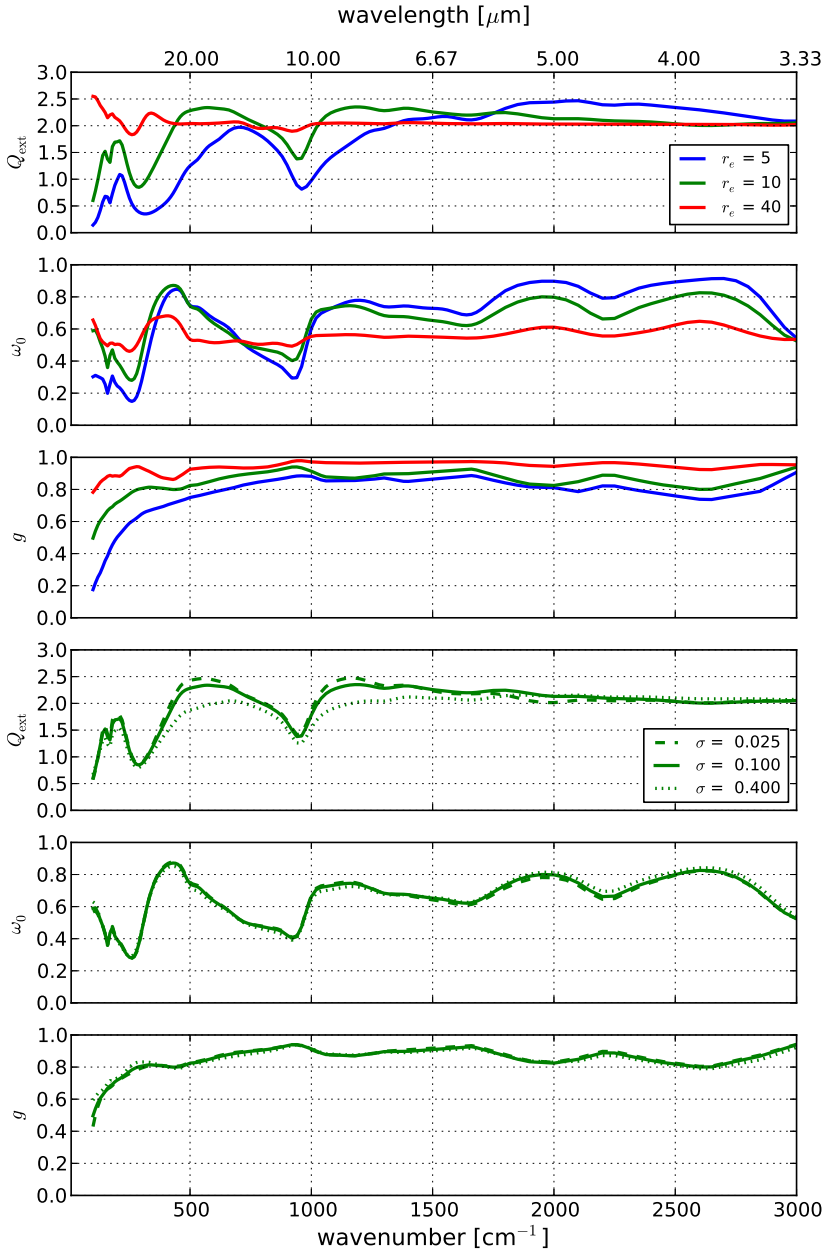

Figure 5.3 Bulk single scattering properties computed for solid column aggregates. Top three plots show the primary scattering properties ($Q_{\rm ext}$, ω_0, and g) for three values of effective radius, and σ = 0.1 for the PSD width parameter. The bottom three plots show the same scattering properties for three values of the width parameter for r_e = 10 μm. The solid green lines are identical for each pair of scattering property plots in the top and bottom plot groups.

spectral emissivity shape is used that represents a linear mixture between soil-like and vegetation-like surface spectral emissivity (**?**). The soil-like emissivity shows a strong feature at 1100–1200 cm^{-1} which is highly correlated to the spectral emissivity of quartz measured in the lab (figure 5.4). The soil-like spectral emissivity is extrapolated to the FIR by using a spectral fit of the quartz emissivity spectrum. There are no spectral emissivity measurements of vegetated surfaces in the FIR, so the vegetation-like emissivity spectrum is assumed to be flat with $\epsilon = 0.997$. A simple composite surface emissivity is used with the spectrum equal to the sum of the soil-like and vegetation-like spectra with the constraint that the two coefficients must sum to unity:

$$\epsilon(\nu) = a\epsilon_{\text{soil}}(\nu) + (1-a)\epsilon_{\text{veg}}(\nu) \tag{5.9}$$

Because of the constraint, the emissivity has only one coefficient to represent the relative weight of the two spectra. The assumed prior mean state for the surface emissivity coefficient is 0.5 (equal weighting). Figure 5.4 shows the equal weighted spectrum with the endmember spectra (a = 1 or 0, indicating 100% soil-like or vegetation-like spectra).

5.1.4 State Vector

As with the clear sky simulations, the state vector contains the profiles of atmospheric temperature and logarithm of the water vapor mass mixing ratio. The mean profile is taken from the standard atmosphere data (Anderson et al., 1986) rather than the computed priors from ACRF radiosonde data. The following variables are added to the state vector to describe cloud and boundary properties: cloud visible optical depth, PSD size parameter r_0, PSD width parameter σ, cloud top altitude, surface temperature, and surface emissivity coefficient. The entire state vector for the cloudy sky simulation can be expressed as:

$$\mathbf{x} = [\tau, r_0, \sigma, z, T_{\text{s}}, a, T(z_k), \ln(q(z_k))]^T \tag{5.10}$$

The assumed prior covariance for these additional components is assumed to be diagonal, while the temperature and water vapor profiles have the synthetic correlation structure shown in figure 3.2. Table 5.1 shows the assumed prior variance for each variable. These are ad hoc selections but

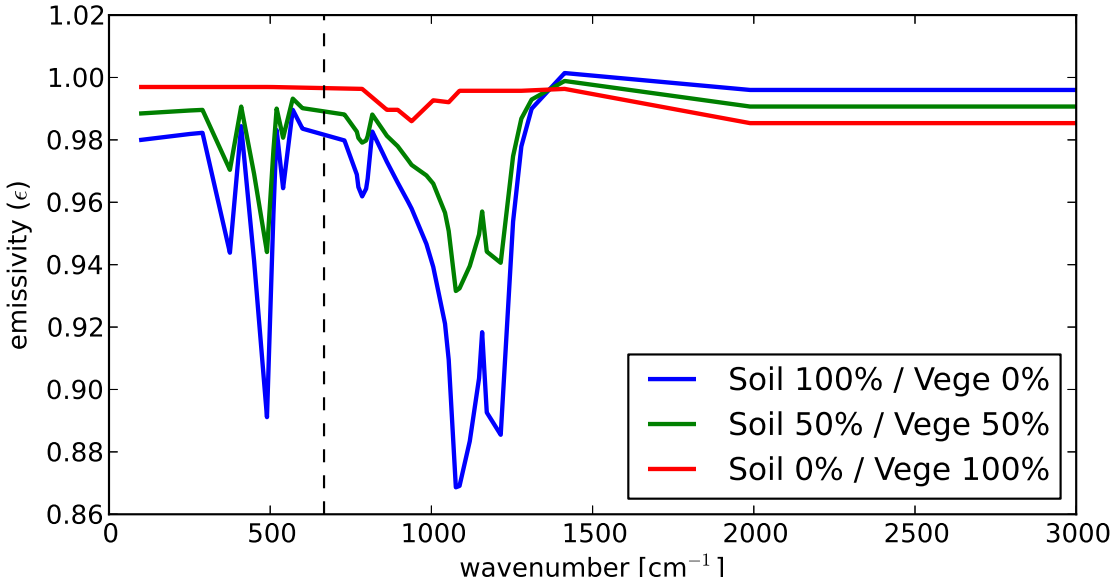

Figure 5.4 Spectral surface emissivity model containing a soil-like and vegetation-like MIR spectra, extrapolated into the FIR using the quartz emissivity spectrum in Christensen et al. (2000).

Table 5.1 Assumed prior variances for additional profiles in cloudy simulations

Variable	Variance	Units	Note
optical depth (τ)	25	N/A	increased to τ^2 when $\tau > 5$
PSD size parameter (r_0)	200^2	μm^2	
PSD width parameter (σ)	0.25	N/A	
cloud height (z)	4	km^2	
surface temperature (T_s)	4	K^2	
emissivity coefficient (a)	50^2	Pct.	

are intended to represent relatively good prior information on the cloud boundaries (cloud height and surface temperature) but little prior information on cloud properties (cloud optical depth and PSD parameters) and the surface emissivity coefficient.

5.1.5 Model Error

The layer cloud assumption is a significantly limiting approximation, since real clouds are rarely homogeneous over a typical satellite sounder's field of view (~ 10 km). The forward model error introduced by this assumption is difficult to estimate, but a simple approximation can be made by using the independent pixel approximation and simulating the sensor field of view as a collection of smaller subpixels. The independent pixel assumption is less limiting as long as highly three dimensional cloud fields (e.g., fair weather cumulus) are avoided. The focus of this research is high altitude ice clouds, such as cirrus and convective anvils, so the problematic three dimensional cases are avoided.

The forward model error approximation is computed by computing a number of 4 sub-pixel spectral radiances and averaging the results to get a single simulated radiance. Each of the 4 sub-pixel clouds is assigned a random τ value, such that the mean of the 4 values is equal to some selected fixed value and the variance is equal to 10% of the mean. For example a cloud with an optical depth of 10 could have a sub-pixel realization with the four optical depth values 9.1, 10.2,

11.3, and 9.4. The simulated radiance is then the mean of the radiance computed for the four individual τ values. Because the radiance has a nonlinear relationship to τ, this mean radiance will not be equal to the radiance of a single simulation with $\tau = 10$. Repeating this calculation for a large number of realizations produces many spectral radiances all with the same average τ value (10 in this case), from which a spectral covariance can be computed. For these experiments, the random variation is a Gaussian random variable with mean 1 and standard deviation 0.1 that multiplies the optical depth value. The model error must be computed for each set of cloud properties. The computed error depends strongly on cloud optical depth and cloud height with particle size and habit causing smaller higher order affects. Thus, the model error is pre-computed for several optical depth values for the tropical standard atmosphere for the column aggregate habit and an effective particle radius of 5 μm. Figure 5.5 shows an example of the model error covariance for τ = 1. This error covariance is then used in DFS and posterior error calculations by adding it to the sensor noise error covariance (equation 3.4).

5.1.6 IWP and IWP Error Propagation

The total Ice Water Path (IWP) in the cloud layer is a key property connecting the cloud radiative properties to the hydrological cycle in the atmosphere. Dynamic processes lift different amounts of water vapor into the upper atmosphere where it condenses to form ice clouds. Although the radiative forcing of these clouds on the Outgoing Longwave Radiation (OLR) is well measured by satellites, the IWP has not as well known. GCMs also show a wide range in global IWP distributions (John and Soden, 2006). Much of this variation can be accounted by differences in ice particle PSD. Two PSDs with significant shape differences can lead to very different IWP while simultaneously having similar optical depth. Part of the aim of the cloudy profile simulations is to gain some insight about the extent to which hyperspectral measurements constrain the IWP, and if extending the spectral measurement into the FIR will improve the IWP estimate.

The PSD and volume-dimensional relationships for the cloud particles are known in these simulations. The IWP of the cloud layer (I) is a straightforward calculation integrating the volume and PSD product to get the Ice Water Content (IWC) and then integrating IWC over the cloud

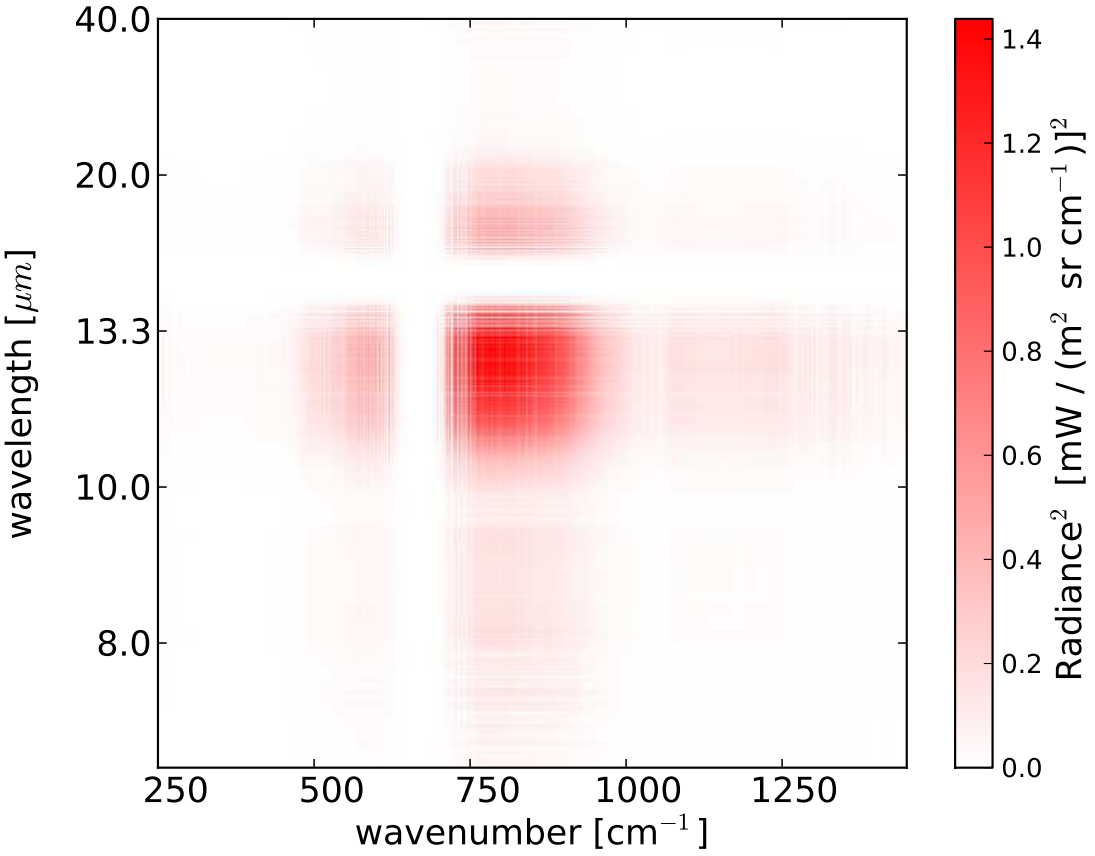

Figure 5.5 Model error covariance for a cloud with optical depth 1.

thickness:

$$I = \int_{z_1}^{z_2} \left[\rho_{\mathrm{i}} \int_{r_1}^{r_2} N_0 V(r) N(r; r_0, \sigma)\, dr \right] dz \tag{5.11}$$

where ρ_{i} is the mass density of bulk ice, 0.917 g cm^{-3}, and N_0 is the as yet unspecified constant proportional to the total particle number density (recall that the size distribution $N(r)$ is a true PDF, so it integrates to unity and has units of inverse length). The expression can be rearranged in a more convenient form by first writing the visible optical depth ($Q_{\mathrm{ext}} = 2$) as another double integral of similar form to the IWP equation above:

$$\tau = \int_{z_1}^{z_2} \left[\rho_i \int_{r_1}^{r_2} N_0 2A(r) N(r; r_0, \sigma)\, dr \right] dz \tag{5.12}$$

Rearranging the equation for I and then substituting τ gives the following equation for I in terms of known quantities:

$$I = \frac{1}{2} \rho_i \tau \frac{\int_{r_1}^{r_2} V(r) N(r; r_0, \sigma)\, dr}{\int_{r_1}^{r_2} A(r) N(r; r_0, \sigma)\, dr} \tag{5.13}$$

Given a posterior covariance $\hat{\mathbf{S}}$, standard error linear propagation can be used to compute the variance on the IWP:

$$\sigma^2_{\mathrm{IWP}} = K^T_{\mathrm{IWP}} \hat{\mathbf{S}} K_{\mathrm{IWP}} \tag{5.14}$$

The term K_{IWP} is the Jacobian of equation 5.13 with respect to the state variables τ, r_0 and σ. K_{IWP} is a three element column vector, since the other state variables (thermodynamic profile, cloud height, surface properties) do not affect the IWP calculation. The components of K_{IWP} are presented in Appendix B.

5.2 Results

The main calculations for the cloudy profile investigation are the OE metrics at the prior mean profiles. The metrics are computed in a grid spanning a section of state space across optical depth and cloud particle size. An approximately logarithmic grid for cloud optical depth is used to span the range 0.02–50 with 11 discrete values. For particle effective radius, five values from 5 μm to

75 μm are selected. A single cloud is simulated at 14 km altitude for the tropical profile and 10 km altitude for the subarctic profile. For the particle distribution, the width parameter σ is set to 0.1 and the solid column aggregate habit is used.

5.2.1 Thermodynamic Profile

ΔDFS for the thermodynamic profiles showing the difference between combined measurements and MIR-only measurements are shown in figure 5.6. With this sign convention, a positive ΔDFS implies the FIR adds new information to the MIR measurement. The temperature profile shows significant through-cloud DFS increase for the smallest particle size and little increase for the large particle size. At the small particle size, the increased DFS is shown for all but the $\tau = 50$ profile, meaning radiance from below the cloud is transmitted even for the $\tau = 20$ cloud. The significant drop in Q_{ext} in the FIR for small particles implies a much lower optical depth. At 300 cm^{-1}, Q_{ext} drops to about 20% of the visible optical depth, so the $\tau = 20$ cloud has an optical depth as low as 4 in the FIR (figure 5.3). At slightly higher wavenumbers (400 cm^{-1}) the Q_{ext} rises to about 50% of the visible optical depth at the same time the single scatter albedo rises to 0.85 which will also increase the cloud transmittance. For larger particle sizes, the Q_{ext} increases and ω_0 decreases, resulting in less transmittance through the cloud layer.

In addition to the increased information in the water vapor and temperature profiles below the cloud, the water vapor profile shows increased information above the cloud. The increase above the cloud is caused by the changed Jacobian profile shapes that result from the interaction between water vapor and the cloud layer. In the clear sky case, there are many weighting functions centered on water vapor absorption lines that peak near or below the cloud altitude. A high optical depth cloud has the effect of truncating the weighting function at the cloud altitude. The truncated weighting function is much narrower since it only contains the high altitude tail of the clear sky weighting function. In addition, the scattering of the cloud layer in the FIR creates cases where the sign of the water vapor Jacobian changes sign near the cloud top. In clear sky cases, an increase in water vapor will always lead to a decrease in radiance, due to the lapse rate in the troposphere. Higher water vapor will block radiance from lower, warmer layers, and emit at colder emission

temperatures. Higher water vapor inside a partially reflective cloud can have the opposite effect, by essentially reducing the effective single scatter albedo of the ice particle and water vapor mixture. In these cases an increase in water vapor can increase the radiance. Figure 5.7 shows several example Jacobian profiles at FIR wavenumbers with different amounts of ice particle scattering. Compared to the clear sky, the cloudy atmosphere does tend to produce sharper and more independently shaped Jacobian profiles for upper troposphere water vapor in this case. Both of these effects increase the DFS of the water vapor profile.

Finally, recalling the relative advantage of the FIR over the MIR for cold upper atmosphere temperatures (discussed in section 2.3.2), the actual radiance signature associated with the water vapor changes will be larger in the FIR. The MIR Jacobian profiles in figure 5.7 show much smaller magnitudes and would be associated with a much smaller information content for the water vapor profile. The result is the significant DFS increase above the cloud when combining the FIR spectra with the MIR. The increase appears strongest for the higher cloud optical depth, as shown in figure 5.6.

The total profile DFS (sum of temperature and water vapor DFS profiles) can be summed for the below cloud and above cloud layers to show the effect with respect to radius and cloud optical depth more clearly (figure 5.8). The additional DFS added due to the cloud reflectance or transmission can be estimated by subtracting the value for the lowest τ value. The additional DFS above the cloud is fairly small, peaking at roughly 0.4 DFS. The below cloud shows a much stronger effect, peaking at 3–4 additional DFS in the ideal conditions of large τ and small particle size.

5.2.2 Cloud Microphysics

For each cloud property state variable, the DFS is plotted individually as a series of lines (one per effective radius) as a function of cloud optical depth alongside the posterior error for the same variable. Figures 5.9 and 5.10 show the results for the MIR-only measurements and the combined measurements, respectively. A number of important qualitative features stand out in the MIR-only measurements. First, for cloud optical depth, the DFS is nearly one at optical depths below 20 with

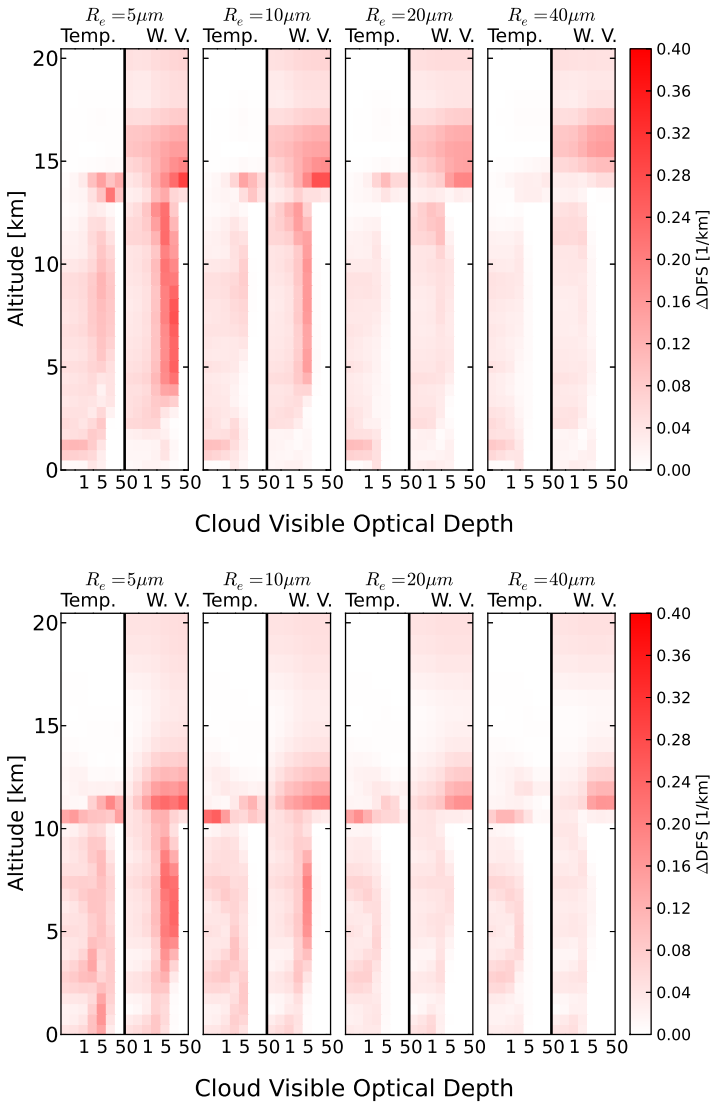

Figure 5.6 ΔDFS profiles (combined minus MIR) for clouds with different particle effective radii. The x axis in each image is an approximately logarithmic spacing in cloud visible optical depth from 0.1 to 50. (Top) tropical atmosphere with cloud layer at 14 km and (bottom) subarctic winter atmosphere with cloud layer at 10 km.

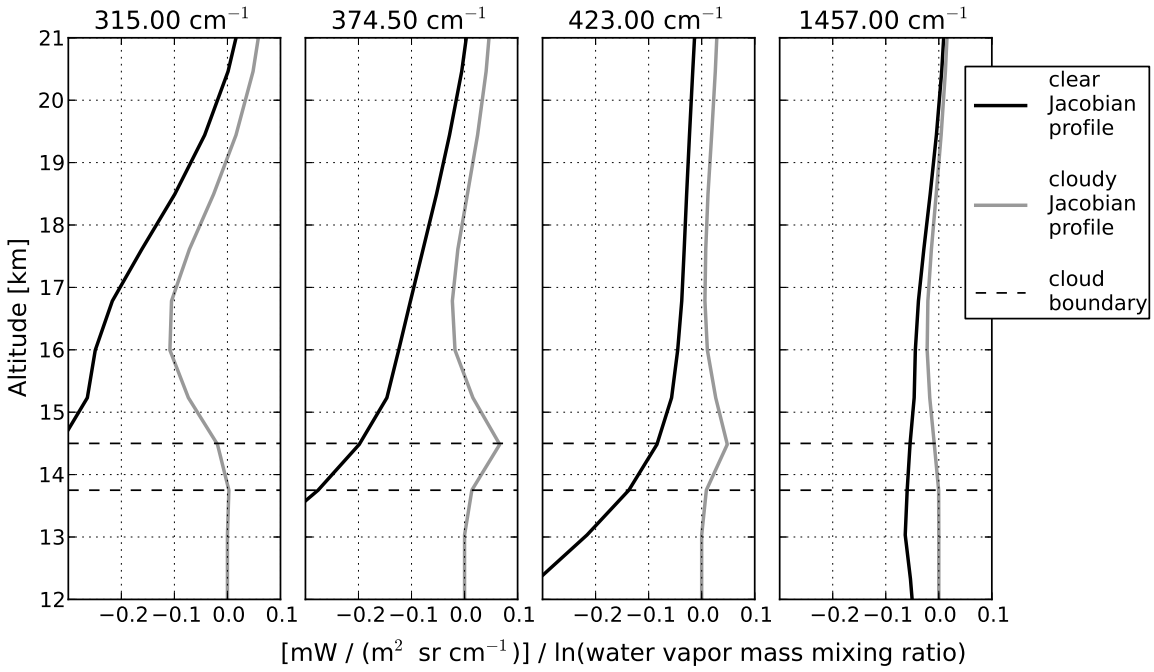

Figure 5.7 Selected Jacobian profiles for nearly clear sky ($\tau = 0.02$, black lines) and high optical depth cloud layer ($\tau = 50$, gray lines) in a standard tropical atmosphere. All selected wavenumbers are centered on strong water vapor absorption lines. The three FIR wavenumbers show significant differences in the Jacobian profile. All MIR Jacobian profiles show a similar shape to the single profile shown here.

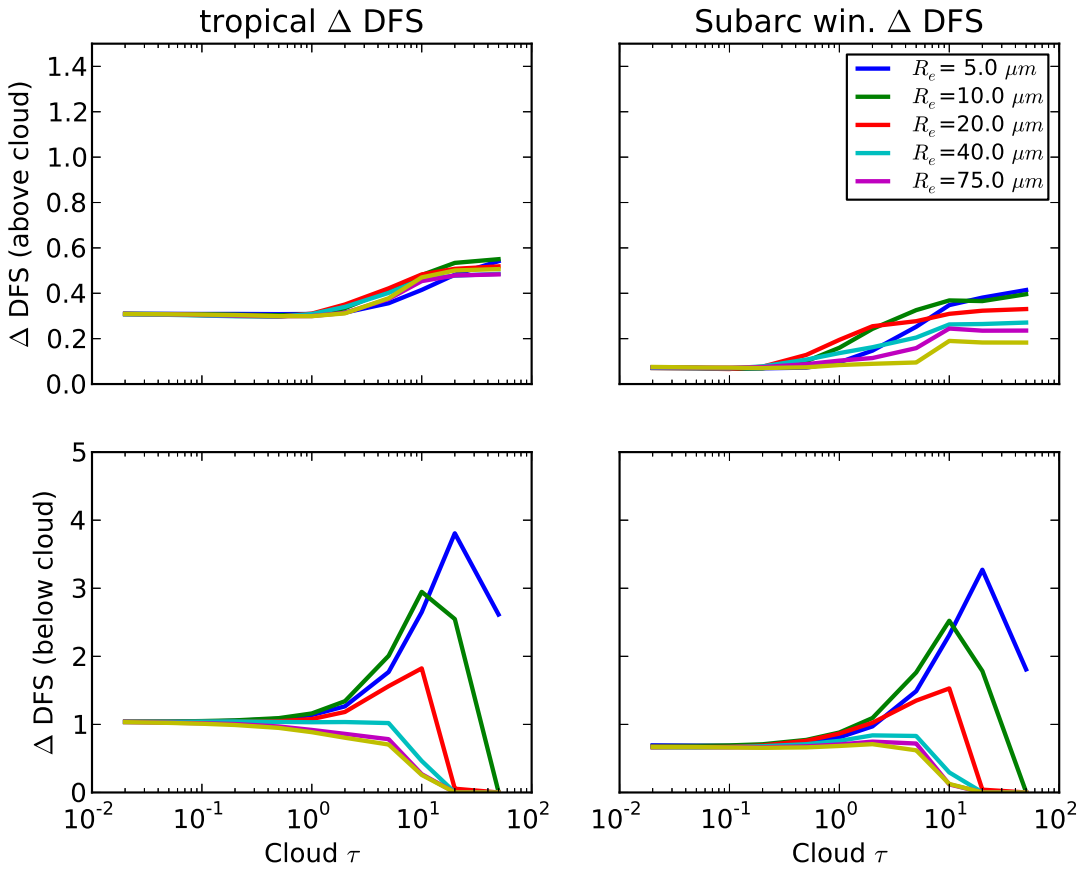

Figure 5.8 Summed ΔDFS for all above cloud levels (top row) and below cloud levels (bottom row), for the results shown in figure 5.6.

a steep drop for the highest values of optical depth. Since the prior variance for optical depth is 25, the DFS is large even for very thin clouds since the retrieval can strongly constrain the optical depth to be near zero. The posterior error, expressed as a fractional error, does show that the error increases for thin clouds as expected. The posterior error is similar for all particle sizes, with a minimum error of a few percent in the region of highest sensitivity ($1 < \tau < 5$). The error increases to $> 20\%$ for the smallest τ and increases to the prior error for the large τ. Similar patterns are seen in both particle PSD parameters (r_0 and σ). The best sensitivity is for moderate range in optical depth. The performance is poor at low τ (< 0.5) due to the smaller magnitude radiance signature. At high τ (> 10) the performance is poor due to the cloud emissivity becoming near unity at all MIR wavenumbers. The spectral signatures used to retrieve the microphysical properties saturate and the sensitivity is lost. Large particle radii ($>= 40$ μm) also show lower sensitivity, since the scattering properties tend to show less spectral variation as particle size increases.

The cloud height DFS and error shows rapid change as optical depth increases, converging to a minimum error at approximately $\tau = 1$. This behavior is expected since the cloud temperature, and thus cloud height, is measured most accurately when the cloud is opaque. For the surface temperature and emissivity, the DFS and error curve shapes can be entirely explained by the amount of cloud transmittance. For large τ the transmittance drops to zero, in turn reducing the DFS to zero and increasing the posterior error to the prior value. The smallest particle size shows slightly increased DFS and reduced error. Recalling the larger single scatter albedo and smaller extinction efficiency of small particles (figure 5.3), the clouds with small particles should have larger transmittance relative to clouds with larger particles.

Combining the FIR and MIR measurements significantly improves in the microphysical retrieval, but has little effect on the surface property and cloud height retrievals. Since the MIR contains window channels, the radiance contrast between the warm surface and cold cloud temperature allows for accurate τ and z retrievals. The cloud free emission in the FIR is largely from water vapor that is almost always colder than the surface. The result is a much smaller radiance contrast, so the FIR will not significantly improve τ and z retrievals. By adding the FIR spectrum, the microphysical parameters show much improved posterior errors, particularly for the

larger particle sizes and large τ. The MIR spectral signatures tend to saturate in those conditions, as discussed above. The FIR scattering properties show elevated single scatter albedo for a wider range of particle sizes than the MIR, and the lower asymmetry parameter leads to proportionally more backscattering. The result is a partially reflective cloud even for $\tau > 20$ with the spectral shape of the reflective component dependent on the PSD parameters. The reflective signature adds information for the PSD parameters up to the largest τ (50) in all cases but the largest particle size (75 μm). Improvement is also seen in the τ retrieval itself for the large τ cases.

Focusing on the improvement of the FIR spectral measurement, figure 5.11 shows the ΔDFS plots and error reductions computed as the difference between the FIR and combined results. Specifically, the ΔDFS plots show the MIR-only DFS subtracted from the combined DFS, and the error plots show the combined error subtracted from the MIR-only error. The sign choice implies improvement is a positive number for all plots. These plots emphasize the ability of the FIR to improve the retrievals for large τ and large r_e clouds. Little change is seen in clouds with small r_e and moderate τ. In these cases, the sensitivity of the MIR is very large, because the spectral shape of the cloud emissivity changes greatly through the MIR window region. Given our assumed spectral sensor noise, the effective SNR of this signature is far larger in the MIR, so the FIR does little to improve the retrieval of small particles.

5.2.3 IWP

Equation 5.14 is applied to the posterior error covariances from the MIR-only and combined FIR + MIR measurements. IWP error expressed as a relative percentage of the total computed IWP is presented in figure 5.12. The general form of the IWP error from the MIR-only measurement matches expectations based on the shape of the DFS and posterior error plots shown in figure 5.9. Specifically, increased error is seen for larger particle size, large optical depth, and small optical depth, as discussed in the previous section. By adding the FIR measurement the IWP error is much less dependent on particle size and the large particle IWP error is within a factor of 1–2 of the small particle IWP error in the range of good sensitivity ($0.1 < \tau < 10$). The error reduction for small particles and large τ is quite dramatic with just over a 60% reduction.

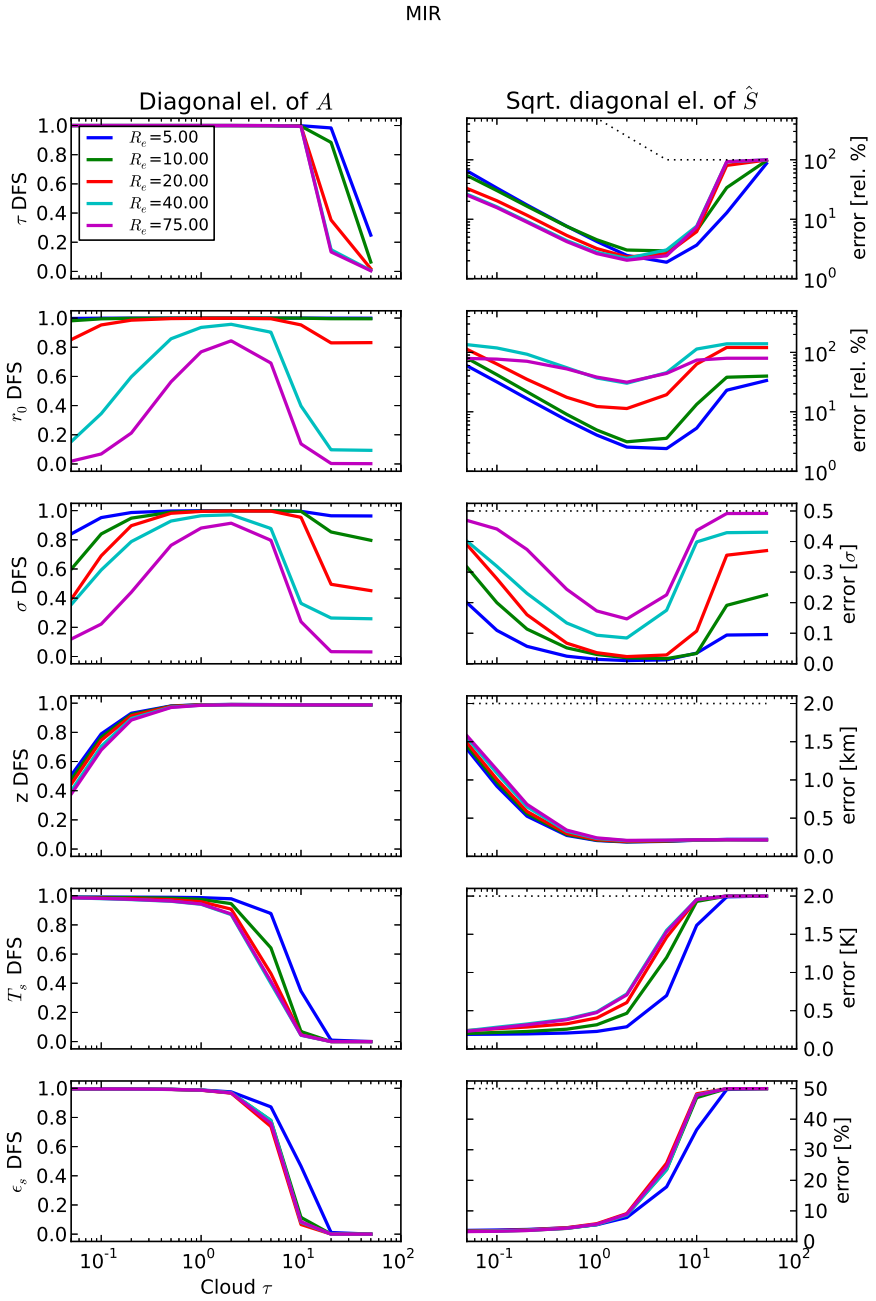

Figure 5.9 Simulated cloud layer at 14 km in a tropical standard atmosphere. (Left) DFS and (right) posterior error for cloud microphysical and boundary variables using the MIR-only measurement. The dotted lines on the right side show the standard deviation in the prior, where applicable.

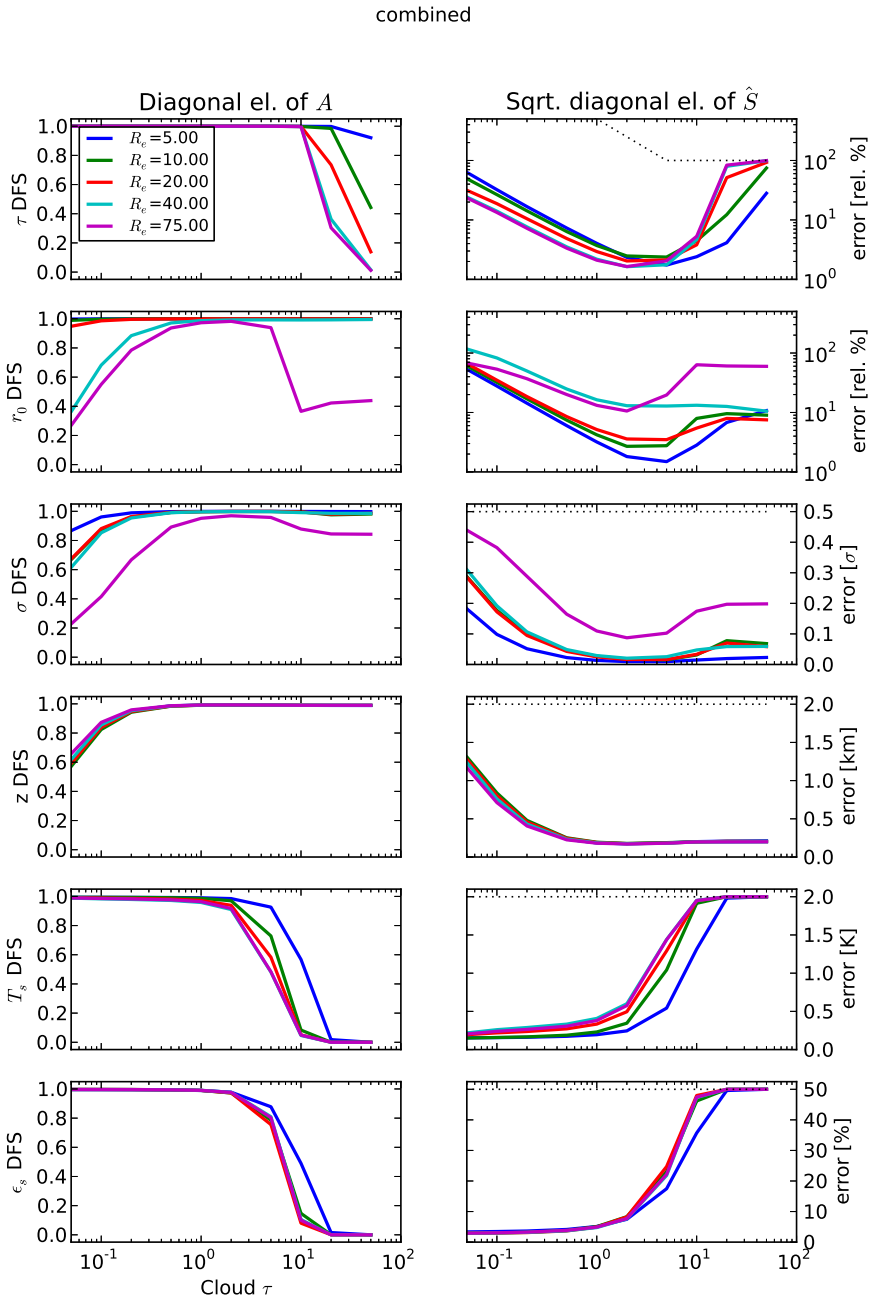

Figure 5.10 Same as figure 5.9, but using combined (FIR + MIR) measurements.

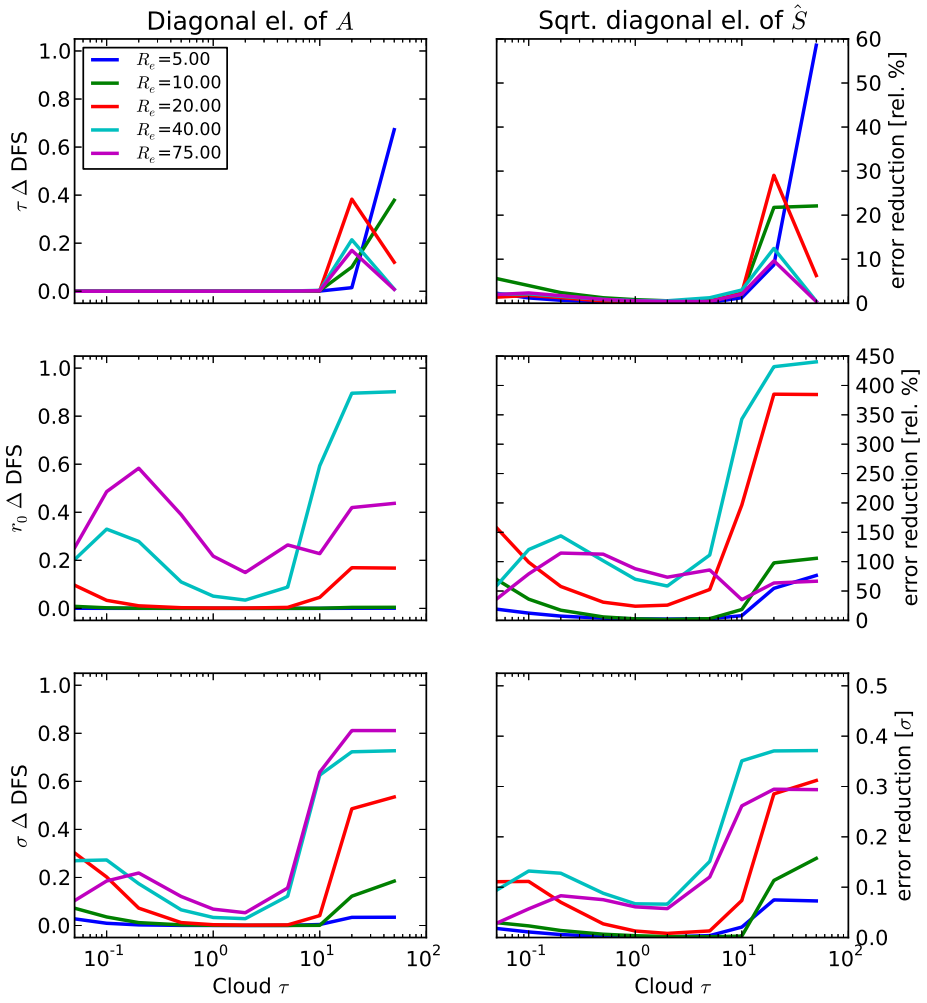

Figure 5.11 For the three cloud microphysical properties, (Left) DFS increase by adding FIR to MIR-only measurements (Right) Reduction in posterior error by adding FIR to MIR-only measurements.

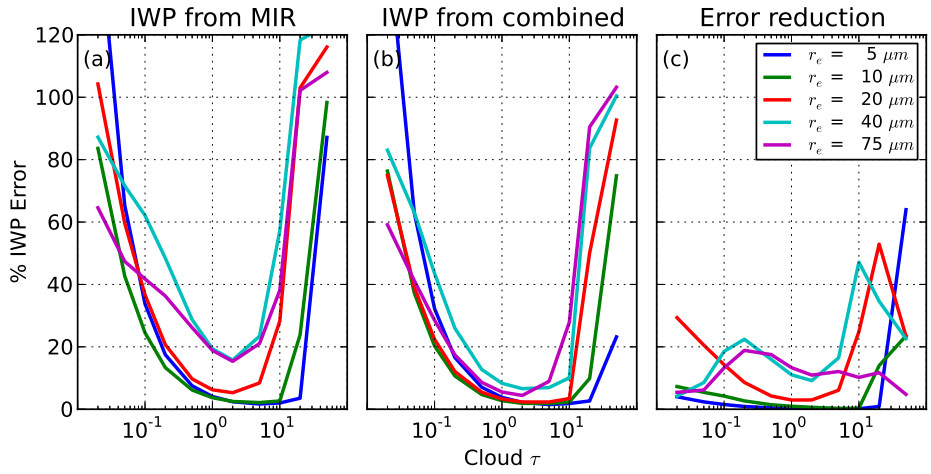

Figure 5.12 (a) percentage IWP error using MIR-only measurement, (b) percentage IWP error using combined FIR + MIR measurement, and (c) reduction in IWP error from combining FIR to MIR measurement (data from (a) minus data from (b)). Simulations using high altitude cloud layer in tropical atmosphere (same as figures 5.9 – 5.11).

5.3 Summary

Using simulations of cloudy sky profiles, extending the MIR spectral measurement into the FIR improved retrievals of thermodynamic profiles and cloud microphysical properties. For through-cloud profiling, the improvement is primarily for thick clouds with very small ice particle size ($r_e < 10$ μm) which is not likely a common occurrence in the real atmosphere. Very small particles can occur in orographically forced clouds (Kahn et al., 2003), but typical particle sizes in cirrus clouds from global retrievals are generally in the range $10 < r_e < 50$ μm (Radel et al., 2003). The higher transmittance does imply a different vertical sensitivity to the cloud particle distribution. Highly scattering FIR wavenumbers should have weighting functions that extend further into the cloud compared to wavenumbers with lower scattering. Whether this could lead to retrievable information on the vertical variation of particle size is a topic for future research.

The increase in above cloud information content in the thermodynamic profile is a more generally useful result. The increased DFS occurs in the upper troposphere and lower stratosphere, where water vapor measurement is particularly important for climate studies due to its important role in water vapor feedback, modulation of clear sky OLR, and clear sky cooling rates.

Combining FIR and MIR measurements also shows improved retrieval of IWP. The largest improvement is shown in high optical depth clouds. It should be noted that thick clouds are much more likely to have vertically inhomogeneous particle distributions. In retrievals using observations of real clouds, the IWP for thick clouds would be poorly estimated for any FIR or MIR measurement simply due to the fact that the lower levels of the cloud are obscured in the measurement. Observations of much longer wavelengths such as microwave or submillimeter are required in this case (Buehler et al., 2007). The improvement in IWP retrieval for moderate τ and large particle size is of more practical use.

Chapter 6

Discussion

6.1 Applications of FIR Radiative Transfer and Remote Sensing

6.1.1 FIR Small Particle Signatures in Anvil Clouds

In convective storms, strong updrafts can produce ice particles that are smaller than the ice particles in the surrounding anvil cloud. This Small Particle Signature (SPS) can be detected as an isolated area of smaller particle effective size embedded in the larger anvil cloud. The SPS are associated with reflectivity detections in ground based radar that indicate strong convective updrafts (Hart, 2012). Figure 6.1 shows an example retrieval of ice particle effective size using the Daytime Cloud Optical and Microphysical Properties (DCOMP) algorithm (Walther and Heidinger, 2012). In this case DCOMP is applied to imager data collected from a geostationary weather satellite. The algorithm uses shortwave channels (wavelength 0.6 μm and 3.9 μm) to retrieve particle effective size. Since the FIR has information about particle size for optically thick clouds, FIR measurements may be able to detect these SPS at night when the DCOMP algorithm is not applicable.

In figure 6.1, the two circles identify SPS within the observed anvil clouds. The SPS show ice particle effective radii in the range 15–20 μm, while the surrounding anvil has an effective radii of > 30 μm. Different types of anvil clouds described in Hart (2012) show a wider range of particle effective radii, but the SPS typically shows retrieved radii of 10–15 μm smaller than the surrounding anvil. For a simple sensitivity test, spectral radiances are simulated to show the MIR and FIR brightness temperature contrast between the SPS and surrounding anvil cloud. Two situations are simulated based on the typical effective radii ranges noted above. In each case, the cloud layer is simulated with an optical depth of $\tau = 20$. In the first case, the SPS and anvil

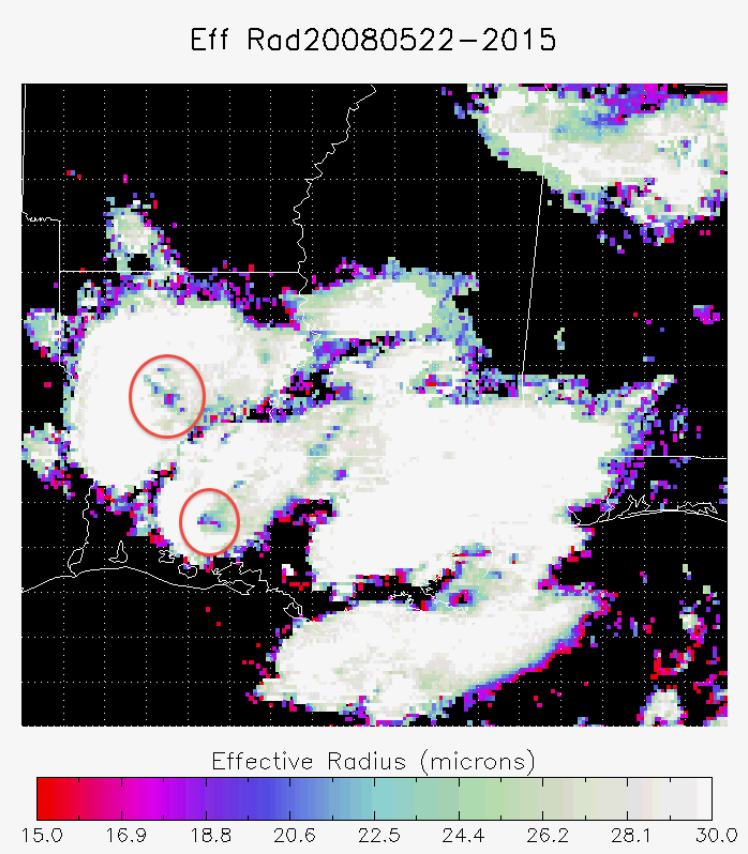

Figure 6.1 DCOMP retrieved ice particle effective size in convective anvil clouds over south central United States. These clouds were observed on May 22, 2008, in multispectral imagery from a geostationary satellite. The orange circles mark Small Particle Signatures ($r_e < 20$ μm surrounded by $r_e > 30\mu$m) that are associated with strong convective updrafts. Figure from Hart (2012).

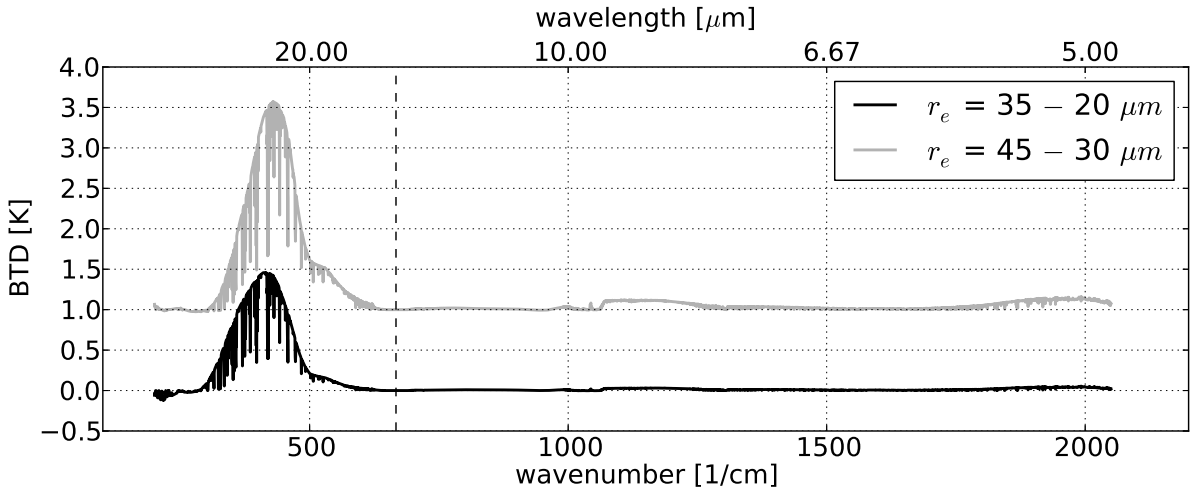

Figure 6.2 Simulated brightness temperature difference across the MIR and FIR spectral ranges. Two clouds are simulated, matching DCOMP retrievals of particle effective radius (see figure 6.1). The gray line is offset by +1 K to better show the differences in the two spectra.

have effective particle radii of 20 and 35 μm and in the second case the radii are 30 and 45 μm. The standard midlatitude summer profile is used for the atmosphere. DCOMP uses the scattering property database from Baum et al. (2007), which is based on the same single size scattering data (Yang et al., 2005) used in these simulations. The particle habit used in these simulations is the column aggregate, which does not match the Baum et al. (2007) habit distribution. However, the resulting difference in sensitivity to effective particle radius should be small. For each of the two pairs of effective radii, the two spectral radiances are computed and subtracted to get a brightness temperature difference spectrum. The difference spectra show which wavenumbers would be sensitive to the difference in particle size between the SPS and anvil. These spectra are shown in figure 6.2. The MIR wavenumber range shows maximum differences of about 0.1 K, while the peak scattering wavenumbers in the FIR (400 cm^{-1}) show 1.5–2.5 K difference. These spectral differences suggest that a FIR imager channel with a noise level below 1 K in brightness temperature could detect the SPS.

6.1.2 FIR Radiative Transfer in GCMs

In large domain atmosphere models such as General Circulation Models (GCMs), the primary radiative quantity is the vertical profile of the spectrally integrated flux. The flux profile is directly related to the heating rate, which in turn couples the radiation field to dynamical processes in the atmosphere. The spectrally resolved flux or radiance is not directly important, since the spectrally integrated quantity is what controls the heating rate profile. Typically the radiative transfer implemented within these models uses optimized parameterizations over a relatively small number of wide spectral bands covering the entire spectrum (longwave and shortwave). These optimized methods are tuned to reproduce the heating rate profiles computed with more accurate but computationally expensive reference codes. The FIR is particularly important since a large fraction of the clear sky longwave heating occurs in this spectral range (Clough et al., 1992). Any updated knowledge of FIR radiative transfer should lead to updated parameterized codes used in GCMs or other forecast models.

One such parameterized model, the Rapid Radiative Transfer Model developed at AER (RRTM, Mlawer et al. (1997)) is based on the same MT_CKD water vapor continuum as used in the LBLRTM. Recent field campaign data has led to updates in the MT_CKD continuum parameters in the FIR (Turner and Mlawer, 2010). Since the RRTM is used within the Community Earth System Model (CESM), a coupled GCM developed at the National Center for Atmospheric Research (NCAR), the changes to the FIR water vapor continuum can be quickly adapted to the model. The change to the water vapor continuum absorption introduces an altered profile in the clear sky heating rate. The zonal average clear sky heating rate change is shown in Figure 6.3. The model quickly adjusts to this energy imbalance by adjusting the temperature, cloud and water vapor fields. The higher altitude layer that is heated by the changed water vapor absorption warms and the relative humidity drops. Lower humidity causes a slight drop (0.5%) in global cloud cover. The pattern of zonal heating changes due to the cloud and humidity adjustment in a way that tends to cancel the heating change introduced by the water vapor continuum model update. This set of GCM runs shows a direct connection between the clear sky radiative transfer parameterizations and the model thermodynamic fields. No significant changes were noted in the model's dynamical fields, as the

thermodynamic and cloud adjustment appeared to balance. The gradual improvement of radiative transfer parameterizations can be noted by comparing the impact of this recent MT_CKD update to those in the previous generation of radiation parameterizations (Collins et al., 2002). In this earlier study, the pattern of zonal heating change from the longwave radiative transfer update shows a qualitatively similar pattern in the upper troposphere ($P < 500$ hPa), but shows a larger magnitude by roughly a factor of 5.

6.2 Future Research

The results presented in this study show a number of potential advantages in extending hyperspectral measurements into the FIR spectral region. The calculations are dependent on high accuracy prior knowledge about the gas absorption spectral properties and the single scattering properties of ice particles. For the clear sky problem, the calculations rest on the AER line database and the MT_CKD water vapor continuum absorption model. These datasets are well validated with a number of ground observations (Turner and Mlawer, 2010). The simulation of upwelling radiance spectra should also be quite accurate, although validation data in the FIR is still quite limited. The FIR spectroscopic database has not been validated to the level of the MIR. In the cloudy sky profile, the scattering properties are less well validated. Measurements of the upwelling spectrum are even more important to validate cloud properties, since very little of the cloud radiance would be observable from the ground. Much of the potential added utility of FIR observations is related to measuring thick clouds, which are not present in dry and high altitude conditions ideal for ground based FIR measurements. This research does highlight the need for further targeted field campaigns to address these issues. Possible research programs include:

- Further observations of the clear sky FIR spectrum from high altitude aircraft platforms. The TAFTS instrument collected such data in the EQUATE field campaign (Cox et al., 2007). This existing dataset is limited and not able to validate the FIR radiative transfer to the extent that is needed. More low noise, high spectral resolution measurements are still needed to address the clear sky radiative transfer.

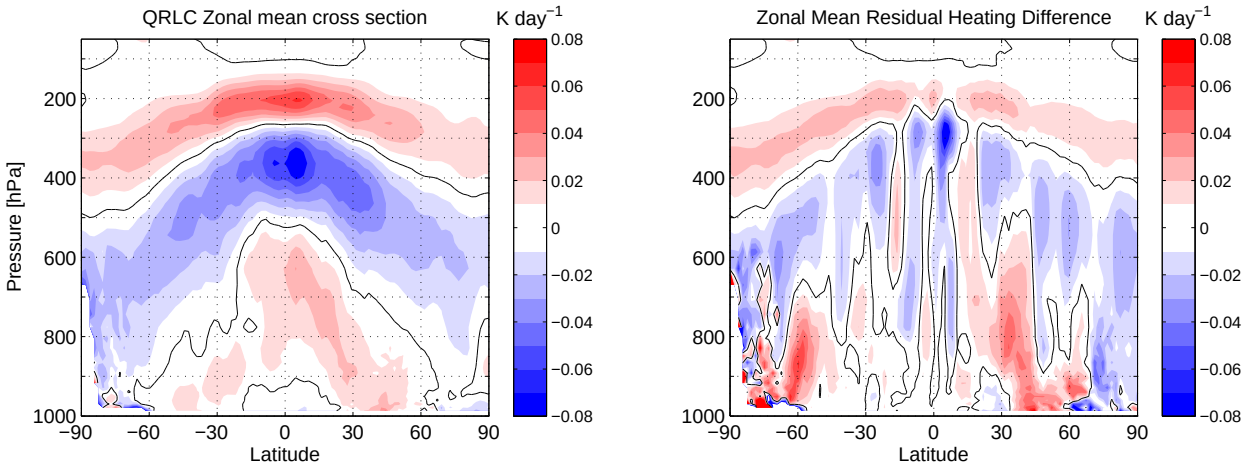

Figure 6.3 (Left) the zonally-averaged clear sky longwave heating rate change between a control CESM run (using the default RRTM and MT_CKD water vapor continuum model) and an experimental CESM (using RRTM modified to include a updates to the MT_CKD water vapor continuum based on FIR measurements). (Right) zonally-averaged total heating rate change. The total heating rate includes including clear sky longwave and shortwave heating rates, cloud forcing, latent heating, and heating from subgrid turbulent diffusion parameterizations. The total heating rate change shows that the adjustment to the various model fields (clouds, temperature, and humidity) tend to reduce the heating rate change introduced by the MT_CKD update. Figure from Turner et al. (2012).

- Observations of the upwelling FIR spectrum in the presence of clouds are needed. Some limited data does exist for cirrus clouds (Cox et al., 2010), but a larger dataset is needed, for a wider range of cloud conditions. The results of this dissertation suggest potential benefits for FIR observations of anvil clouds, which would require newly designed field campaigns targeting these cloud types.

- Of particular importance is better validation of the different ice crystal habits within the single scattering property databases. Observations combining near IR (reflected solar radiation) and MIR are particularly useful to help constrain habit (Baran and Francis, 2004), and it would be very informative to repeat similar measurements but combine FIR, MIR, and reflected solar radiation in the near IR or visible wavelengths. Radiative closure over the entire thermal and reflected solar wavelength range is needed to produce self consistent scattering models.

- Measurements of FIR surface emissivity are also needed where the microwindows are located. Even for moderately dry midlatitude atmosphere profiles, there will be some emission from the surface. There are no documented observations of FIR emissivity other than the mineral data referenced in this study (Christensen et al., 2000), so it is not known if there are features due to other natural surfaces (vegetation in particular) that may complicate FIR retrievals.

Integration within GCMs is extremely important for any updates to FIR radiative transfer. This is especially important for ice scattering in the FIR, since it is likely to show the largest changes as our understanding improves.

Bibliography

Ackerman, T. P. and G. M. Stokes, 2003: The Atmospheric Radiation Measurement Program. *Phys. Today*, **56 (1)**, 38–44.

Anderson, G., S. A. Clough, F. X. Kneizys, J. H. Chetwynd, and E. P. Shettle, 1986: AFGL atmospheric constituent profiles. Tech. Rep. AFGL-TR-86-110, Air Force Geophysical Laboratory.

Antonelli, P., et al., 2004: A principal component noise filter for high spectral resolution infrared measurements. *J. Geophys. Res.*, **109 (D23)**, D23 102, doi:10.1029/2004JD004862.

Atlas, D., 1969: Atmospheric exploration by remote probes; final report of the panel on remote atmospheric probing. Tech. rep., National Research Council.

Baran, A. J., 2007: The impact of cirrus microphysical and macrophysical properties on upwelling far-infrared spectra. *Quart. J. Roy. Meteor. Soc.*, **133 (627)**, 1425–1437.

Baran, A. J. and P. N. Francis, 2004: On the radiative properties of cirrus cloud at solar and thermal wavelengths: A test of model consistency using high-resolution airborne radiance measurements. *Q.J.R. Meteorol. Soc.*, **130 (598)**, 763–778.

Barnes, W., T. Pagano, and V. Salomonson, 1998: Prelaunch characteristics of the Moderate Resolution Imaging Spectroradiometer (MODIS) on EOS-AM1. *IEEE Trans. Geosci. Remote Sens.*, **36 (4)**, 1088–1100.

Baum, B. A., P. F. Soulen, K. I. Strabala, M. D. King, S. A. Ackerman, W. P. Menzel, and P. Yang, 2000: Remote sensing of cloud properties using MODIS airborne simulator imagery during SUCCESS 2. cloud thermodynamic phase. *J. Geophys. Res.*, **105 (D9)**, 11 781–11 792.

Baum, B. A., P. Yang, S. Nasiri, A. K. Heidinger, A. Heymsfield, and J. Li, 2007: Bulk scattering properties for the remote sensing of ice clouds. part III: high-resolution spectral models from 100 to 3250 cm-1. *J. Appl. Meteor. Climatol.*, **46 (4)**, 423–434.

Bianchini, G., L. Palchetti, and B. Carli, 2006: A wide-band nadir-sounding spectroradiometer for the characterization of the earth's outgoing long-wave radiation. *SPIE Proceedings*, Vol. 6361, doi:10.1117/12.689260.

Bingham, G. A., N. S. Pougatchev, M. P. Esplin, W. J. Blackwell, and C. D. Barnet, 2010: The NPOESS cross-track infrared sounder (CrIS) and advanced technology microwave sounder (ATMS) as a companion to the new generation AIRS/AMSU and IASI/AMSU sounder suites. *6th Annual Symposium on Future National Operational Environmental Satellite Systems-NPOESS and GOES-R*, American Meteorological Society, Atlanta, GA.

Buehler, S. A., et al., 2007: A concept for a satellite mission to measure cloud ice water path, ice particle size, and cloud altitude. *Quart. J. Roy. Meteor. Soc.*, **133 (2)**, 109–128, doi: 10.1002/qj.143.

Buehler, S. A., et al., 2012: Observing ice clouds in the submillimeter spectral range: the CloudIce mission proposal for ESA's earth explorer 8. *Atmos. Meas. Tech.*, **5 (7)**, 1529–1549, doi:10.5194/amt-5-1529-2012.

Cady-Pereira, K. E., M. W. Shephard, D. D. Turner, E. J. Mlawer, S. A. Clough, and T. J. Wagner, 2008: Improved daytime column-integrated precipitable water vapor from vaisala radiosonde humidity sensors. *J. Atmos. Oceanic Technol.*, **25 (6)**, 873–883.

Canas, T. A., J. E. Murray, and J. E. Harries, 1997: Tropospheric airborne fourier transform spectrometer (TAFTS). *SPIE Proceedings*, Vol. 3220, 91–102, doi:10.1117/12.301139.

Capelle, V., A. Chédin, E. Péquignot, P. Schlüssel, S. M. Newman, and N. A. Scott, 2012: Infrared continental surface emissivity spectra and skin temperature retrieved from IASI observations over the tropics. *J. Appl. Meteor. Climatol.*, doi:10.1175/JAMC-D-11-0145.1.

Carissimo, A., I. De Feis, and C. Serio, 2005: The physical retrieval methodology for IASI: the [delta]-IASI code. *Environ. Modell. Software*, **20 (9)**, 1111–1126, doi: 10.1016/j.envsoft.2004.07.003.

Chaboureau, J.-P., A. Chédin, and N. A. Scott, 1998: Remote sensing of the vertical distribution of atmospheric water vapor from the TOVS observations: Method and validation. *J. Geophys. Res.*, **103 (D8)**, 8743–8752, doi:10.1029/98JD00045.

Chahine, M., H. Aumann, and F. Taylor, 1977: Remote sounding of cloudy atmospheres. III. experimental verifications. *J. Atmos. Sci.*, **34 (5)**, 758–765.

Chahine, M. T., et al., 2006: AIRS: improving weather forecasting and providing new data on greenhouse gases. *Bull. Amer. Meteor. Soc.*, **87 (7)**, 911–926, doi:10.1175/BAMS-87-7-911.

Christensen, P. R., J. L. Bandfield, V. E. Hamilton, D. A. Howard, M. D. Lane, J. L. Piatek, S. W. Ruff, and W. L. Stefanov, 2000: A thermal emission spectral library of rock-forming minerals. *J. Geophys. Res.*, **105 (E4)**, 9735–9739, doi:10.1029/1998JE000624.

Christensen, P. R., et al., 1992: Thermal emission spectrometer experiment: Mars observer mission. *J. Geophys. Res.*, **97 (E5)**, 7719–7734, doi:10.1029/92JE00453.

Clough, S., F. Kneizys, and R. Davies, 1989: Line shape and the water vapor continuum. *Atm. Res.*, **23 (3–4)**, 229–241, doi:10.1016/0169-8095(89)90020-3.

Clough, S., M. Shephard, E. Mlawer, J. Delamere, M. Iacono, K. Cady-Pereira, S. Boukabara, and P. Brown, 2005: Atmospheric radiative transfer modeling: a summary of the AER codes. *J. Quant. Spectrosc. Radiat. Transfer*, **91 (2)**, 233–244, doi:10.1016/j.jqsrt.2004.05.058.

Clough, S. A. and M. J. Iacono, 1995: Line-by-line calculation of atmospheric fluxes and cooling rates 2. application to carbon dioxide, ozone, methane, nitrous oxide and the halocarbons. *J. Geophys. Res.*, **100 (D8)**, 16 519–16 535.

Clough, S. A., M. J. Iacono, and J.-L. Moncet, 1992: Line-by-line calculations of atmospheric fluxes and cooling rates: Application to water vapor. **97**, 15 761–15 785.

Collins, W. D., J. K. Hackney, and D. P. Edwards, 2002: An updated parameterization for infrared emission and absorption by water vapor in the national center for atmospheric research community atmosphere model. *J. Geophys. Res.*, **107 (D22)**, 4664.

Conrath, B. J., R. A. Hanel, V. G. Kunde, and C. Prabhakara, 1970: The infrared interferometer experiment on nimbus 3. *J. Geophys. Res.*, **75 (30)**, 5831–5857.

Cox, C. V., J. E. Harries, J. P. Taylor, P. D. Green, A. J. Baran, J. C. Pickering, A. E. Last, and J. Murray, 2010: Measurement and simulation of mid- and far-infrared spectra in the presence of cirrus. **136**, 718–739.

Cox, C. V., J. E. Murray, J. P. Taylor, P. D. Green, J. C. Pickering, J. E. Harries, and A. E. Last, 2007: Clear-sky far-infrared measurements observed with TAFTS during the EAQUATE campaign, september 2004. *Q.J.R. Meteorol. Soc.*, **133 (S3)**, 273–283.

Crevoisier, C., 2012: IASI-New generation onboard EPS-SG: expected impact on accuracy and vertical resolution for atmospheric variables. *International TOVS Study Conference - 18*, Toulouse, France.

Dils, B., et al., 2006: Comparisons between SCIAMACHY and ground-based FTIR data for total columns of CO, CH4, CO2 and N2O. *Atmos. Chem. Phys.*, **6 (7)**, 1953–1976, doi:10.5194/acp-6-1953-2006.

Divakarla, M. G., C. D. Barnet, M. D. Goldberg, L. M. McMillin, E. Maddy, W. Wolf, L. Zhou, and X. Liu, 2006: Validation of Atmospheric Infrared Sounder temperature and water vapor retrievals with matched radiosonde measurements and forecasts. *J. Geophys. Res.*, **111 (D9)**, D09S15, doi:10.1029/2005JD006116.

Downing, H. D. and D. Williams, 1975: Optical constants of water in the infrared. *J. Geophys. Res.*, **80 (12)**, 1656–1661.

Elwell, J. D., et al., 2006: A geosynchronous imaging fourier transform spectrometer (GIFTS) for hyperspectral atmospheric remote sensing: instrument overview and preliminary performance results. *SPIE Proceedings*, Vol. 6297, doi:10.1117/12.684135.

Evans, K. F., S. J. Walter, A. J. Heymsfield, and G. M. McFarquhar, 2002: Submillimeter-wave cloud ice radiometer: Simulations of retrieval algorithm performance. *J. Geophys. Res.*, **107 (D3)**, 4028.

Evans, K. F., J. R. Wang, P. E. Racette, G. Heymsfield, and L. Li, 2005: Ice cloud retrievals and analysis with the compact scanning submillimeter imaging radiometer and the cloud radar system during CRYSTAL FACE. *J. Appl. Meteor.*, **44 (6)**, 839–859.

Eyre, J. R., 1989: Inversion of cloudy satellite sounding radiances by nonlinear optimal estimation. II: application to TOVS data. *Quart. J. Roy. Meteor. Soc.*, **115 (489)**, 1027–1037, doi:10.1002/qj.49711548903.

Fischer, H., et al., 2008: MIPAS: an instrument for atmospheric and climate research. *Atmos. Chem. Phys.*, **8 (8)**, 2151–2188, doi:10.5194/acp-8-2151-2008.

Fu, Q., P. Yang, and W. B. Sun, 1998: An accurate parameterization of the infrared radiative properties of cirrus clouds for climate models. *J. Climate*, **11 (9)**, 2223–2237, doi:10.1175/1520-0442(1998)011¡2223:AAPOTI¿2.0.CO;2.

Hanel, R., B. Schlachman, D. Rogers, and D. Vanous, 1971: Nimbus 4 michelson interferometer. *Appl. Opt.*, **10 (6)**, 1376–1382.

Hansen, J. E. and L. D. Travis, 1974: Light scattering in planetary atmospheres. *Space Sci. Rev.*, **16 (4)**, 527–610, 10.1007/BF00168069.

Harries, J., et al., 2008: The far-infrared earth. *Rev. Geophys.*, **46 (4)**, RG4004.

Hart, C., 2012: Interpretation of small particle signatures in satellite observations of convective storms. M.S. thesis, University of Wisconsin-Madison.

Heidinger, A. K. and M. J. Pavolonis, 2009: Gazing at cirrus clouds for 25 years through a split window. part i: Methodology. *J. Appl. Meteor. Climatol.*, **48 (6)**, 1100–1116.

Hilleary, D. T., E. L. Heacock, W. A. Morgan, R. H. Moore, E. C. Mangold, and S. D. Soules, 1966: Indirect measurements of atmospheric temperature profiles from satellites: III. the spectrometers and experiments. *Mon. Wea. Rev.*, **94 (6)**, 367–377.

Hilton, F., N. C. Atkinson, S. J. English, and J. R. Eyre, 2009: Assimilation of IASI at the met office and assessment of its impact through observing system experiments. *Quart. J. Roy. Meteor. Soc.*, **135 (639)**, 495–505, doi:10.1002/qj.379.

Hilton, F., et al., 2011: Hyperspectral earth observation from IASI: five years of accomplishments. *Bull. Amer. Meteor. Soc.*, **93 (3)**, 347–370, doi:10.1175/BAMS-D-11-00027.1.

Huang, H.-L., P. Yang, H. Wei, B. A. Baum, Y. Hu, P. Antonelli, and S. A. Ackerman, 2004: Inference of ice cloud properties from high spectral resolution infrared observations. *IEEE Trans. Geosci. Remote Sens.*, **42 (4)**, 842 – 853, doi:10.1109/TGRS.2003.822752.

Inoue, T., 1985: On the temperature and effective emissivity determination of semi-transparent cirrus clouds by bi-spectral measurements in the 10 um window region. *J. Meteorol. Soc. Jpn.*, **64**, 88–99.

John, V. O. and B. J. Soden, 2006: Does convectively-detrained cloud ice enhance water vapor feedback? *Geophys. Res. Lett.*, **33 (20)**, L20 701, doi:10.1029/2006GL027260.

Kahn, B. H., S. L. Nasiri, M. M. Schreier, and B. A. Baum, 2011: Impacts of subpixel cloud heterogeneity on infrared thermodynamic phase assessment. *J. Geophys. Res.*, **116 (D20)**, D20 201, doi:10.1029/2011JD015774.

Kahn, B. H., et al., 2003: Near micron-sized cirrus cloud particles in high-resolution infrared spectra: An orographic case study. *Geophys. Res. Lett.*, **30 (8)**, 1441, doi:10.1029/2003GL016909.

Kaplan, L. D., 1959: Inference of atmospheric structure from remote radiation measurements. *J. Opt. Soc. Am.*, **49 (10)**, 1004–1006.

Knuteson, R. O., F. A. Best, D. H. DeSlover, B. J. Osborne, H. E. Revercomb, and W. L. Smith, 2004a: Infrared land surface remote sensing using high spectral resolution aircraft observations. *Adv. Space Res.*, **33 (7)**, 1114–1119, doi:10.1016/S0273-1177(03)00752-X.

Knuteson, R. O., et al., 2004b: Atmospheric emitted radiance interferometer. part I: instrument design. *J. Atmos. Oceanic Technol.*, **21 (12)**, 1763–1776.

Kratz, D. P., 2002: High-resolution modeling of the far infrared. *Optical Spectroscopic Techniques, Remote Sensing, and Instrumentation for Atmospheric and Space Research IV*, A. M. Larar and M. G. Mlynczak, Eds., SPIE, San Diego, CA, USA, Vol. 4485, 171–180.

Kreisler, A. J. and A. Gaugue, 2000: Recent progress in high-temperature superconductor bolometric detectors: from the mid-infrared to the far-infrared (THz) range. *Supercond. Sci. Technol.*, **13 (8)**, 1235.

Kurucz, R. L., 1992: Synthetic infrared spectra. *Infrared Solar Physics*, Kluwer Academic.

Li, J. and J. Li, 2008: Derivation of global hyperspectral resolution surface emissivity spectra from advanced infrared sounder radiance measurements. *Geophys. Res. Lett.*, **35 (15)**, L15 807, doi:10.1029/2008GL034559.

Li, J., et al., 2005: Retrieval of cloud microphysical properties from MODIS and AIRS. *J. Appl. Meteor.*, **44 (10)**, 1526–1543.

Merrelli, A. and D. D. Turner, 2011: Comparing information content of upwelling far-infrared and midinfrared radiance spectra for clear atmosphere profiling. *J. Atmos. Oceanic Technol.*, **29 (4)**, 510–526, doi:10.1175/JTECH-D-11-00113.1.

Mlawer, E. J., V. H. Payne, J.-L. Moncet, J. S. Delamere, M. J. Alvarado, and D. C. Tobin, 2012: Development and recent evaluation of the MT_CKD model of continuum absorption. *Philos. Trans. R. Soc. London, Ser. A*, **370 (1968)**, 2520–2556, doi:10.1098/rsta.2011.0295.

Mlawer, E. J., S. J. Taubman, P. D. Brown, M. J. Iacono, and S. A. Clough, 1997: Radiative transfer for inhomogeneous atmospheres: RRTM, a validated correlated-k model for the longwave. **102 (D14)**, 16 663–16 682.

Mlynczak, M., 2010: Infrared instrument overview. *CLARREO Science Team Meeting*, National Institute of Aerospace, Hampton, VA.

Mlynczak, M. G., et al., 2006: First light from the far-infrared spectroscopy of the troposphere (FIRST) instrument. *Geophys. Res. Lett.*, **33**.

Nasiri, S. L., H. Van T. Dang, B. H. Kahn, E. J. Fetzer, E. M. Manning, M. M. Schreier, and R. A. Frey, 2011: Comparing MODIS and AIRS infrared-based cloud retrievals. *J. Appl. Meteor. Climatol.*, **50 (5)**, 1057–1072, doi:10.1175/2010JAMC2603.1.

Nordh, H. L., et al., 2003: The Odin orbital observatory. *Astron. Astrophys.*, **402**, L21–L25, doi:10.1051/0004-6361:20030334.

Parol, F., J. Buriez, G. Brogniez, and Y. Fouquart, 1991: Information content of AVHRR channels 4 and 5 with respect to the effective radius of cirrus cloud particles. *J. Appl. Meteor.*, **30 (7)**, 973–984, doi:10.1175/1520-0450-30.7.973.

Petty, G. W. and W. Huang, 2011: The modified gamma size distribution applied to inhomogeneous and nonspherical particles: Key relationships and conversions. *J. Atmos. Sci.*, **68 (7)**, 1460–1473, doi:10.1175/2011JAS3645.1.

Purser, R. J. and H.-L. Huang, 1993: Estimating effective data density in a satellite retrieval or an objective analysis. *J. Appl. Meteor.*, **32 (6)**, 1092–1107.

Rabier, F., N. Fourrié, D. Chafäi, and P. Prunet, 2002: Channel selection methods for infrared atmospheric sounding interferometer radiances. *Quart. J. Roy. Meteor. Soc.*, **128 (581)**, 1011–1027.

Radel, G., C. J. Stubenrauch, R. Holz, and D. L. Mitchell, 2003: Retrieval of effective ice crystal size in the infrared: Sensitivity study and global measurements from TIROS-N operational vertical sounder. *J. Geophys. Res.*, **108 (D9)**, 4281, doi:10.1029/2002JD002801.

Rathke, C., J. Fischer, S. Neshyba, and M. Shupe, 2002: Improving IR cloud phase determination with 20 microns spectral observations. *Geophys. Res. Lett.*, **29 (8)**, 1209.

Revercomb, H. E., et al., 2003: The ARM program's water vapor intensive observation periods. *Bull. Amer. Meteor. Soc.*, **84 (2)**, 217–236, doi:10.1175/BAMS-84-2-217.

Rizzi, R., C. Serio, and R. Amorati, 2002: Sensitivity of broadband and spectral measurements of outgoing radiance to changes in water vapor content. *Optical Spectroscopic Techniques, Remote Sensing, and Instrumentation for Atmospheric and Space Research IV*, A. M. Larar and M. G. Mlynczak, Eds., SPIE, San Diego, CA, USA, Vol. 4485, 181–190.

Rodgers, C. D., 2000: *Inverse Methods for Atmospheric Sounding*, Series on Atmospheric, Oceanic and Planetary Physics, Vol. 2. World Scientific.

Rodgers, C. D., P. B. Hays, and J. Wang, 1996: Information content and optimization of high-spectral-resolution measurements. *Optical Spectroscopic Techniques and Instrumentation for Atmospheric and Space Research II*, SPIE, Denver, CO, USA, Vol. 2830, 136–147.

Rothman, L., et al., 2005: The HITRAN 2004 molecular spectroscopic database. *J. Quant. Spectrosc. Radiat. Transfer*, **96 (2)**, 139–204, doi:10.1016/j.jqsrt.2004.10.008.

Rothman, L., et al., 2009: The HITRAN 2008 molecular spectroscopic database. *J. Quant. Spectrosc. Radiat. Transfer*, **110 (9–10)**, 533–572, doi:10.1016/j.jqsrt.2009.02.013.

Sandford, S. P., et al., 2010: CLARREO: cornerstone of the climate observing system measuring decadal change through accurate emitted infrared and reflected solar spectra and radio occultation. *Sensors, Systems, and Next-Generation Satellites XIV*, R. Meynart, S. P. Neeck, and H. Shimoda, Eds., SPIE, Toulouse, France, Vol. 7826.

Schoeberl, M., et al., 2006: Overview of the EOS Aura mission. *IEEE Trans. Geosci. Remote Sens.*, **44 (5)**, 1066–1074, doi:10.1109/TGRS.2005.861950.

Schwalb, A., 1978: The TIROS-N/NOAA A-G satellite series. 75.

Seemann, S. W., E. E. Borbas, R. O. Knuteson, G. R. Stephenson, and H.-L. Huang, 2008: Development of a global infrared land surface emissivity database for application to clear sky sounding retrievals from multispectral satellite radiance measurements. *J. Appl. Meteor.*, **47 (1)**, 108–123.

Smith, W. L., D. T. Hilleary, J. C. Fischer, H. B. Howell, and H. M. Woolf, 1974: Nimbus-5 ITPR experiment. *Appl. Opt.*, **13 (3)**, 499.

Smith, W. L., H. M. Woolf, and W. J. Jacob, 1970: A regression method for obtaining real-time temperature and geopotential height profiles from satellite spectrometer measurements and its application to numbus 3 "SIRS" observations. *Mon. Wea. Rev.*, **98 (8)**, 582–603.

Stamnes, K., S.-C. Tsay, W. Wiscombe, and K. Jayaweera, 1988: Numerically stable algorithm for discrete-ordinate-method radiative transfer in multiple scattering and emitting layered media. *Appl. Opt.*, **27 (12)**, 2502–2509.

Strabala, K. I., S. A. Ackerman, and W. P. Menzel, 1994: Cloud properties inferred from 8-12 μm data. *J. Appl. Meteor.*, **33 (2)**, 212–229.

Stubenrauch, C. J., R. Holz, A. Chédin, D. L. Mitchell, and A. J. Baran, 1999: Retrieval of cirrus ice crystal sizes from 8.3 and 11.1 μm emissivities determined by the improved initialization inversion of TIROS-N operational vertical sounder observations. *J. Geophys. Res.*, **104 (D24)**, 31 793–31 808, doi:10.1029/1999JD900828.

Stuhlmann, R., A. Rodriguez, S. Tjemkes, J. Grandell, A. Arriaga, J.-L. Bézy, D. Aminou, and P. Bensi, 2005: Plans for EUMETSAT's third generation meteosat geostationary satellite programme. *Adv. Space Res.*, **36 (5)**, 975–981, doi:10.1016/j.asr.2005.03.091.

Susskind, J., C. Barnet, and J. Blaisdell, 2003: Retrieval of atmospheric and surface parameters from AIRS/AMSU/HSB data in the presence of clouds. *IEEE Trans. Geosci. Remote Sens.*, **41 (2)**, 390–409.

Susskind, J., C. Barnet, J. Blaisdell, L. Iredell, F. Keita, L. Kouvaris, G. Molnar, and M. Chahine, 2006: Accuracy of geophysical parameters derived from Atmospheric Infrared Sounder/Advanced Microwave Sounding Unit as a function of fractional cloud cover. *J. Geophys. Res.*, **111 (D9)**, journal Article.

Susskind, J., J. Rosenfield, D. Reuter, and M. T. Chahine, 1984: Remote sensing of weather and climate parameters from HIRS2/MSU on TIROS-N. *J. Geophys. Res.*, **89**, 4677–4697.

Takahashi, C., S. Ochiai, and M. Suzuki, 2010: Operational retrieval algorithms for JEM/SMILES level 2 data processing system. *J. Quant. Spectrosc. Radiat. Transfer*, **111 (1)**, 160–173, doi: 10.1016/j.jqsrt.2009.06.005.

Turner, D. D., 2005: Arctic mixed-phase cloud properties from AERI lidar observations: Algorithm and results from SHEBA. *J. Appl. Meteor.*, **44 (4)**, 427–444.

Turner, D. D. and U. Löhnert, 2012: Retrieved temperature and humidity profiles from the AERI during MC3E. *Atmospheric System Research Science Team Meeting 2012*.

Turner, D. D., A. Merrelli, D. Vimont, and E. J. Mlawer, 2012: Impact of modifying the longwave water vapor continuum absorption model on community earth system model simulations. *J. Geophys. Res.*, **117 (D4)**, D04 106, doi:10.1029/2011JD016440.

Turner, D. D. and E. J. Mlawer, 2010: The radiative heating in underexplored bands campaigns. *Bull. Amer. Meteor. Soc.*, **91 (7)**, 911–923.

Turner, D. D., et al., 2004: The QME AERI LBLRTM: a closure experiment for downwelling high spectral resolution infrared radiance. *J. Atmos. Sci.*, **61 (22)**, 2657–2675.

Walther, A. and A. K. Heidinger, 2012: Implementation of the daytime cloud optical and microphysical properties algorithm (DCOMP) in PATMOS-x. *J. Appl. Meteor.*, **51 (7)**, 1371–1390, doi:10.1175/JAMC-D-11-0108.1.

Wark, D. Q. and H. E. Fleming, 1966: Indirect measurements of atmospheric temperature profiles from satellites: I. introduction. *Mon. Wea. Rev.*, **94 (6)**, 351–362.

Wark, D. Q. and D. T. Hilleary, 1969: Atmospheric temperature: Successful test of remote probing. *Science*, **165 (3899)**, 1256–1258, doi:10.1126/science.165.3899.1256.

Wark, D. Q., F. Saiedy, and D. G. James, 1967: Indirect measurements of atmospheric temperature profiles from satellites: VI. high-altitude balloon testing. *Mon. Wea. Rev.*, **95 (7)**, 468–479.

Warren, S. G. and R. E. Brandt, 2008: Optical constants of ice from the ultraviolet to the microwave: A revised compilation. *J. Geophys. Res.*, **113 (D14)**, D14 220.

Waters, J., et al., 2006: The earth observing system microwave limb sounder (EOS MLS) on the aura satellite. *Geoscience and Remote Sensing, IEEE Transactions on*, **44 (5)**, 1075–1092, doi: 10.1109/TGRS.2006.873771.

Wylie, D. P., W. P. Menzel, H. M. Woolf, and K. I. Strabala, 1994: Four years of global cirrus cloud statistics using HIRS. *J. Climate*, **7 (12)**, 1972–1986.

Yang, P., H. Wei, H.-L. Huang, B. A. Baum, Y. X. Hu, G. W. Kattawar, M. I. Mishchenko, and Q. Fu, 2005: Scattering and absorption property database for nonspherical ice particles in the near- through far-infrared spectral region. *Appl. Opt.*, **44 (26)**, 5512–5523.

Yang, P., et al., 2003: Spectral signature of ice clouds in the far-infrared region: Single-scattering calculations and radiative sensitivity study. *J. Geophys. Res.*, **108**.

Zhou, D. K., W. L. Smith, X. Liu, A. M. Larar, S. A. Mango, and H.-L. Huang, 2007: Physically retrieving cloud and thermodynamic parameters from ultraspectral IR measurements. *J. Atmos. Sci.*, **64 (3)**, 969–982.

Appendix A: List of Satellite Instruments

The following tables contain a brief summary of all satellite instruments mentioned in Chapter 2. References, key specifications (wavenumber coverage, approximate spectral resolution, and spatial resolution), platforms, and operational dates are listed. The comment column lists and extra information, such as those instruments that are limb sounders, and those that are Fourier Transform Spectrometers (FTS). For limb sounders, the listed spatial resolution is the width of the beam at the tangent point. The number of channels listed for an FTS is flexible, since it can change depending on the processing applied to the raw interferogram. The number listed is either the number used in standard L1 processing, or for the older instruments (e.g., IRIS), just the spectral coverage divided by the resolution.

Table A.1 Satellite instrument acronym list

Acronym	Expansion	Table
AERI-ER	Atmospheric Emitted Radiance Interferometer - Extended Range	A.4
AIRS	Atmospheric InfraRed Sounder	A.2
AVHRR	Advanced Very High Resolution Radiometer	A.2
CLARREO	CLimate Absolute Radiance and Refractivity Observatory	A.4
CrIS	Cross-track Infrared Sounder	A.2
FIRST	Far-InfraRed Spectroscopy of the Troposphere	A.4
HIRS	High resolution Infrared Radiation Sounder (TOVS subsystem)	A.2
IASI	Infrared Atmospheric Sounding Interferometer	A.2
IASI-NG	IASI - New Generation	A.2
IRIS	InfraRed Interferometer Spectrometer	A.2
ITPR	Infrared Temperature Profiling Radiometer	A.2
MIPAS	Michelson Interferometer for Passive Atmospheric Sounding	A.2
MLS	Microwave Limb Sounder	A.3
MODIS	MODerate resolution Imaging Spectrometer	A.2
REFIR	Radiation Explorer in the Far-InfraRed	A.4
SIRS	Satellite InfraRed Spectrometer	A.2
SMILES	Superconducting subMIllimeter-wave Limb Emission Sounder	A.3
SMR	SubMillimeter Radiometer	A.3
TAFTS	Tropospheric Airborne Fourier Transform Spectrometer	A.4
TOVS	TIROS-N Operational Vertical Sounding system	A.2

Table A.2 Infrared Satellite Instrument list

Instrument	Satellite	Launch Year	Wavenumber coverage [cm^{-1}]	Approx. spec. res. [cm^{-1}]	Num of spec. chan.	Spatial res. [km]	Comments	Ref.
SIRS	Nimbus 3	1969	670–900	5	7	225		Wark and Hilleary (1969)
IRIS-B	Nimbus 3	1969	400–2000	5	320	150	FTS	Conrath et al. (1970)
IRIS-D	Nimbus 4	1970	400–1600	2.8	420	95	FTS	Hanel et al. (1971)
ITPR	Nimbus 5	1972	540–2900	5–400	5	20		Smith et al. (1974)
HIRS	Nimbus 6, TIROS-N	1975	685–2700	3–100	19	17		Schwalb (1978)
AVHRR	TIROS-N	1978	800, 900, 2650	75, 300	3	1		Schwalb (1978)
MODIS	Aqua, Terra	1999	700–2700	15–150	16	1		Barnes et al. (1998)
MIPAS	EnviSat	2002	685–2410	0.025	50,000	30	FTS, Limb	Fischer et al. (2008)
AIRS	Aqua	2002	650–2665	0.4–2.1	2378	13.5		Chahine et al. (2006)
IASI	MetOp-A	2006	645–2760	0.5	8461	12	FTS	Hilton et al. (2011)
CrIS	Suomi-NPP	2011	650–2550	0.625	1305	14	FTS	Bingham et al. (2010)
IASI-NG	EPS-SG	2020	645–2760	0.25	16921	12	FTS	Crevoisier (2012)

Table A.3 Submillimeter Satellite Instrument list

Instrument	Satellite	Launch Year	Frequency coverage [GHz]	Approx. spec. res. [MHz]	Num of spec. chan.	Spatial res. [km]	Comments	Ref.
SMR	Odin	2001	486–581	0.1–1	$\sim$1000	?	Limb scanner	Nordh et al. (2003)
MLS	Aura	2004	118–2250	0.2–500	728	$2-12$	Limb scanner	Waters et al. (2006)
SMILES	ISS	2009	624–650	1.8	3456	?	Limb scanner	Takahashi et al. (2010)

Table A.4 Far Infrared instrument list

Instrument	Frequency coverage [cm^{-1}]	Approx. spec. res. [cm^{-1}]	Num of spec. chan.	Comments	Ref.
AERI-ER	400–2400	0.5	2000	FTS, cooled photoelectric detector	Knuteson et al. (2004b)
CLARREO	200–2000	0.5	3600	FTS	Sandford et al. (2010)
FIRST	50–2000	0.625		FTS, cooled bolometer detector	Mlynczak et al. (2006)
REFIR	100–1400	0.5	2600	FTS, room temperature pyroelectric detector	Bianchini et al. (2006)
TAFTS	100–600	0.12		FTS, cryogenic photoelectric detectors	Canas et al. (1997)

Appendix B: IWP derivatives

The equation relating the IWP error to the posterior error covariance 5.14 requires the derivatives of the IWP with respect to the retrieved state variables. The alternative form of the gamma PSD 5.5 and the IWP equation 5.13 are reproduced here for clarity:

$$N(r) = \frac{N_0}{(r_0\sigma)^{\frac{1-2\sigma}{\sigma}}\Gamma\left(\frac{1-2\sigma}{\sigma}\right)} r^{\frac{1-3\sigma}{\sigma}} e^{-\frac{r}{\sigma r_0}} \tag{B.1}$$

$$I = \frac{1}{2}\rho_{\mathrm{i}}\tau\frac{\int_{r_1}^{r_2} V(r)N(r;r_0,\sigma)\,dr}{\int_{r_1}^{r_2} A(r)N(r;r_0,\sigma)\,dr} \tag{B.2}$$

The required derivative is:

$$K_I = \left[\frac{\partial\,\mathrm{IWP}}{\partial\tau}, \frac{\partial\,\mathrm{IWP}}{\partial\sigma}, \frac{\partial\,\mathrm{IWP}}{\partial r_0}\right] \tag{B.3}$$

It is convenient to express this derivative by first calculating the derivatives of the PDF function $n(r;r_0,\sigma)$ with respect to the two PDF parameters, r_0 and σ:

$$\frac{\partial n(r;\sigma,r_0)}{\partial r_0} = n(r;\sigma,r_0)\left[\frac{r}{r_0} + 2\sigma - 1\right]\frac{1}{\sigma r_0} \tag{B.4}$$

$$\frac{\partial n(r;\sigma,r_0)}{\partial \sigma} = n(r;\sigma,r_0)\frac{1}{\sigma^2}\left[\frac{1}{r_0}\left(r - r_0\ln\left(\frac{r}{\sigma r_0}\right)\right) + \psi^0\left(\frac{1-2\sigma}{\sigma}\right) + 2\sigma - 1\right] \tag{B.5}$$

The function $\psi^0(x)$ is the 0-order polygamma function, also known as the digamma function. It is equal to the first derivative of the logarithm of the gamma function.

The IWP derivatives can then be written in terms of the two n derivatives. In these expressions, the arguments of n are omitted for brevity, meaning n in these equations represents $n(r;r_0,\sigma)$:

$$\frac{\partial \mathrm{IWP}}{\partial \tau} = \frac{\mathrm{IWP}}{\tau} \tag{B.6}$$

$$\frac{\partial \mathrm{IWP}}{\partial \sigma} = \frac{\rho_i \tau}{2} \frac{\int \frac{\partial n}{\partial \sigma} V(r)\, dr \int nA(r)\, dr - \int \frac{\partial n}{\partial \sigma} A(r)\, dr \int nV(r)\, dr}{\left(\int nA(r)\, dr \right)^2} \tag{B.7}$$

$$\frac{\partial \mathrm{IWP}}{\partial r_0} = \frac{\rho_i \tau}{2} \frac{\int \frac{\partial n}{\partial r_0} V(r)\, dr \int nA(r)\, dr - \int \frac{\partial n}{\partial r_0} A(r)\, dr \int nV(r)\, dr}{\left(\int nA(r)\, dr \right)^2} \tag{B.8}$$

The description of $V(r)$ and $A(r)$ in the Yang et al. (2005) database are vectors of values computed at the particle size grid values. Since not all particle descriptions have fixed power law relationships for the volume-size relationship (see figure 5.1), the array of pre-computed values must be used. The IWP derivatives must be computed numerically for this reason.